Measurement of $D^{*\pm}$ Cross Sections in Photon Proton Collisions at HERA

by

S. Stonjek

Measurement of $D^{*\pm}$ Cross Sections in Photon Proton Collisions at HERA

Dissertation
zur Erlangung des Doktorgrades
des Fachbereiches Physik
der Universität Hamburg

vorgelegt von

Stefan Stonjek

aus Harderberg

Hamburg
2001

Gutachter der Dissertation:	Prof. Dr. R. Klanner Prof. Dr. V. Blobel
Gutachter der Disputation:	Prof. Dr. Erich Lohrmann Prof. Dr. Joachim Meyer
Datum der Disputation:	06.09.2001
Dekan des Fachbereichs Physik und Vorsitzender des Promotionsausschusses:	Prof. Dr. F.-W. Büßer

Abstract

Open charm photoproduction has been studied with the ZEUS detector in electron proton collisions at the HERA collider at $\sqrt{s} = 300$ GeV. The $D^{*\pm} \rightarrow K^{\mp}\pi^{\pm}\pi^{\pm}$ decay mode has been measured using data taken in 1996 and 1997 which correspond to an integrated luminosity of $\mathcal{L} = 16.6$ pb^{-1}. In the restricted phase space $-1.0 < \eta(D^*) < 1.5$, 2.0 GeV $< p_{\perp}(D^*) < 8.0$ GeV, 80 GeV $< W < 120$ GeV and $Q^2 < 0.15$ GeV^2 the total cross section was measured to $\sigma_{ep\rightarrow eD^*X} = 8.8 \pm 0.7(stat)^{+0.5}_{-1.0}(syst)$ nb. Differential cross sections have been measured as a function of $p_{\perp}(D^*)$ and $\eta(D^*)$. They are compared to different NLO QCD calculations. Within their limits of applicability the calculations are in reasonable agreement with the data. A slight excess of the cross section was found towards the proton direction.

Kurzzusammenfassung

Mit dem ZEUS Detektor wurde die Photoproduktion von Mesonen mit Charm Quarks in Elektron Proton Streuung bei HERA bei $\sqrt{s} = 300$ GeV untersucht. Dazu wurde der Zerfall $D^{*\pm} \rightarrow K^{\mp}\pi^{\pm}\pi^{\pm}$ in den Daten von 1996 und 1997 mit einer integrierten Luminosität von $\mathcal{L} = 16.6$ pb^{-1} verwendest. Im eingeschränkten Phasenraum $-1.0 < \eta(D^*) < 1.5$, 2.0 GeV $< p_{\perp}(D^*) < 8.0$ GeV, 80 GeV $< W < 120$ GeV und $Q^2 < 0.15$ GeV^2 wurde ein Wirkungsquerschnitt von $\sigma_{ep\rightarrow eD^*X} = 8.8 \pm 0.7(stat)^{+0.5}_{-1.0}(syst)$ nb gemessen. Die differentiellen Wirkungsquerschnitte $d\sigma/dp_{\perp}(D^*)$ und $d\sigma/d\eta(D^*)$ wurden untersucht und mit verschiedenen QCD Rechnungen nächstführender Ordnung der starken Kopplungskonstanten verglichen. Die Rechnungen stimmen im allgemeinen, im Rahmen ihrer Gültigkeitsbereiche, mit den Daten überein. Die Daten zeigen aber einen leichten Überschuß in Richtung des Protons.

Contents

Introduction **13**

1 Theory **17**

1.1 Lepton Nucleon Scattering 17

1.2 Photoproduction 18

1.2.1 Direct Photoproduction 20

1.2.2 Resolved Photoproduction 20

1.2.3 General Photoproduction Calculation 21

1.2.4 The Structure of the Photon 22

1.3 Charm in Photoproduction 24

1.3.1 Perturbative Formalism for Heavy Quark Photoproduction 24

1.3.2 "Massive Model" for Heavy Flavor in Photoproduction 25

1.3.3 "Massless Model" for Heavy Flavor in Photoproduction 26

1.4 Charm Identification via D^* Decay 27

1.4.1 Fragmentation 28

1.4.2 The D^* Decay 28

2 Experimental Setup **31**

2.1 HERA 31

2.2 The ZEUS Detector 31

2.2.1 Tracking 34

2.2.1.1 Central Tracking Detector 34

2.2.2 Calorimeter 35

2.2.2.1 The Uranium Calorimeter 36

2.2.3 Electron Tagger 39

2.2.3.1 44m Tagger 39
2.2.4 Trigger and Online 39
2.2.5 Reconstruction, Data Storage and Analysis Software 41
2.2.6 Monte Carlo 42
2.3 ZES 42
2.3.1 Design and Implementation of ZES 43

3 Monte Carlo Simulation 45
3.1 Simulation of the Physics Process 45
3.1.1 HERWIG 47
3.1.2 PYTHIA 47
3.2 Simulation of the Detector Response 48

4 Methods 49
4.1 Track Reconstruction in the CTD 49
4.1.1 Differences between positive and negative tracks 51
4.2 D* Reconstruction 52
4.2.1 Background 53
4.2.1.1 Wrong Charge Combination 54
4.2.1.2 Fitting the ΔM distribution 55
4.2.1.2.1 Differences between D^{*+} and D^{*-} 56
4.3 Photoproduction Selection with the 44m Tagger 57

5 Analysis 59
5.1 Data Sample 59
5.2 Event Selection 59
5.2.1 Trigger Selection 59
5.2.2 Offline Selection 60
5.2.3 Photoproduction Selection 60
5.2.4 D* Meson Selection 61
5.3 Acceptance 65
5.3.1 44m Tagger Acceptance 66

5.3.2 D* Meson Acceptance 68
5.3.2.1 Grid Correction 69
5.4 Systematical Uncertainties 71
5.4.1 Charge Asymmetry 72

6 Results **75**
6.1 Cross Section 75
6.1.1 Total Cross Section 75
6.1.2 Differential Cross Sections 75

Summary and Conclusions **85**

List of Figures

1.1 General sketch of lepton nucleon scattering 17
1.2 Leading order direct processes 20
1.3 Examples for leading order resolved processes 21
1.4 General sketch of a resolved photoproduction process 22
1.5 Sketch of a process which can be either direct or resolved photoproduction . 23
1.6 Electron probing an on shell photon with a virtual photon 23
1.7 Sketch of charm excitation 26
1.8 Comparison of massive and massless scheme 27

2.1 HERA collider 32
2.2 ZEUS detector (longitudinal section) 33
2.3 ZEUS detector (transverse section) 33
2.4 Central tracking detector 35
2.5 Uranium calorimeter 37
2.6 Calorimeter module 38
2.7 The ZEUS tagger system 40
2.8 Layout of the 44m tagger 40
2.9 ZEUS trigger system 41
2.10 ZEUS dataflow 42
2.11 ZES Database Schema 44

3.1 Schematic view of the processes in a generator 46
3.2 Hadronisation models 46

4.1 Negative track in a CTD cell 49
4.2 Track helix 51

4.3 Field configuration around a sense wire 51
4.4 ΔM distribution for 44m tagged events 53
4.5 $M(D^0)$ distribution for 44m tagged events 54
4.6 Background normalization 55
4.7 ΔM distribution for 44m tagged events with D^{*+} 56
4.8 ΔM distribution for 44m tagged events with D^{*-} 57

5.1 Acceptance of the electron tagger as function of the electron energy 61
5.2 W_{true} vs. W 62
5.3 $W_{generated}$ vs. $W_{measured}$ (Profile and Difference) 63
5.4 Comparison of the reconstructed $\eta(K)$ and $p_\perp(K)$ for data and Monte Carlo 64
5.5 Comparison of the reconstructed $\eta(\pi)$ and $p_\perp(\pi)$ for data and Monte Carlo . 64
5.6 Comparison of the reconstructed $\eta(\pi_s)$ and $p_\perp(\pi_s)$ for Data and Monte Carlo 65
5.7 Comparison of $p_\perp(D^*)$ and $\eta(D^*)$ for Data and Monte Carlo 65
5.8 ΔM distribution for 44m tagged events 66
5.9 $M(D^0)$ distribution for 44m tagged events 67
5.10 Acceptance of the electron tagger as function of the electron energy 67
5.11 Generated $\eta(D^*)$ and $p_\perp(D^*)$ with and without track requirements 68
5.12 Difference between generated and Monte Carlo reconstructed $p_\perp(D^*)$ and $\eta(D^*)$ 69
5.13 Relation between generated and Monte Carlo reconstructed $p_\perp(D^*)$ and $\eta(D^*)$ 69
5.14 Difference between generated and Monte Carlo reconstructed $p_\perp(K)$ and $\eta(K)$ 70
5.15 Difference between generated and Monte Carlo reconstructed $p_\perp(\pi)$ and $\eta(\pi)$ 70
5.16 Difference between generated and Monte Carlo reconstructed $p_\perp(\pi_s)$ and $\eta(\pi_s)$ 71
5.17 Acceptance for D^{*+} and D^{*-} as function of $\eta(D^*)$ and $p_\perp(D^*)$ 72
5.18 Charge asymmetry for photoproduction events tagged by the 44m tagger . . 73
5.19 Charge asymmetry for untagged events 74
5.20 Charge asymmetry for untagged events in ηD^* bins 74

6.1 Differential cross sections $d\sigma/dp_\perp(D^*)$ for -1.0 $< \eta(D^*) <$ 1.5 76
6.2 Differential cross sections $d\sigma/d\eta(D^*)$ for 2 GeV $< p_\perp(D^*) <$ 8 GeV 77
6.3 Differential cross sections $d\sigma/d\eta(D^*)$ for 2 GeV $< p_\perp(D^*) <$ 3.25 GeV 78
6.4 Differential cross sections $d\sigma/d\eta(D^*)$ for 3.25 GeV $< p_\perp(D^*) <$ 8 GeV 79

6.5 Differential cross sections $d\sigma/dp_\perp(D^*)$ for -1.0 $< \eta(D^*) <$ 1.5 79

6.6 Differential cross sections $d\sigma/d\eta(D^*)$ for 3.25 GeV $< p_\perp(D^*) <$ 8 GeV 80

6.7 Differential cross sections $d\sigma/dp_\perp(D^*)$ for untagged photoproduction 80

6.8 Differential cross sections $d\sigma/d\eta(D^*)$ for untagged photoproduction 81

6.9 Different fragmentations for $d\sigma_{ep\to D^*X}/dp_\perp(D^*)$ 82

6.10 Comparison of the massive and the massless calculation to the 3.25 GeV $< p_\perp <$ 8 GeV results 83

6.11 Cross section ratios 84

List of Tables

2.1 Technical parameters of the HERA collider 34
2.2 Technical parameters of the CTD 36
2.3 Technical parameters of the calorimeter 37

Introduction

What is the structure of the matter? This question is probably as old as mankind. One of the first known answers to this question originates from the Greek philosopher Leukipp. He explained the world as being composed of indivisible constituents, called atoms ($\alpha\tau o\mu o\sigma$: greek for indivisible). More than two thousand years later Mendelejew gave a new answer to this question by showing that the chemical elements can be classified in a periodic table and identified their constituents as the atoms. By scattering helium nuclei on gold atoms Rutherford revealed 1911 that these atoms consist of a positively charged nucleus and electrons, discovered by Thompson back in 1897, circling around it. The nucleus was found to consist of protons and neutrons which are held together by the strong force. The model which describes all matter as consisting of protons, neutrons and electrons was found to be too simple since literally hundreds of different particles were found in cosmic rays and in first particle accelerators till the 1960s. Most of these particles, called hadrons, were found to interact strongly like the proton and the neutron. Some of these hadrons were found to have a rather long lifetime compared to the other hadrons. They were called "stange" particles. 1964 Gell-Mann [GM64] and Zweig [Zwe64b] [Zwe64a] proposed that hadrons are composed of constituents, called " quarks". To avoid violating the Pauli principle which forbids states in which two fermions have the same quantum numbers, a new quantum number, called color, was introduced. The color charge has a similar role in the strong interaction as the electric charge in the electromagnetic force. The proton substructure was experimentally confirmed by the first inelastic electron-proton scattering experiment at the Stanford Linear Accelerator Center (SLAC) in 1968. At this time three different flavors of quarks were known: up (u), down(d) and strange(s).

In 1970 a fourth and heavier quark was predicted by Glashow, Iliopoulus and Maiani [GIM70] and called "charm" quark. The first charmed hadron, the bound state of a charm quark and an anti-charm quark, called J/Ψ, was found in November 1974 independently by two groups at BNL [A$^+$74a] and SLAC [A$^+$74b]. A similar resonance was found in 1977 [H$^+$77] containing an even heavier quark, the bottom quark. This discovery lead to the prediction of the sixth quark, the top quark. This prediction was confirmed by the first observation of the top quark at Fermilab in 1994 [CDF94] [CDF95] [D0-95] which was a great success for the so called "Standard Model". In the Standard Model, which describes the electromagnetic, weak and strong force, all matter is composed of fermions (leptons and hadrons) interacting with each other through gauge fields by the exchange of gauge bosons. As Quantum Electro Dynamics (QED) describes the electromagnetic interaction, Quantum Chromo-Dynamics (QCD) describes the interaction of quarks and gluons, the gauge bosons of the strong force.

To calculate the coupling constant of the strong interactions α_s one needs to use renormalization techniques. A large scale, representing a short distance at which α_s is small, provides an opportunity to apply perturbative calculations. The mass of a heavy quark like the charm quark represents a hard scale. Therefore, the measurement of hadrons containing charm quarks provides a good testing ground for perturbative QCD.

At the HERA machine in Hamburg, Germany, electrons collide with protons. The total electron proton cross section is dominated by the exchange of a quasi real photon. Therefore, this process, called "photoproduction", is well suited to study processes with a small cross section like heavy quark production. In this analysis a special detector component was used to tag the scattered electron which allows to study a previously inaccessible kinematic region. Earlier analyses were restricted to a minimal mass of the hadronic system (W) of 130 GeV. This analysis covers 80 GeV $< W <$ 120 GeV.

The aim of this analysis is to measure the cross section of the $D^{*\pm}$ meson in this new kinematic region and to compare the results to different NLO QCD calculations. It is interesting to see if those calculations are able to describe this previously unmeasured region. Since the calculations contain approximations optimized in other kinematic regions or other processes, a successful description of the data will be an important step to prove that the calculations are universally applicable.

Earlier analyses of charmed mesons in electron proton scattering found an excess of the measured cross sections in forward[1] direction when compared to QCD calculations. One possible explanation for this excess is a too simple approximation in the modeling of the fragmentation function of the charm quark to a $D^{*\pm}$ meson. In this case this effect should also be present in the kinematic region used in this analysis.

This thesis is structured in the following way:

An overview of the theory of photoproduction is given in the first chapter. Two general approaches to calculate $D^{*\pm}$ meson cross sections in photoproduction, the massive and the massless one are introduced. The $D^{*\pm}$ meson decay channel $D^{*\pm} \to K^{\mp}\pi^{\pm}\pi^{\pm}$ is described.

The second chapter explains the experimental setup. The main components of the ZEUS detector, the central tracking detector, the uranium calorimeter and the electron tagger are presented. The trigger system and the data taking and storage system are covered, including a tag database to preselect events for a physics analysis.

The simulation of the physics process and the detector response is explained in chapter three.

A detailed description of the D^* meson reconstruction method used in this analysis can be found in chapter four. Track reconstruction and electron tagging is also described in this chapter.

The fifth chapter covers the details of the event selection and the acceptance calculation, including comparison between measured data and Monte Carlo calculations. Also the systematic error is covered in this chapter.

[1] At HERA the proton hemisphere is defined as forward direction.

The results of this analysis are presented in the sixth chapter including total and differential cross sections and their comparison to different NLO QCD calculations.

Chapter 1

Theory

1.1 Lepton Nucleon Scattering

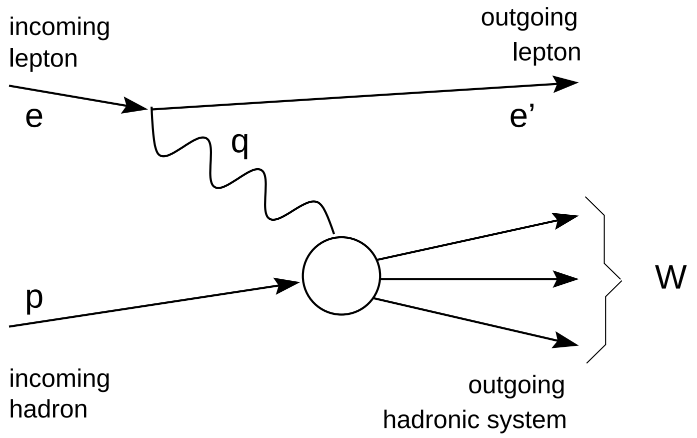

Figure 1.1: General sketch of lepton nucleon. scattering

The scattering process of a lepton and a proton can be described by the exchange of an electroweak boson. This can be a photon (γ) or a Z^0 (neutral current, NC) or a $W^{\pm}$ (charged current, CC). Fig. 1.1 shows a general sketch of this process with $\mathbf{e} = (0, 0, -p_e, E_e)$ / $\mathbf{e}' = (p_e^{'} \sin\theta_e, 0, p_e^{'} \cos\theta_e, E_e^{'})$ being the four vector of the incoming / outgoing lepton and $\mathbf{p} = (0, 0, p_p, E_p)$ the four vector of the incoming proton. E_e and E_p are the energies of the incoming electron and proton which have the momenta p_e and p_p. E_e' is the energy of the outgoing electron with the scattering angle θ_e and the momentum p_e'. The square of the energy in the center of mass system is defined by

$$\mathrm{s} = (\mathbf{e} + \mathbf{p})^2 \approx 4\mathrm{E_e E_p} \tag{1.1}$$

The four vector of the exchanged boson is defined by $\mathbf{q} = \mathbf{e} - \mathbf{e}'$. Since q is spacelike one defines the negative value of the photon virtuality by

$$q^2 = (\mathbf{e} - \mathbf{e}')^2 = -Q^2 \tag{1.2}$$

According to Heisenberg's uncertainty relation $\Delta X \Delta p_x \leq \hbar$ the negative value of the photon virtuality defines the transverse size in the proton $\Delta X \approx \hbar c/\sqrt{Q^2}$ which can be resolved by the photon. Events with $Q^2 \gg 1$ GeV^2 are probing the structure of the proton. This class of processes is called "deep inelastic scattering" (DIS).

The square of the invariant mass of the γ - p system is defined by

$$W^2 = (\mathbf{q} + \mathbf{p})^2. \tag{1.3}$$

1.2 Photoproduction

Due to the photon propagator the total electron-proton cross sections is proportional to $1/Q^4$. Therefore the cross section is dominated by the exchange of quasi real photons with $Q^2 \approx 0$. These photons are emitted collinear to the incoming electron and have a very low virtuality. This process is called "photoproduction". Due to their small virtuality these photons do not probe the proton structure. For $Q^2 \to 0$ GeV^2 the definition

$$y = \frac{\mathbf{pq}}{\mathbf{pe}} \tag{1.4}$$

can be approximated to $y = E_\gamma/E_e$ in the collinear case. E_e and E_γ are the energy of the incoming electron[1] or the emitted photon respectively. This is referred to as the collinear approximation.

Since the exchange of quasi real photons has a much higher cross section than the exchange of virtual photons, such interactions are well suited to study rare processes where large transverse momenta or heavy quarks are produced. In this process the electron beam can be seen as a photon source which leads effectively to a photon proton collider. The coupling at the lepton vertex is purely electromagnetic.

The total cross section σ_{tot}^{ep} can be factorized in terms of the γ - p cross section $\sigma_{tot}^{\gamma p}$ and a flux factor $f_{e\to\gamma}(y)$. This factor can be considered as the probability to get a photon with the energy $E_\gamma = yE_e$ from the electron [Han63] [DW64].

In general photons with transverse and longitudinal polarization contribute to the total cross section:

$$d\sigma^{ep\to eX} = \int dy dQ^2 \left[f_{e\to\gamma,L}(y,Q^2) d\sigma_L^{\gamma_L p\to X} + f_{e\to\gamma,T}(y,Q^2) d\sigma_T^{\gamma_T p\to X} \right] \tag{1.5}$$

[1]HERA can accelerate electrons as well as positrons. The charge of the incoming lepton does not influence the γ-p interaction. In this thesis the generic word electron is used for electrons and positrons. The data presented in this analysis are based upon positron proton collisions.

For $Q^2 \to 0$ GeV^2 the longitudinal contribution vanishes. Therefore the photoproduction cross section can be approximated by

$$\frac{d^2\sigma^{ep}}{dydQ^2} \sim f_{e\to\gamma,T}(y,Q^2)\sigma_{tot}^{\gamma p}(y,Q^2) \tag{1.6}$$

with

$$f_{e\to\gamma,T}(y,Q^2) = \frac{\alpha_{em}}{2\pi}\frac{1}{Q^2}\left[\frac{1+(1-y^2)}{y} - 2\frac{1-y}{y}\frac{Q^2_{min}}{Q^2}\right] \tag{1.7}$$

This is known as the "equivalent photon approximation" (EPA) [BGMS]. The validity of the EPA for electron proton collisions is shown in [BS89]. Neglecting the Q^2 dependence of the $\gamma - p$ cross section and integrating over photon virtualities in a kinematic region leads to the Weizsäcker-Williams approximation [Wei34] [Wil34]

$$f^{WWA}_{e\to\gamma}(y) = \frac{\alpha_{em}}{2\pi}\left[\frac{1+(1-y)^2}{y}\ln\frac{Q^2_{max}}{Q^2_{min}} - 2\frac{1-y}{y}\left(1-\frac{Q^2_{min}}{Q^2_{max}}\right)\right] \tag{1.8}$$

Photoproduction can be divided into two different classes of processes. The photon can either enter the hard subprocess directly or fluctuate into partons before interacting. The first is called "direct" and the second "resolved" photoproduction.

Resolved photoproduction can be divided into two different contributions. The anomalous part and the part described by the Vector Meson Dominance model (VMD). In this model the photon fluctuates to quarks with a small transverse momentum. Therefore a bound state can be formed. This state is a superposition of vector mesons which have the same quantum numbers as the photon: ρ^0, ω, ϕ etc.. The lifetime of the different fluctuation states is given by:

$$t_V \sim \frac{E_\gamma}{m_V^2 + Q^2} \tag{1.9}$$

Therefore the probability of such fluctuations is suppressed for high Q^2 and for high vector meson masses m_v. For mesons formed out of quarks with masses $m_q \geq m_c$ the VMD contribution is negligible.

The anomalous contribution emerging from a small virtuality photon splitting into partons. Due to the large transverse momentum of the partons this contribution is, in principle, perturbatively calculable [Wit77].

It is not physically meaningful to consider the VDM and the anomalous part separately. They are combined to the resolved component.

1.2.1 Direct Photoproduction

In direct photoproduction the incoming photon interacts as a pointlike object. In the hard subprocess the photon couples directly to the parton from the proton. In this case the whole photon energy is participating in the hard subprocess. Therefore the final state of the hard subprocess is expected to have higher transverse momenta compared to the interactions where only a part of the photon energy participates. In leading order of the strong coupling constant α_s only two processes contribute to direct photoproduction (see Fig.1.2). In the Boson Gluon Fusion (BGF, Fig. 1.2 (a)) the photon couples to a quark-antiquark [GM64] pair which also couples to a gluon from the proton. In the QCD Compton process (Fig. 1.2 (b)) the photon couples to a quark radiated from the proton. In both cases the final state of the hard subprocess consist of two partons. Quarks and gluons fragment into jets of colorless hadrons. In the QCD Compton case one jet is initiated by a quark and the other one by a gluon. In the BGF case both jets are initiated by quarks.

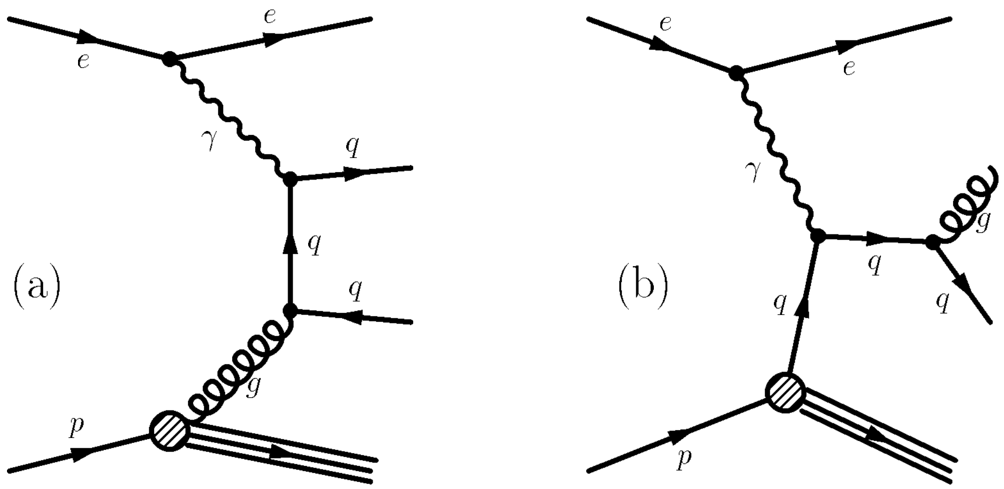

Figure 1.2: Leading order direct processes. (a) Boson gluon fusion (b) QCD Compton scattering.

1.2.2 Resolved Photoproduction

In resolved photoproduction the photon acts as a source of partons. One parton from the photon interacts with a parton from the proton in the hard subprocess. Thus it is similar to hard hadron-hadron interactions. Analogous to the parton from the proton carrying the fraction x_p from the proton momentum the parton from the photon carries the fraction x_γ from the photon momentum. Also the concept of a parton density function for the photon is introduced for resolved photoproduction.

Examples of processes in leading order α_s for resolved photoproduction are shown in Fig. 1.3. Fig. 1.3 (a) shows a gluon from the photon which interacts with a gluon from the proton.

This is called gluon-gluon fusion. In Fig. 1.3 (b) a quark from the photon interacts with a gluon from the proton. As in direct photoproduction the final state contains usually two jets. In the first case both of them are quark jets while in the second case one is a quark jet and the other one is a gluon jet. In addition to the proton remnant present in both types of photoproduction a photon remnant exists in resolved photoproduction.

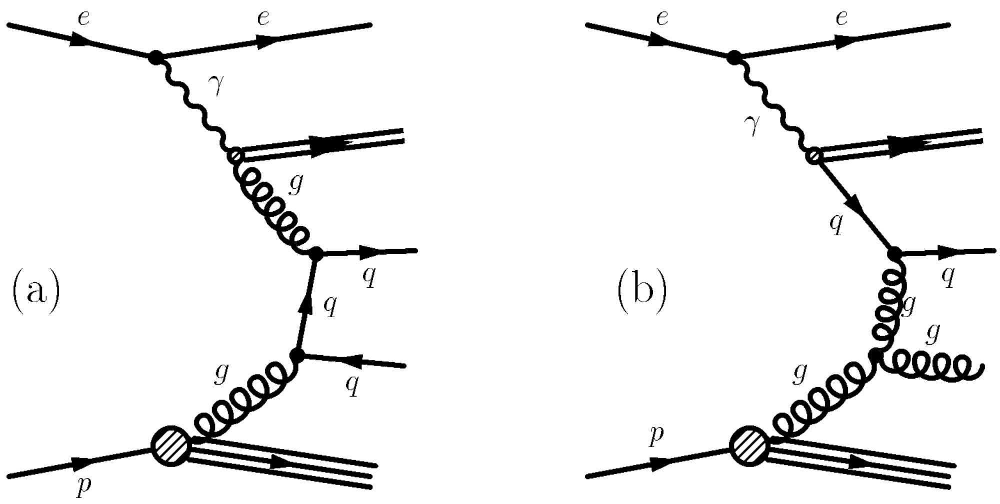

Figure 1.3: Examples for leading order resolved processes.

1.2.3 General Photoproduction Calculation

In general the calculation of hard photoproduction is divided into the hard subprocess with can be calculated perturbatively and the non perturbative parton distribution function with the factorization scales μ_p and μ_γ (see Fig. 1.4 for a sketch). In the direct case the photon enters the hard subprocess directly. The hard subprocess is independent from this arbitrarily chosen factorization scale. A variation of the scale only affects the parton density functions.

The total photoproduction cross section can be separated into the direct and resolved component.

$$d\sigma_{\gamma p\to cd} = d\sigma^{dir}_{\gamma p\to cd} + d\sigma^{res}_{\gamma p\to cd} \tag{1.10}$$

with the direct component

$$d\sigma^{dir}_{\gamma p\to cd} = \sum_b \int_{x_p} dx_p f_{p\to b}(x_p, \mu_p^2) d\hat{\sigma}_{\gamma b\to cd} \tag{1.11}$$

and the resolved component

$$d\sigma^{res}_{\gamma p\to cd} = \sum_{ab} \int_{x_p} dx_p \int_{x_\gamma} dx_\gamma f_{p\to b}(x_p, \mu_p^2) f_{\gamma\to a}(x_\gamma, \mu_\gamma^2) d\hat{\sigma}_{ab\to cd} \tag{1.12}$$

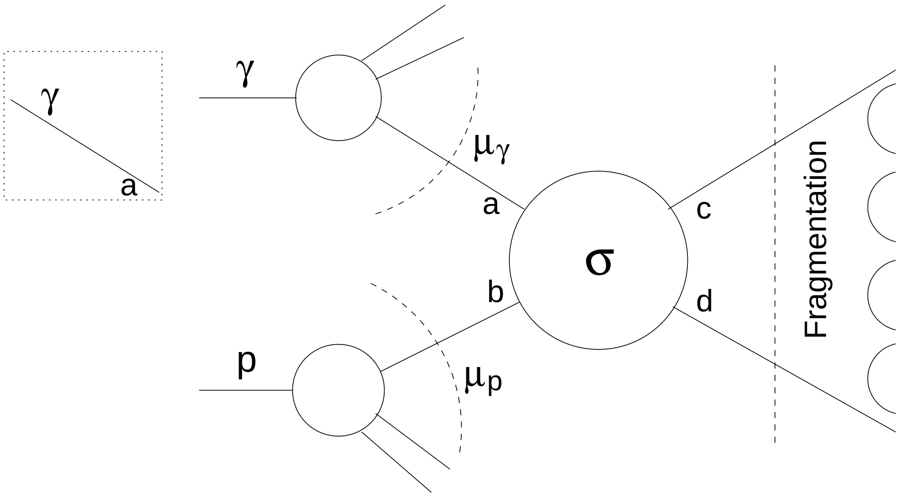

Figure 1.4: General sketch of a resolved photoproduction process. σ indicates the hard subprocess. μ_p and μ_γ denote the arbitrarily chosen factorization scales. In direct photoproduction the photon enters the hard subprocess directly, the incoming photon is identical to the parton a: $a \equiv \gamma$, as shown in the top left corner.

Where $d\hat{\sigma}$ is given by the perturbative matrix element of the hard subprocess and the parton density functions $f_{\gamma\to a}$ and $f_{p\to b}$.

The distinction between direct and resolved processes is only meaningful in leading order. Fig. 1.5 shows a process which can be seen either as a direct ($\mu_\gamma = \mu_2$) or a resolved ($\mu_\gamma = \mu_1$) process. This ambiguity between NLO direct and LO resolved depends on the factorization scale μ_γ. NLO calculations are less dependent on the choice of the factorization scale μ_γ. In next-to-leading order (NLO) QCD only the sum of direct and resolved photoproduction processes is unambiguously defined.

1.2.4 The Structure of the Photon

For the case of resolved photoproduction the photon has to be considered as an object with hadronic structure. The photon structure relevant to resolved photoproduction can be related to the the structure of an electron probing an on shell photon with a virtual photon (see. Fig. 1.6). The cross section for an electron probing the structure of the photon is analogous to deep inelastic electron proton scattering and given by

$$\frac{d^2\sigma_{e\gamma\to eX}}{dxdy} = \frac{\alpha_s^2(Q^2)}{2\pi}\left[\left[1+(1-y)^2\right]F_2^\gamma(x,Q^2) - y^2 F_L^\gamma(x,Q^2)\right] \qquad (1.13)$$

Analogous to the proton the hadronic content of the photon can be described by a parton density function

$$F_2^\gamma(x,Q^2) = 2x\sum_i e_{q_i}^2 q_i^\gamma(x,Q^2) \qquad (1.14)$$

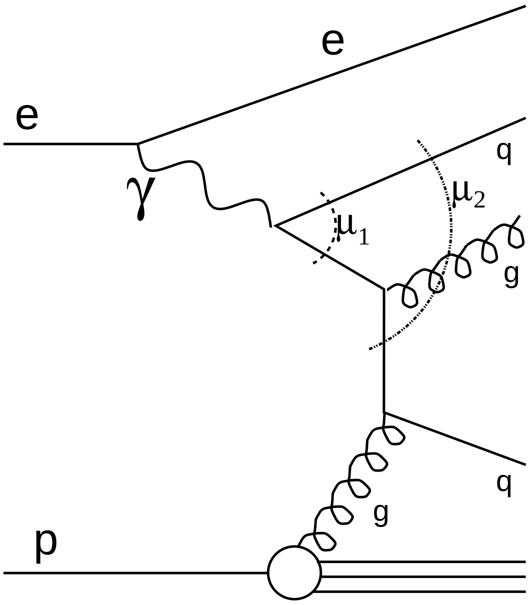

Figure 1.5: This process can be seen as direct or resolved photoproduction, depending on the choice of μ. For $\mu = \mu_1$ this process is accounted as NLO direct photoproduction and for $\mu = \mu_2$ as LO resolved photoproduction process.

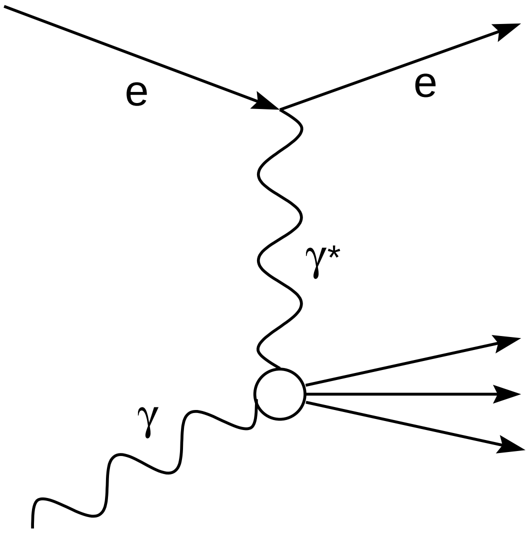

Figure 1.6: Electron probing an on shell photon with a virtual photon.

summing the quarks densities q_i^γ in the photon over all quark flavors i with charge $e_{q_i}^2$ and the antiquarks with $x = Q^2/(2\mathbf{p}\cdot\mathbf{q})$ and $y = Q^2/(sx)$.

The Q^2 dependencies of the parton densities can be calculated according to [DJS+79]

$$\frac{dq_i(x,Q^2)}{d\log Q^2} = a(x) + \frac{\alpha_s(Q^2)}{2\pi}\int_x^1 \frac{dy}{y}\left[P_{qq}(x/y)q_i(y,Q^2) + P_{qg}(x/y)g(y,Q^2)\right] \tag{1.15}$$

with

$$a(x) = 3e_i^2\frac{\alpha}{2\pi}(x^2 + (1-x)^2) \tag{1.16}$$

and the splitting functions $P_{jk}(x/y)$ which represent the probability of a parton j emitting a parton k and then having the momentum fraction x/y.

1.3 Charm in Photoproduction

In the definition of the coupling constant of the strong interaction α_s a dimensional parameter is used. This parameter is called Λ_{QCD} and represents the scale at which the coupling gets too large in order to apply perturbative calculation techniques. Λ_{QCD} is in the order of 200 MeV [ESW96]. Quarks with a mass which is considerably higher than the value of the Λ parameter ($m_q \gg \Lambda_{QCD}$) are regarded as "heavy" quarks. The charm, bottom and top quarks are "heavy". Their mass can be used as a hard scale (scale $\gg \Lambda_{QCD}$) in perturbative quantum chromo-dynamics (pQCD) calculations. By using this hard scale the cross sections for heavy flavor production in hadron-hadron, photon-hadron and electron-hadron collisions can be reliablely calculated in perturbative quantum chromo-dynamics pQCD. The short-distance cross sections are calculable as a perturbation series in the running coupling constant with corrections which are suppressed by powers of the heavy quark mass [EK88] [CSS86]. Therefore measuring charm production is a good test for pQCD.

Two types of NLO calculations are available for comparison with measurements of charm photoproduction at HERA. The massive charm approach [FMNR94] [FNR95] assumes light quarks to be the only active flavors within the structure functions of the proton and the photon, while the massless charm approach [CGRT97a] [CGRT97b] [BKK97] also treats charm as an active flavor.

1.3.1 Perturbative Formalism for Heavy Quark Photoproduction

In the absence of any hard scale photoproduction cross sections can not be calculated. According to [EN89] the total cross section for the inclusive production of heavy-quark pairs, can however be calculated to the order $\mathcal{O}(\alpha_s^2\alpha_{em})$.

For the process

$$\gamma(p_1) + H(p_2) \rightarrow Q(p) + X \tag{1.17}$$

the total cross section for a photon-hadron center of mass energy s is given by

$$\sigma(s) = \sum_j \int dx \hat{\sigma}_{\gamma j}(xs, m^2, \mu^2) F_j^H(x, \mu) + \sum_{i,j} \int dx_1 dx_2 \hat{\sigma}_{ij}(x_1 x_2 s, m^2, \mu^2) F_i^\gamma(x_1, \mu) F_j^H(x_2, \mu) \tag{1.18}$$

The functions F_i^γ for the photon and F_j^H for the hadron are the parton densities of the light partons, s is the square of the center-of-mass energy of the colliding photon-hadron system and m the mass of the produced heavy quark.

The total short-distance cross section $\hat{\sigma}$ for the inclusive production of a heavy quark in a photon proton collision can be written as

$$\hat{\sigma}_{\gamma j}(s, m^2, \mu^2) = \frac{\alpha_{em}\alpha_s(\mu^2)}{m^2} f_{\gamma j}(\rho, \mu^2/m^2) \tag{1.19}$$

with $\rho = 4m^2/s$ and μ being the renormalization and factorization scale. Eq. 1.19 is analogous to the definition of the short distance cross section for the hadroproduction of heavy quarks

$$\hat{\sigma}_{ij}(s, m^2, \mu^2) = \frac{\alpha_s^2(\mu^2)}{m^2} f_{ij}(\rho, \mu^2/m^2) \tag{1.20}$$

The dimensionless functions $f_{\gamma j}$ have the following perturbative expansion.

$$f_{\gamma j}(\rho, \mu^2/m^2) = f_{\gamma j}^{(0)}(\rho) + 4g^2(\mu^2)\left[f_{\gamma j}^{(1)}(\rho) + \bar{f}_{\gamma j}^{(1)}(\rho)\ln(\mu^2/m^2)\right] + \mathcal{O}(g^4) \tag{1.21}$$

1.3.2 "Massive Model" for Heavy Flavor in Photoproduction

In the massive model the number of active parton flavors in the photon is set to 3 [2]. Only the three light quarks (up, down, strange) and gluons contribute to the photon and proton structure function. The charm mass acts to regularize initial state collinear divergences and those from the collinear emission of gluons from the charm quark, with other soft and collinear divergencies canceling between the real and the virtual contribution. Heavy quarks are produced dynamically in the hard subprocess. Therefore only two leading order resolved processes are possible:

$$gg \to cc \quad \text{and} \quad q\bar{q} \to c\bar{c} \tag{1.22}$$

Massive calculations for photoproduction of heavy quarks can be found in [FMNR94]. They are based on hadroproduction calculations [MNR92] [MNR93].

The massive model is reliable in the region $p_\perp^2 \sim m_c^2$. For high $p_\perp$ the $\log(p_\perp^2/m_c^2)$ terms become large. This leads to a diverging series making the calculation unreliable for $p_\perp \gg m_c$.

[2]Therefore this model is also called a fixed flavor scheme

1.3.3 "Massless Model" for Heavy Flavor in Photoproduction

In the massless model also the heavy quarks contribute to the parton density function. Above a certain threshold $\mu^2 \approx m_c^2$ charm is treated as an active flavor with zero mass evolution. Due to charm as an active flavor in the parton density function of the photon and proton in addition to the processes $gg \to cc$ and $q\bar{q} \to c\bar{c}$ additional leading order processes

$$qc \to qc \quad \text{and} \quad gc \to gc \tag{1.23}$$

are present in this scheme. These processes are called "charm excitation" (see Fig. 1.7).

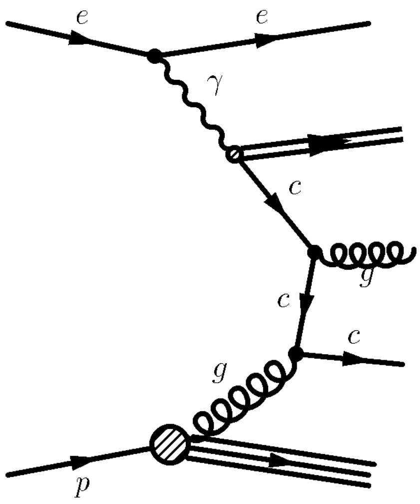

Figure 1.7: Sketch of charm excitation.

The massless scheme allows the resummation of the terms $\ln(p_\perp^2/m_c^2)$ by providing perturbative fragmentation functions for the heavy quark. These fragmentation functions include the logarithmic dependence.

The scale choice μ^2 means that this calculation is not truly massless. The term massless is based on the fact that terms of the form $m_c^2/p_\perp^2$ are neglected.

Contrary to the massive method the massless method is not reliable at $p_T^2 \sim m_c^2$ [CG93]. But for $p_\perp^2 \gg m_c^2$ this method is expected to produce reasonable predictions.

A comparison of the two methods can be found in [Cac97]. Fig. 1.8 shows that both methods give different results for the direct and resolved components. For the sum of direct and resolved, the physical observable, both calculations are in better agreement.

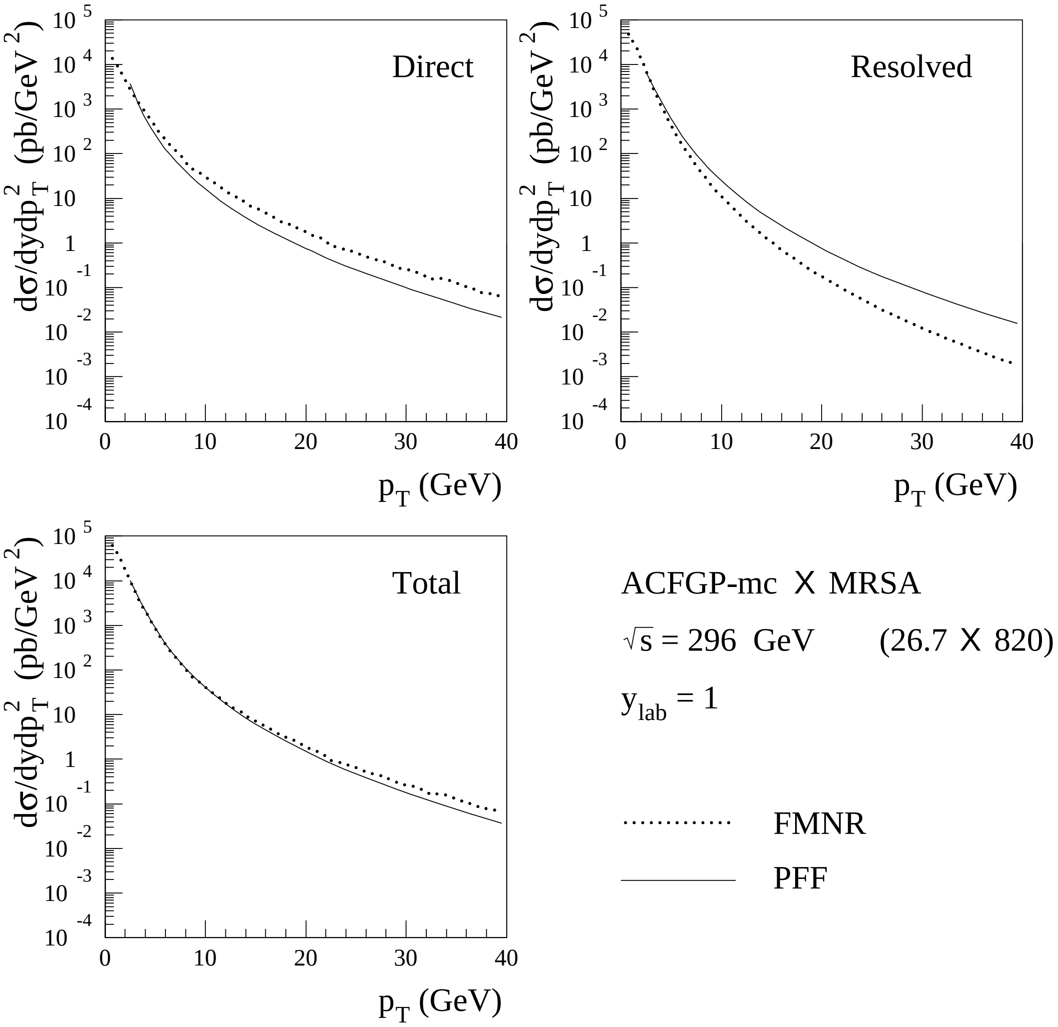

Figure 1.8: Comparison of massive (FMNR) and massless (PFF) calculations (from [Cac97]). The cross section $d\sigma_{\gamma p \to cX}/dydp_T^2$ is plotted as a function of the transverse momentum of the charm quark at a rapidity $y_{lab} = 1$. The upper plots show comparisons between the massless and the masive calculations for direct (upper left) and resolved (upper right) processes. Here a disagreement can be seen. The sum of direct and resolved processed for the massive and the massless calculation is compared in the lower plot. Here the agreement is better than that for each component. The functions used in this plot are not compared to the data measured in the presented analysis since they are not available for the kinematic region of this analysis.

1.4 Charm Identification via D* Decay

Due to the confinement of quarks into hadrons a direct observation of quarks is not possible. It is only possible to measure properties of charm quarks by measuring mesons or baryons containing charm quarks. To extrapolate from the cross sections of the mesons or baryons to those of the charm quarks it is necessary to measure the branching ratio of the charm quark to a certain hadron, for this analysis the D$^{*\pm}$ meson. This was done e.g. at OPAL [OPA95], ALEPH [ALE94] and DELPHI [DEL93] in e^+e^- collisions. According to [Gla99] the average is

$$f(c \to D^{*+}) = 0.232 \pm 0.007. \tag{1.24}$$

1.4.1 Fragmentation

Several models exist which describe the fragmentation of heavy quarks into hadrons. The Peterson fragmentation function [PSSZ83] is a commonly used model. It describes the probability of the transition of a heavy quark Q with the momentum P to a certain hadron $H = \bar{q}Q$ with the momentum zP

$$D_Q^H(z) = \frac{N}{z[1-(1/z)-\epsilon_Q/(1-z)]^2} \tag{1.25}$$

The normalization is fixed by summing over all hadrons containing the heavy quark $\sum \int dz D_Q^H(z) = 1$. The parameter ϵ_Q is of the order of $\mathcal{O}(m_q^2/m_Q^2)$. It can be determined from fits to experimental results from e^+e^- colliders.

1.4.2 The D* Decay

The D$^{*\pm}$ meson decays via different channels. Since the branching ratios to the different channels are known it is possible to measure just one channel and extrapolate to the total number of D* mesons. For an exact mass measurement all final state particles in the selected channel have to be well measured. The decay D$^{*\pm} \to$ D$^0\pi^\pm \to$ K$^\mp\pi^\pm\pi^\pm$ used in this analysis suits this requirement.

This channel has an additional advantage. Due to the kinematics of the process the signal can be observed even in the presence of processes with a much bigger cross section.

According to [PDG00] the mass of the D$^{*\pm}$ and the D^0 meson are $m(D^{*\pm}) = 2010.0 \pm 0.1$ MeV and $m(D^0) = 1864.5 \pm 0.5$ MeV. Since the mass difference of D$^{*\pm}$ and D^0 ,

$$\Delta M = M(D^0\pi_s) - M(D^0) = M(K\pi\pi_s) - M(K\pi) = 145.5\text{MeV} \tag{1.26}$$

is only a bit larger than the mass of the pion, $m(\pi^\pm) = 139.6 MeV$, the $\pi^\pm$ radiated from the D$^{*\pm}$ decay has a small momentum and energy in the center of mass frame of the D*-meson.

$$E_{\pi_s} = \frac{M_{D^{*\pm}}^2 + m_{\pi^\pm}^2 - M_{D^0}^2}{2M_{D^{*\pm}}} \tag{1.27}$$

$$p_{\pi_s} = \sqrt{E_{\pi_s}^2 - m_{\pi_s}^2} = 42.6 \text{ MeV} . \tag{1.28}$$

This small momentum is the reason why this pion is labeled "slow" (π_{slow} or π_s). It is also the reason for the small phase space available for this decay. This leads to a good mass difference resolution. Therefore this signal can easily be separated from the background.

The disadvantage of this method is the relatively small branching ratio. According to [PDG00] the branching ratios are:

$$BR(D^{*\pm} \to D^0\pi^\pm) = 0.677 \pm 0.005 \tag{1.29}$$

$$BR(D^0 \to K^\mp\pi^\pm) = 0.0383 \pm 0.0009 \tag{1.30}$$

$$BR(D^{*\pm} \to D^0\pi^\pm \to K^\mp\pi^\pm) = 0.026 \pm 0.005 \tag{1.31}$$

The combination of 1.24 and 1.31 shows that only 0.6 % of the charm quarks can be detected via this channel.

Other D^0 decay channels also have final states[3] which consist of charged particles only and have larger branching ratios. But these decays suffer from other disadvantages. The $D^0 \to K^\mp\pi^\pm\pi^\pm\pi^\mp$ decay for example has a branching ratio of approx. 7.5 %. The disadvantages of this decay is the high combinatorial background. Charm can also be observed via electroweak semileptonic decays ($c \to l\nu_l X$). The semileptonic branching ratio is higher than for the decay used in this analysis and measured to be 9.5 % [ARG92]. But the semileptonic decays suffer from a large irreducible background [Heb00].

The $D^{*\pm} \to K^\mp\pi^\pm\pi_s^\pm$ decay has a small branching ratio, but allows a very good background suppression. Therefore it was chosen for this analysis.

[3] Final state in this context includes those states where all particles have a decay length which is sufficiently long to be detected in the tracking device.

Chapter 2

Experimental Setup

2.1 HERA

HERA[1], the first electron -proton collider worldwide, is located in Hamburg, Germany. The first collisions were observed in spring 1992.

The two storage rings (see Fig. 2.1) are located in an underground tunnel 15-30m below the surface. Protons and electrons are stored in different rings, the protons move counterclockwise and the electrons (positrons)[2] clockwise. Superconducting magnets are used to generate the bending field for the proton ring. In order to achieve superconductivity the magnets are cooled by fluid helium to a temperature of 4.2 K. The protons are accelerated up to an energy of 920 GeV. The electron energy is limited to 30 GeV (design value) by the energy needed to compensate the energy loss by synchrotron radiation. In the years 1996 and 1997, relevant for this analysis, the electron energy was 27.5 GeV and the proton energy was 820 GeV (see table 2.1).

The proton and the electron beams collide head on in two different experimental areas. The H1 and ZEUS experiments are large acceptance colliding beam experiments and are located in the north and in the south hall. The HERMES experiment situated in the east hall uses just the longitudinally polarized electron beam to measure the spin structure of nucleons. The HERA-B experiment in the west hall uses only the proton beam and was designed to measure CP-violation in the b-quark system produced in hadron-hadron collisions.

2.2 The ZEUS Detector

The ZEUS detector (see Fig. 2.2, 2.3) is a multi purpose large acceptance detector. Its main components are a uranium calorimeter and a multi-wire tracking chamber. It is designed to study various aspects of electron proton interactions. In the tracking component the direction

[1]Hadron-Elektron-Ring-Anlage

[2]The HERA machine can accelerate electrons as well as positrons. They were used at different times: 1992,1993: electron; 1994 - 1997 positrons; 1998 - May 1999 electrons; May 1999 - August 2000 positrons

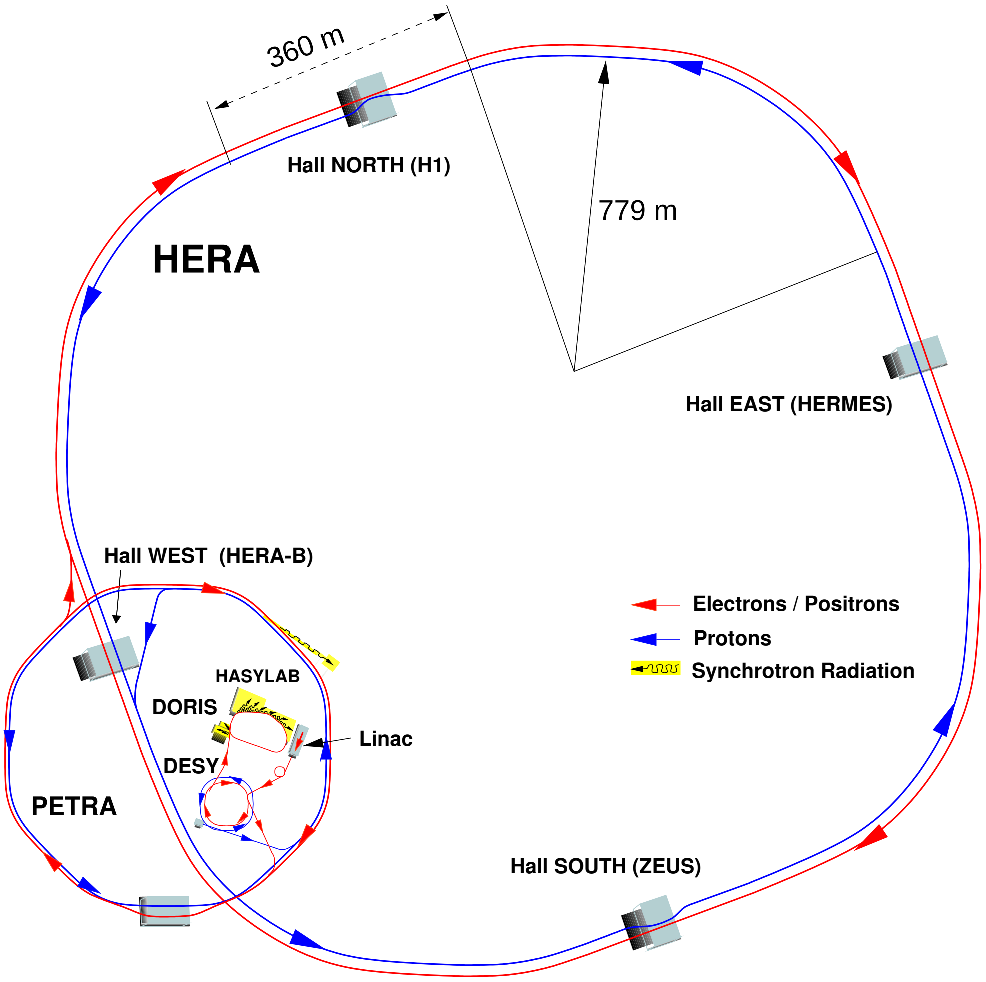

Figure 2.1: HERA Collider with pre-accelerators. The electrons / positrons move clockwise and the protons counterclockwise. The ZEUS experiment is situated in the south hall of the HERA collider.

and momentum of charged particles are measured. The surrounding calorimeters measure the energy of charged and neutral particles.

Due to the imbalance of proton and electron (positron) beam energies more particles are scattered in the direction of the proton beam. Therefore the detector setup is asymmetric in the z-direction[3]. The detector covers 99.7 % of the 4π solid angle. Just the area where the beampipe enters and leaves the detector are not covered. A more detailed description of the detector can be found in [ZEU93].

[3]In the right-handed ZEUS coordinate system the positive z-axis is pointing in the direction of the proton beam. This is also called forward direction. The x-axis is pointing to the center of the accelerator and the y-axis is pointing upwards. The origin of the coordinate system is defined by the center of the central tracking detector.

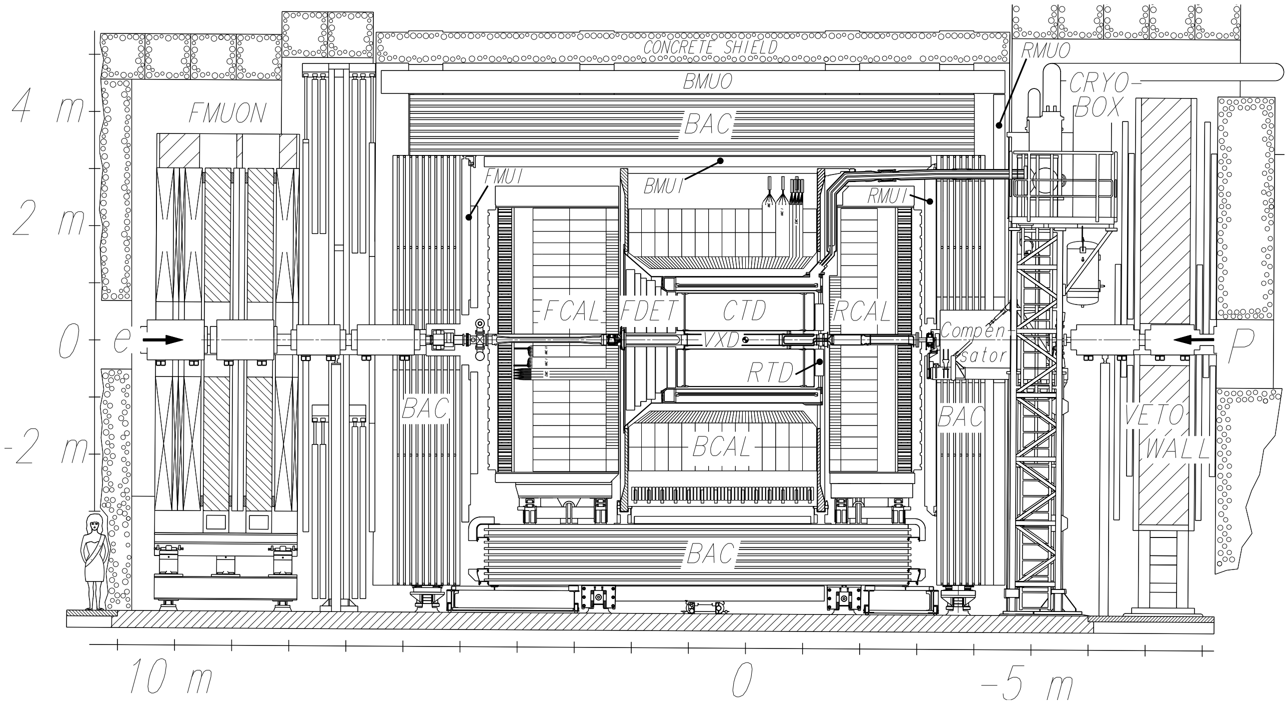

Figure 2.2: Longitudinal section of the ZEUS Detector (along the beam axis).

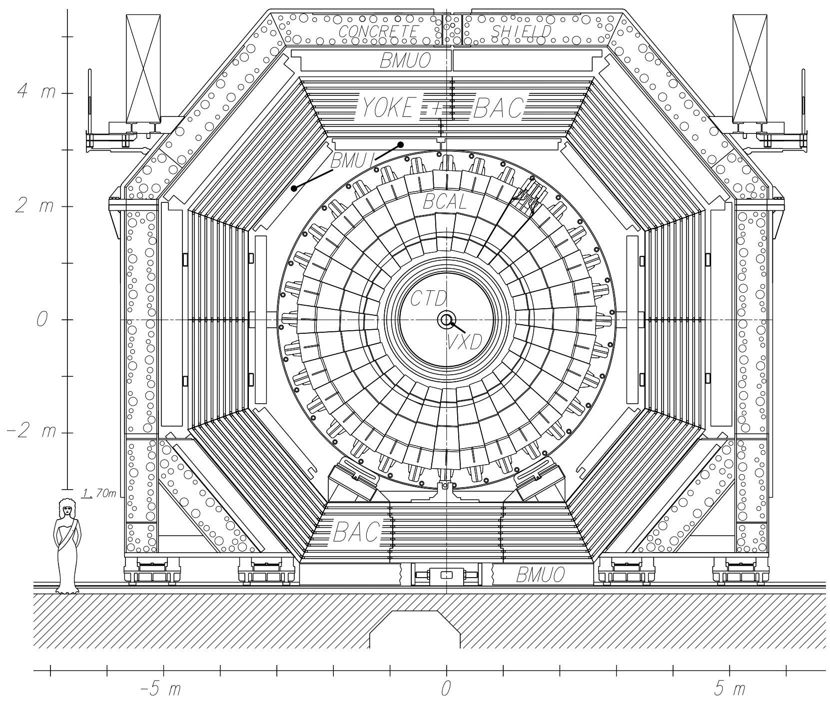

Figure 2.3: Transverse section of the ZEUS Detector (transvers to the beam axis).

	design values		1996		1997	
particle type	p	e^-/e^+	p	e^-/e^+	p	e^+
beam energy [GeV]	820	30	820	27.5	820	27.5
center of mass energy	314		300		300	
circumference [m]	6336					
number of bunches	210	210	174	174	174	174
number of unpaired bunches	-	-	6	15	6	15
time between bunch crossings [ns]	96		96		96	
integrated luminosity (per year) [pb^{-1}]	50		17.2		36.4	
magnetic field [T]	4.68	0.165	4.68	0.15	4.68	0.15
beam currents [mA]	163	58	≈ 70	≈ 30	≈ 80	≈ 40

Table 2.1: Technical parameters of the HERA collider

2.2.1 Tracking

The main part of the ZEUS tracking system is the central tracking detector (CTD). There are additional drift chambers in the forward (FTD[4]) and backward (RTD[5]) direction. The forward region is also covered by a transition radiation detector (TRD). The small angle rear track detector (SRTD) [Ng93] [NV95] improves the track reconstruction for particles scattered in the backward direction close to the beampipe.

2.2.1.1 Central Tracking Detector

The central tracking detector (CTD) is situated in the center of the detector. It is surrounded by a superconducting solenoid producing a magnetic field of 1.43 T. The detector is a jet-type drift chamber which covers the full azimuthal angle and a polar angle of $15^o < \theta < 165^o$. Its active volume has a length of 203 cm with inner and outer radii of 19 and 78.5 cm respectively.

The CTD is filled with a mixture of argon and ethane. A traversing charged particle ionizes atoms from the gas mixture. Electrons resulting from this ionization process move along the electric field produced by field wires. Close to the cathode wires the electrons produce an avalanche of electrons which is measured on the signal wires. By combining several of those measurements tracks of charged particles are reconstructed.

[4] Forward Track Detector
[5] Rear Track Detector

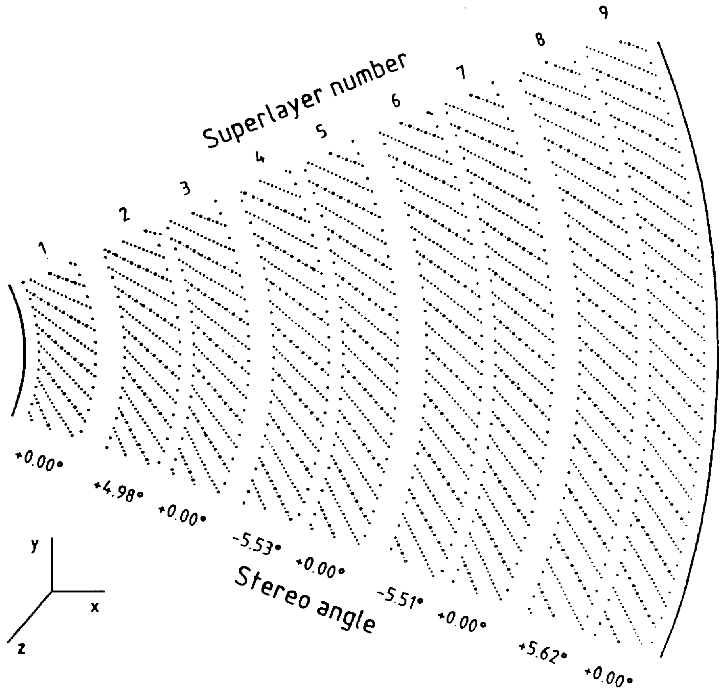

Figure 2.4: Wires in one octant of the Central Tracking Detector (CTD). The numbers in the lower part show the angle of the wires relative to the beam axis.

The 4608 sense wires are ordered in 72 concentric layers arranged in 9 superlayers. Each superlayer is divided into cells with 8 sense wires in each. The number of cells per superlayer increases from the inner to the outer layer. Superlayer 1 consists of 32 cells and superlayer 9 of 96. The cells are tilted by approximately 45^o in order to resolve left-right ambiguities of hit positions w.r.t. the signal wires and to prevent particles from escaping undetected between two cells. Each sense wire is read out every 9.6 ns with an accuracy of 8 bit by flash analog to digital converters (FADCs). The position resolution of the CTD in (r, ϕ) is 190 μm. The wires in the superlayers with odd numbers are oriented parallel to the beampipe. Those in the superlayers with even numbers are tilted by approximately $5°$. By combining the signals from the odd and the even superlayers one can determine the z-position of the resulting track. This method is called "z-by stereo". This leads to a reconstructed z-resolution of approx. 1.5 mm for the reconstructed tracks. One can also determine the z-position of a hit by comparing the arrival time of the signal on both ends of a sense wire. This so called z-by-timing method leads to a z-resolution of 4.4 cm and is mainly used for triggering.

2.2.2 Calorimeter

Calorimeters measure the energy of particles. This can be done by absorption in a medium that becomes ionized or excited in a shower process. The energy deposit in the calorimeter is proportional to the energy of the incoming particle. The energy measurement can

angular coverage	$15^o - 165^o$
max. drift time	≈ 500 ns
resolution (x-y plane)	190 μm
z-resolution (timing)	< 4.5 cm
z-resolution (stereo)	1.0 - 1.4 mm
double track resolution	< 2.5 mm
vertex resolution (x-y plane)	1 mm
vertex resolution (z - direction)	4 mm
magnetic field	1.4 Tesla
$\sigma(p)/p$ for $\theta = 90^o$	0.0021p(GeV/c) $\oplus$ 0.0029
dE/dx resolution	< 6 %

Table 2.2: Technical parameters of the CTD. The values for momentum resolution and dE/dx are valid for tracks which have hits in all 9 superlayers. $\oplus$ indicates quadratic summation ($a \oplus b = \sqrt{a^2 + b^2}$).

be either continuous or alternating. The latter is called sampling calorimeter. The particles deposit their energy in the absorber and are measured in the scintillator. It is called sampling calorimeter since the total amount of absorbed energy can be reconstructed from the statistical sample of the energy deposit in the active material.

2.2.2.1 The Uranium Calorimeter

The CTD and the magnet are enclosed by a high resolution uranium-scintillator compensating calorimeter. It consists of a central cylindrical calorimeter (BCAL)[6], a disk-like forward (FCAL)[7] and a disk-like backward calorimeter (RCAL)[8] (see Fig. 2.5). All three parts are constructed as sampling calorimeters. They consist of alternating layers of depleted uranium (DU) and scintillator as active material. The thickness of the two components (2.6 mm scintillator and 3.3 mm uranium) have been chosen to achieve an optimal compensation of the calorimeter. In a compensating calorimeter electromagnetic and hadronic showers of equal energy produce equal signals ($e/h = 1$). Depleted uranium as absorber was chosen for its compensation capability [KW89].

SCSN-38 is used as scintillator. It is an organic material which emits blue light upon the trespassing of charged particles. Several alternating layers of scintillator and absorber form

[6]barrel calorimeter
[7]forward calorimeter
[8]rear calorimeter

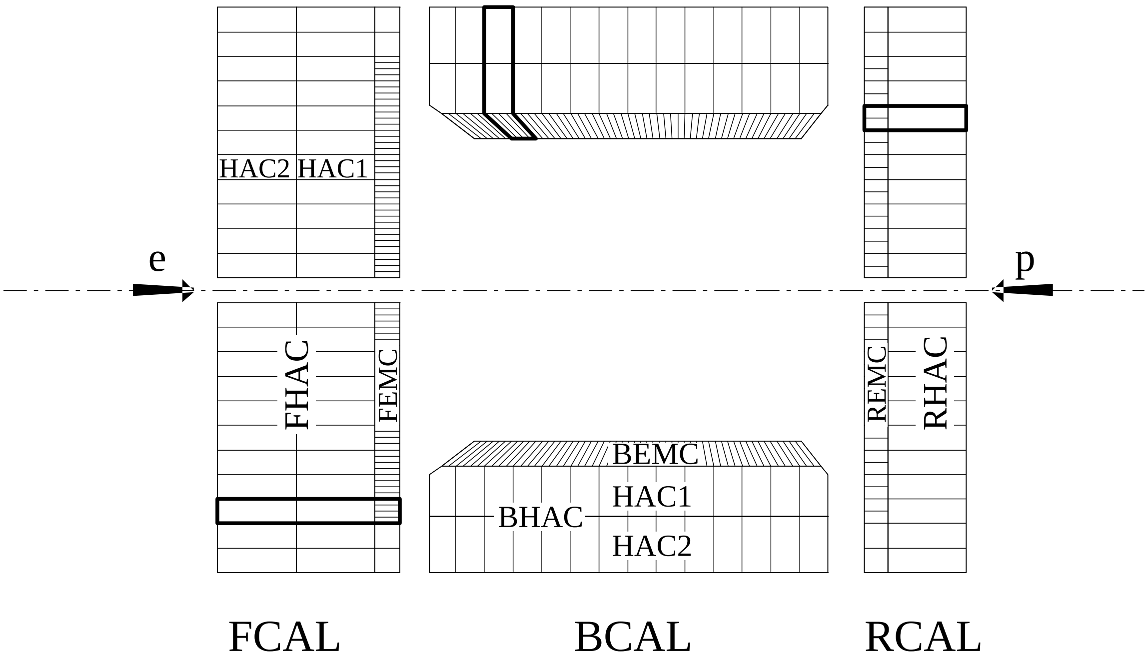

Figure 2.5: Overview of the uranium calorimeter (y-z plane). The areas marked with thick lines enclose the cells belonging to a single tower. The EMC parts have a granularity in the y-direction which is four times (RCAL two times) finer than those in the HAC sections. The granularity in the x-direction is the same for the EMC and HAC sections.

polar angle coverage (FCAL)	$2.6^o - 36.7^o$
polar angle coverage (BCAL)	$36.7^o - 129.1^o$
polar angle coverage (RCAL)	$129.1^o - 176.2^o$
energy resolution (hadrons)	$35\%/\sqrt{\mathrm{E[GeV]}}$
energy resolution (electrons)	$18\%/\sqrt{\mathrm{E[GeV]}}$
position resolution in x-direction (hadrons)	$6.5\ \mathrm{cm}/\sqrt{\mathrm{E[GeV]}}$
position resolution in x-direction (electrons)	$6.7\ \mathrm{cm}/\sqrt{\mathrm{E[GeV]}}$
position resolution in y-direction (hadrons)	$5.4\ \mathrm{cm}/\sqrt{\mathrm{E[GeV]}}$
position resolution in y-direction (electrons)	$1.5\ \mathrm{cm}/\sqrt{\mathrm{E[GeV]}}$

Table 2.3: Technical parameters of the calorimeter. The values for energy resolution and position resolution have been measured in a test beam.

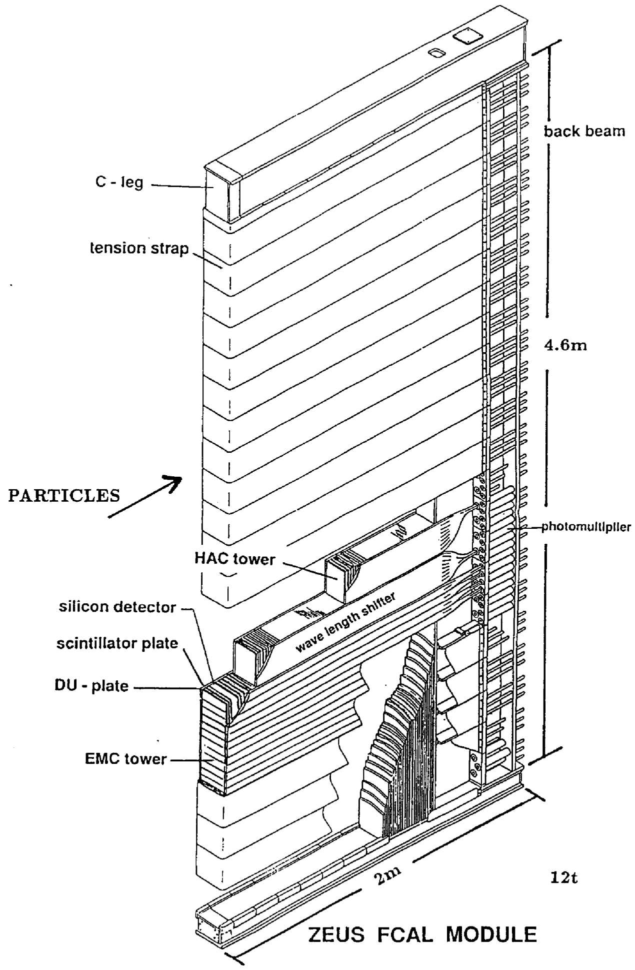

Figure 2.6: A single calorimeter module. The module shown is part of the forward calorimeter.

a cell. This light emitted from all scintillators of one cell is collected by wave-length shifters on both sides of the cell. In the wave-length shifters the light is transformed to green light. This green light is guided by optical fibers to photomultipliers. Each cell is read out by two photomultipliers, on each side (see Fig. 2.6). By evaluating the signal difference one can increase the horizontal resolution in the FCAL and the RCAL and the radial resolution in the BCAL. Angular coverage and energy resolution are shown in table 2.3.

The calorimeter sections are divided into vertical (FCAL and RCAL) or radial (BCAL) modules which are subdivided in towers (see Fig. 2.5). To distinguish between electromagnetic (e,γ) and hadronic (e.g. $\pi^{\pm}$, p, n) showers each tower in the calorimeter is longitudinally divided into three sections (RCAL: two sections) with separate read-out (see Fig. 2.6). The innermost part is the electromagnetic calorimeter (EMC) followed by the hadronic parts HAC1 and HAC2 (in the RCAL there is only HAC1). The depth of the HAC parts is $2 \cdot 3\ \lambda$ in FCAL, $2 \cdot 2\ \lambda$ in BCAL and $1 \cdot 3\ \lambda$ in RCAL[9]. An electromagnetic shower deposits

[9] λ: absorption length

most of its energy in the EMC (depth of EMC: 25 radiation length; $25X_0 \approx 1\lambda$)[10] while a hadronic shower deposits most of its energy in the HAC sections. An electromagnetic shower has a much smaller transverse size.To achieve a better angular resolution the EMC cell in one tower is divided into four parts of $5 \times 20\text{cm}^2$ (RCAL: $10 \times 20\text{cm}^2$).

The calorimeter is calibrated on a channel-by-channel basis using the radioactive decay of U^{238}, which provides a constant reference signal. This calibration procedure is good to 1% [ZEU93].

2.2.3 Electron Tagger

In addition to the main calorimeter the scattered electron can be identified in three taggers. These taggers are placed 8m, 35m and 44m downstream[11] from the interaction point (see Fig. 2.7). The 44m tagger is used in this analysis to tag the scattered electron.

2.2.3.1 44m Tagger

The 44 meter tagger (see Fig. 2.8) is placed 44m away from the interaction point next to the beam pipe. An electron scattered at a very small angle leaves the beam pipe through a copper window into the tagger. The position of the tagger relative to the interaction point and to the beam magnets limits the kinematic range of events which can be tagged by this device. The tagger has a front size of $70 \times 90\text{mm}^2$. It is constructed as a sampling calorimeter with alternating plates of tungsten and scintillator (SCSN-38). The depth is $24X_0$.

2.2.4 Trigger and Online

The HERA collider produces one bunch crossing every 96 ns which corresponds to a crossing rate of approximately 10 MHz. Only a small fraction of events is useful for physics analysis. ZEUS uses a three level trigger system to keep as many interesting events as possible and to remove as many background events as possible. The background is dominated by beam gas events.

- In the first level trigger (FLT) the data are separately analyzed in each detector component. The results are sent to the general first level trigger (GFLT) which decides within 55 bunch crossings whether the event is accepted or not. During this time the measured values are stored in a pipeline at each component. The rate of events accepted by the FLT is up to 600 Hz.
- All the data of all events accepted by the GFLT are digitized and transfered to the second level trigger (SLT, GSLT). This trigger consists of several processors working in parallel on the same event. Due to the lower input rate this level can already use

[10] X_0: radiation length
[11] in negative z-direction

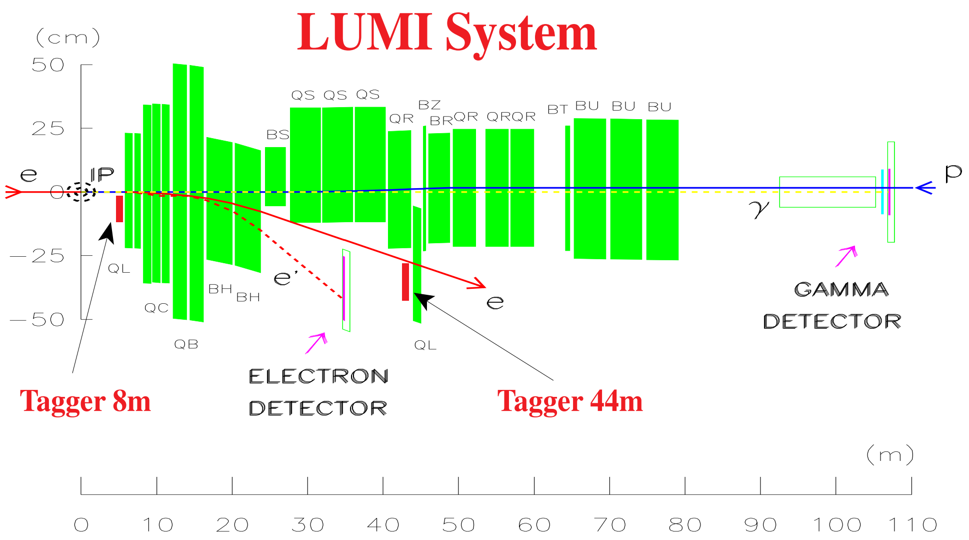

Figure 2.7: The luminosity monitor system, the 8m and the 44m taggers. The luminosity monitor system and the 44m tagger are located in the HERA tunnel. The hatched areas are the HERA magnets.

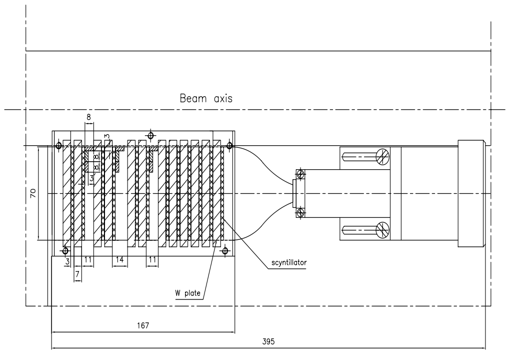

Figure 2.8: Layout of the 44m tagger.

complex objects like vertices and tracks to decide upon the acceptance of an event. After the SLT the rate is lowered by one order of magnitude to approx. 70 Hz.

- All events accepted by the SLT are fully reconstructed in the eventbuilder. The third level trigger can use these data to decide whether an event is taken or not. The output rate of the TLT is 5 – 10 Hz. All the events accepted by the TLT are written to tape in the DESY computing center.

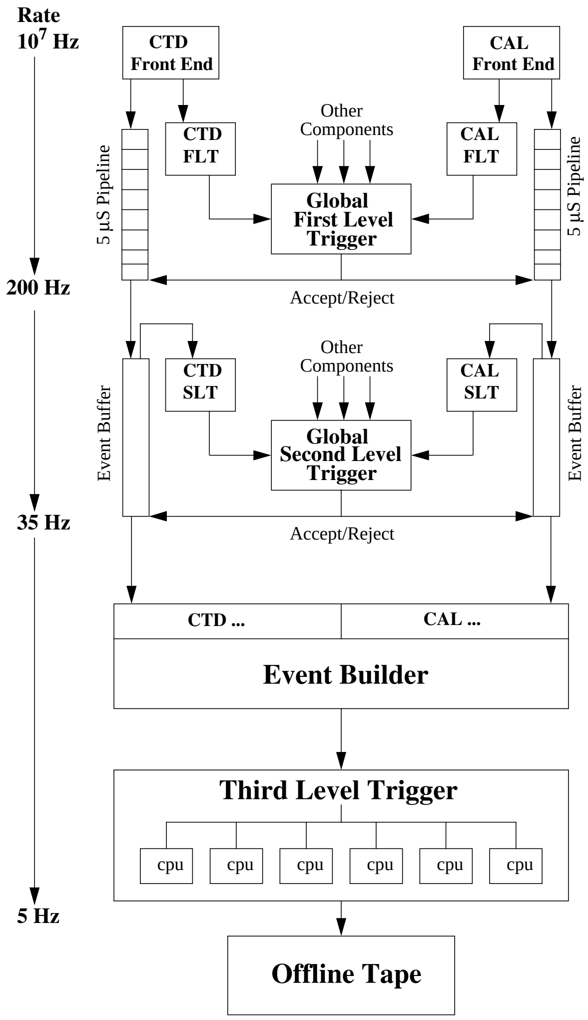

Figure 2.9: ZEUS trigger system. The trigger system starts at the top with the FLT. The second step is the SLT. The event builder already belongs to the third step the TLT.

2.2.5 Reconstruction, Data Storage and Analysis Software

Some of the detector components need calibration constants calculated on a run by run basis. Therefore the reconstruction can not start before all events of a run are written to tape. This requirement decouples the data taking from the offline reconstruction. In the reconstruction process the raw data of a run are read from disk. All events are completely reconstructed and the result is written to disk. Just the reconstructed data which is relevant for physics analysis is written to MDST[12]-files in ADAMO format [FP94]. This is an easily accessible and well structured format. All data are stored in tables and relations between different tables are supported. During the offline reconstruction all events are classified by

[12] medium data storage tape

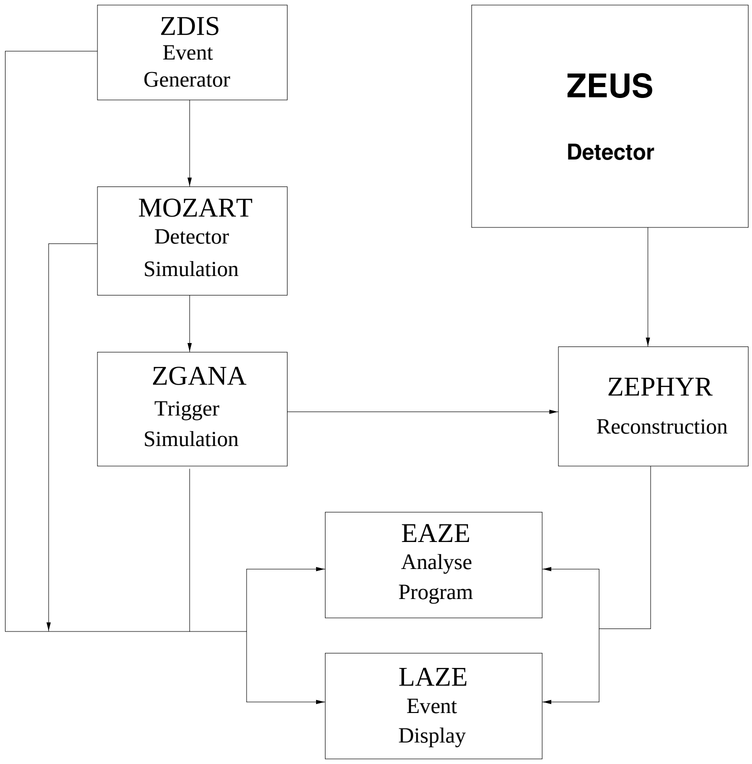

Figure 2.10: ZEUS dataflow

128 boolean variables (DST-bits).

2.2.6 Monte Carlo

Events generated by a Monte Carlo simulator are converted to a common format. These data are processed by a detector simulation program (MOZART) based on GEANT. The output of the simulated detector is analyzed by a trigger simulation (ZGANA). The final output of this process (see Fig. 2.10) is similar to the one coming from the detector. Only information about the generated process is added.

The data written to disk are used for physics analysis.

2.3 ZES

To increase the flexibility of the 128 boolean variables for event selection a new system was introduced at ZEUS [BFHS+01] [Sto98]. ZES[13] stores 200 physics variables (e.g. x, y and Q^2) per event. These variables are stored in an object oriented database[14].

[13]ZEUS Event Storage

[14]The ZEUS experiment has chosen the Objectivity database for this purpose

2.3.1 Design and Implementation of ZES

The data of the ZEUS experiment which are used for physics analysis are stored in sequential ADAMO files. Each run is split up into files with roughly 2000 events. Before the introduction of ZES an additional index file was generated for each run. In this index file the run number, the event number, the name of the file which contains this particular event, the offset of this event in the file and 128 boolean variables (also called bits) are stored for each event. These bits are filled during the reconstruction process.

In this framework (called ZEUS Event Directory, ZED) it was only possible to preselect upon these 128 boolean variables whether an event should be used for a physics analysis. By using this technique the user was limited to the threshold values for the physics variables which were applied at the time of the reconstruction. For a selection of events for which no suitable bit existed it was necessary to use a logical combination of different bits which could have resulted in a huge overhead of events.

To solve this problem an object oriented database was developed which allows to select events based upon roughly 200 physical variables. To emphasize the databases structure of this technique it is called a tag database.

Some requirements were set for the implementation of this tag database.

- It should be integrated in the existing software with a minimum of changes in the existing programs.
- The steering should be done in a way similar to those used for the bits.
- It should be fully transparent for those users which still use the old technique.

The ZED was implemented by a main function which returns a pointer to the file and the offset of the event which is to be read next. This allows the analysis program to access the next event in the fastest possible way. Therefore this general technique was kept but the file and the offset in the file is now returned by the tag database. Since the tag database has to return the filename and the offset for every event to the analysis routine it is necessary to store them in addition to the physics variables.

The Objectivity database stores data in a so called federation. Therefore it is also called a federational database (FDB). A federation is split up into different physical files. In a file the data objects are stored in so called containers. In the ZES case a container represents a run. Several run-containers are stored in one file. Every event is represented by a single object in the appropriate run container. The file object contains information about the run number, the event number, the offset of this event inside the sequential file and a pointer to an object which represents the file the event is stored in. This file object is of course the same for all events stored in the same file.

Since the analysis job is written in FORTRAN and the Objectivity database has to be programmed in C++ is necessary to implement a FORRTAN callable C++ function and a C++ function which is able to read FORTRAN data structures.

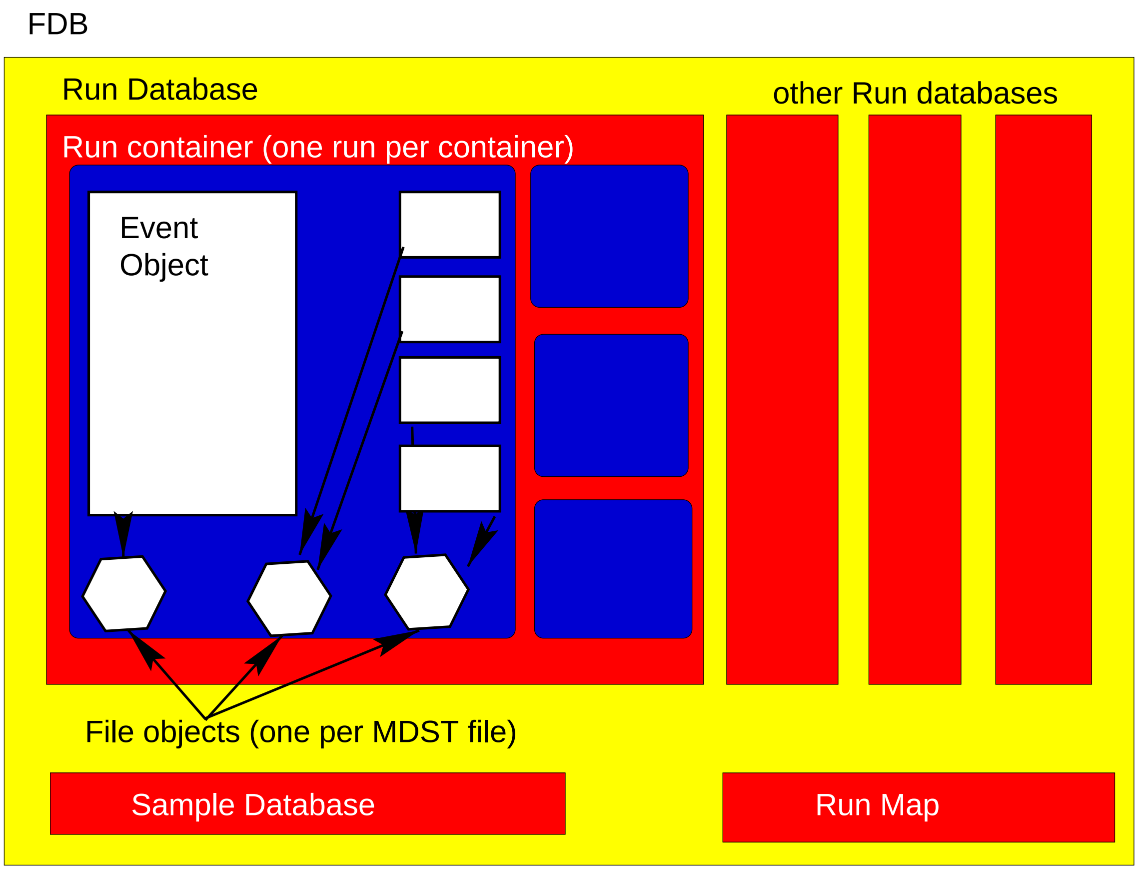

Figure 2.11: ZES Database Schema. The outermost box represents the whole database, the so called federation. The next boxes represent the physical files storing the information of several runs. All information belonging to one run is stored in a container, represented by the next box. In a container every event is stored as an object. In addition an event for each file belonging to a run is stored in the container. From every event object a pointer points to the file object which represents the file the event is stored in.

Chapter 3

Monte Carlo Simulation

Some information is lost in every measurement. One reason is the limited geometrical acceptance of the ZEUS detector, it is not a full 4π detector. This information loss can affect the D^* meson measurement. Therefore the measurement has to be corrected for detector and trigger system acceptances. Due to the high complexity of the system consisting of the physics process, the detector and the trigger, Monte Carlo techniques are used to simulate the physics process as well as the detector response to calculate acceptances.

The simulation is divided into two main parts. The first step is the simulation of the ep scattering process and the simulation of the hadronisation of the final state particles. In the second step the interaction of the generated particles traversing the detector and the response of the detector and the trigger system is simulated.

3.1 Simulation of the Physics Process

The physics process is simulated by programs which are called "event generators". These generators divide the simulation of the scattering process into different phases (see Fig. 3.1). This separation is based on the factorization theorem (see Sec. 1.2.3).

In the first step the hard subprocess is calculated based upon LO QCD matrix elements for charm photoproduction. Flavor and momentum of the incoming parton is chosen according to the selected parton density function (PDF) [PB95]. The hard subprocess is responsible for the physics characteristics of the event.

In the next step higher order QCD initial and final state radiation is simulated. A common approach is the parton shower method. Here the radiation is simulated by a random number of branchings of one to two partons.

In the hadronisation step the partons generated in the earlier steps are combined into color neutral objects. This process is not yet fully understood. In the generators this process is approximated with a phenomenological model. Two main models exist. The cluster hadronisation [Web84] (see Fig. 3.2(a)) and the string hadronisation [AGIS83](see Fig. 3.2(b)).

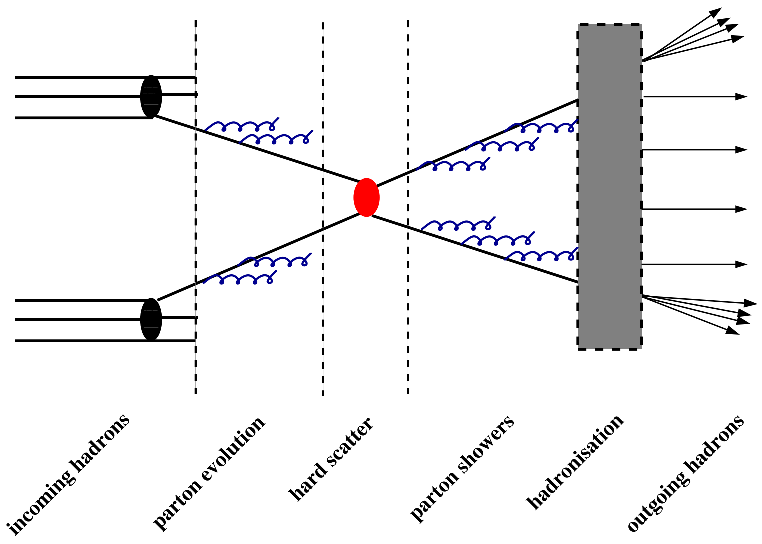

Figure 3.1: Schematic view of the processes in a generator

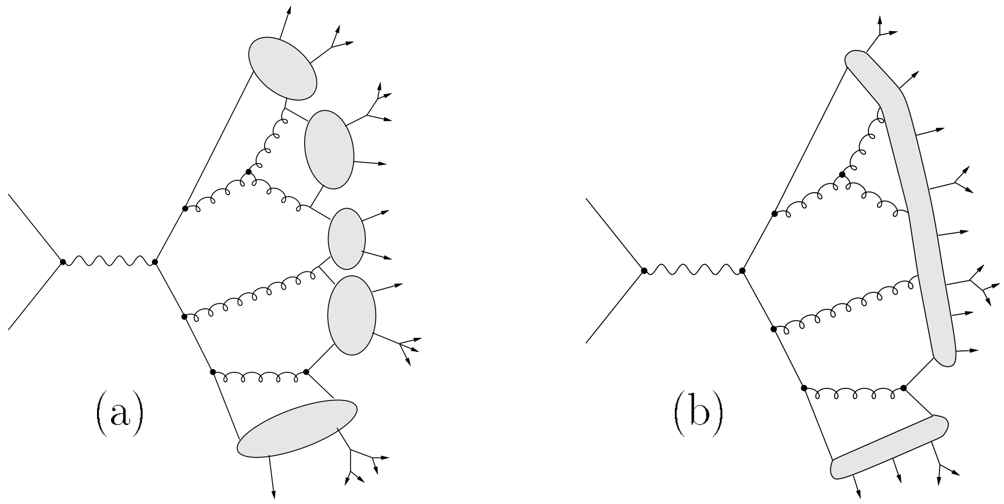

Figure 3.2: Hadronisation Models. (a) shows a sketch of the cluster hadronisation model as used in HERWIG while the string fragmentation model as used in PYTHIA is shown in (b).

In the Lund string fragmentation model the partons are connected by strings with a strength of about 1 GeV/fm. As the partons move away from each other the strings become more energetic. Finally the string is breaking up and produces a $q\bar{q}$ pair. If the energy of the string is too small to allow another separation, hadrons are formed. As the last step the hadrons decay according to their measured lifetimes.

In the cluster fragmentation model in a first step all outgoing gluons are split up into quark pairs. In a next step the quarks are clustered into color neutral objects. These clusters fragment into hadrons which decay as in the string fragmentation model.

In this analysis the HERWIG generator [MWA+92] and the PYTHIA generator [Sjö94] are used. In the following their features are briefly described. A more complete comparison can be found in [B+91].

3.1.1 HERWIG

The Herwig program is a general purpose generator. It is the aim of this generator to provide an implementation of the underlying perturbative QCD process which is as complete as possible. Due to the relatively small number of free parameters this generator has a large predictive power. The authors of the program tried to make the generator as independent from non-perturbative parameters as possible. The entire parton structure is generated based on the hard subprocess. The scale of the hard subprocess is given by

$$\mu^2 = \frac{2\hat{s}\hat{t}\hat{u}}{\hat{s}^2 + \hat{t}^2 + \hat{u}^2} \tag{3.1}$$

with $\hat{s}$, $\hat{t}$, $\hat{u}$ being the Mandelstam variables. For the limit $p_\perp^2 \to 0$ the resulting cross section is divergent. Therefore one needs to introduce a minimal transverse momentum $p_{\perp,min}$. In Herwig direct photoproduction is calculated based upon the exact matrix element. For the resolved process the equivalent photon approximation (EPA, see Sect. 1.2) is used.

The parton shower method is used for the incoming and outgoing partons. Each single parton initiates a shower by splitting up into many partons according to the appropriate splitting functions. Logarithms of the form $\alpha_s \log(\mu^2/\mu_0^2)$ are resummed and the partons are ordered according to their opening angle. The hadronisation in Herwig is based upon a non-perturbative cluster model.

3.1.2 PYTHIA

Like Herwig, the PYTHIA generator is a general propose generator. Although both generators share many common features, PYTHIA's main emphasis is to model the hadronisation phase as completely as possible. In photoproduction the Weizäcker-Wiliam approximation (WWA) is used for direct and resolved events. The hard scale used, is the transverse mass $m_\perp$ of the outgoing parton from the hard subprocess

$$\mu^2 = m_\perp^2 = \frac{1}{2}\left(m_1^2 + p_{1,\perp}^2 + m_2^2 + p_{2,\perp}^2\right) \tag{3.2}$$

with m_1, p_1, m_2, p_2 being the mass and momentum of the outgoing partons. As in Herwig the parton shower method is used to describe the initial and final state radiation. In PYTHIA the emitted partons are ordered according to their virtuality. For the hadronisation the LUND - string fragmentation model [AGIS83] is used.

3.2 Simulation of the Detector Response

After the generation phase all events are handed over to the detector simulation. The MOZART [Haa92] software package takes the information about the generated particles as input parameters and simulates the response of every detector component. This simulation is based upon the simplified model of the material and geometry of the detector components. This software package is based upon the GEANT software library [CAS94] and is calibrated using the test beam results as well as the data gained by physics analyses. The schematics of the dataflow at the ZEUS experiment is shown in Fig. 2.10.

The decision of the component based ZEUS trigger system is simulated by the ZGANA program [WY93]. The ZEPHYR package reconstructs the generated events in the same way as it is done with events measured in the detector. From here on generated and measured events are handled in the same way. The generated events just contain the additional information about the values used in the generation process. These values are also called "true" values.

Chapter 4

Methods

4.1 Track Reconstruction in the CTD

The CTD[1] is able to measure space points along the way of a charged particle. These points are called hits. The x and y component of each hit are reconstructed from the signal of the wires induced by a passing particle. The wires are read out at both ends. The timing difference between the arrival of the signal at the forward and the rear end of the signal wire gives the z component of the hits.

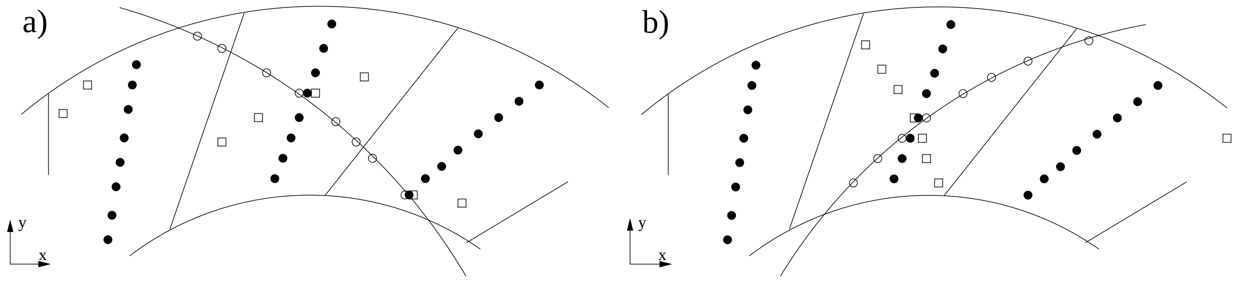

Figure 4.1: CTD cells with a track of a charged particle and the calculated positions of the hits. The solid circles represent the sense wires in a CTD cell. The open circles and open squares are possible hit positions of a track. The open circles indicate the selected positions after the combination of track fragments in different cells. The track shown in the left plot is produced by a particle with negative charge, the one in the right plot is produced by a particle with positive charge. This track is more likely to pass only one cell in a superlayer.

The two different times at the front (t_{front}) and the rear (t_{rear}) end can be seen as a sum of different times

$$t_{front} = t_0 + t_{flight} + t_{drift} + t_{wire,front} \tag{4.1}$$

[1]Central Tracking Detector

$$t_{rear} \quad = t_0 + t_{flight} + t_{drift} + t_{wire,rear} \tag{4.2}$$

where t_0 is the interaction time of the event, t_{flight} the flight time of the particle from the interaction point to the point where the interaction of the particle with the gas in the chamber induces an electron avalanche, t_{drift} the drift time of the electrons to the sense wire and $t_{wire,front}$ ($t_{wire,rear}$) the time the induced electrical signal needs to move along the wire from the point where the electron cascade reaches the sense wire to the front (rear) end of the wire. The time t_0 is given by the HERA machine and t_{flight} mainly depends on the distance of the point where the electron cascade reaches the sense wire and the interaction point. The velocity for the signal moving along the wire is known. Also the velocity of the electron cascade in the gas mixture the CTD is filled with is known. With these parameters one can also calculate the point where the electron cascade was started by the particle. Due to the symmetric shape of the electric field around the sense wire (see Fig. 4.3) one can not determine from which side of the sense wire the cascade originates. Therefore every real hit produces a so called "ghost hit" which has the same z-component, but is situated on the other side of the sense wire (see Fig. 4.1). There is no direct way to distinguish between a hit and the corresponding ghost hit. It is only possible to differentiate between them by combining several hits from different cells to a track.

In a next step hits are combined to tracks. This procedure starts in the outermost superlayer, superlayer number nine[2]. At least three hits from the same cell are combined to a so called "track seed". The track seed is linked to the assumed interaction point at $x = y = 0$. The resulting track candidate is approximated by a circle arc in the x-y-plane. Following this circle arc inward more hits in the superlayers with wires parallel to the beam axis are assigned to the track. The circle arc is rotated outside the x-y plane. A pattern recognition software searches for hits in the superlayers with wires tilted with respect to the beam axis, the so called "stereo layers". The z-position of the whole track is determined by the rotation necessary to superimpose the original circle arc with its components found in the stereo layers. This procedure is repeated with all possible track seeds in superlayer 9. The hits not yet assigned to a track in the other odd superlayers are also treated as track seeds starting from the outer superlayers. This procedure is executed a second time for tracks which do not originate from the main event vertex. Hits in the inner superlayers which could belong to two tracks and can not be clearly assigned to one of the tracks are assigned to the longer one.

The final track candidates are fitted to an ideal helix with five parameters by 'swimming' [HILM96] the trajectory outward. The helix is refined with every added hit. For this procedure a simplified model of the magnetic field inside the CTD is used. The helix (see Fig. 4.2)

$$H(\phi_H, Q/R, QD_H, Z_H, \cot\theta) \tag{4.3}$$

is described by ϕ_H the angle tangent to the helix in the x-y plane at the distance of closest approach, Q/R where Q is the charge of the particle and R being the local radius, D_H the

[2]The odd numbered superlayers (see 2.2.1.1) are axial layers, the even numbered are stereo layers. Wires in the stereo layers are tilted by $\approx 5°$.

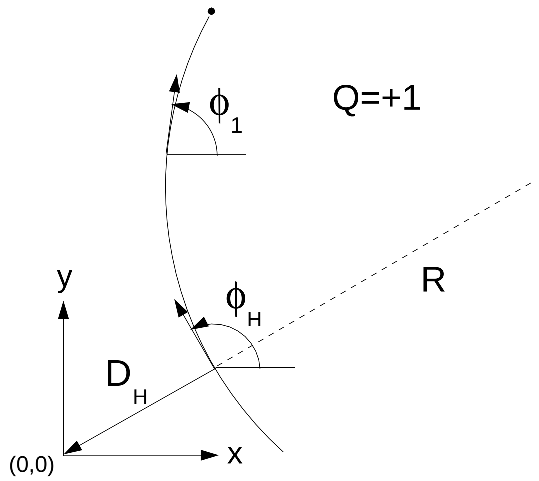

Figure 4.2: Track helix in the x-y plane. D_H is the distance of closest approach of the helix to the reference point $x = y = 0$. ϕ_H the angle tangent to the helix in the x-y plane. The curvature of this track indicates a particle with a positive charge.

distance of closest approach between the helix and the reference point $x = y = 0$, Z_H the z-position of the point of closest approach and $\cot\theta$ where θ is the polar angle.

4.1.1 Differences between positive and negative tracks

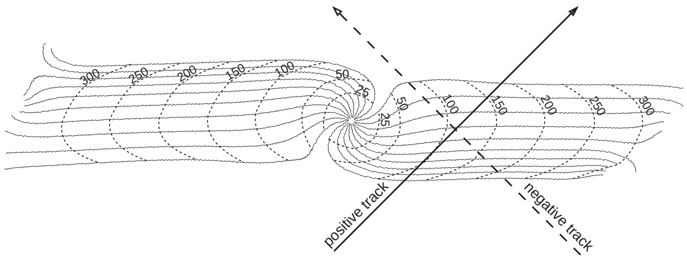

Figure 4.3: Field configuration around a sense wire. The solid lines show the drift paths of electrons from the ionization process around a sense wire. The dashed lines mark points with constant drift time to the sense wire. Positive and negative tracks cross the drift paths at different angles.

In a cylinder symmetric tracking device positive and negative tracks produce the same signal. The ZEUS CTD is not cylinder symmetric. The borders between different cells are not perpendicular to the beam axis. They are tilted (see Fig. 2.4 and 4.1). This geometry does not allow a straight path from the interaction point through the CTD which goes along the cell borders. Such a path would allow particles to escape the CTD undetected along the cell borders. This geometry also helps to distinguish between a hit and a ghost hit (see Fig. 4.1). The track components made of ghost hits end at the cell borders. Those made of real hits can be concatenated over cell borders. The tilt of the cell borders is chosen to be in the direction which prefers negative tracks.

This asymmetry leads to different signals for positive and negative tracks. The magnetic field deflects positive and negative tracks in opposite directions. Due to the asymmetry in the geometry the tracks with different charges cross the electrical field around the sense wires at different angles (see Fig. 4.3). A positive charged particle moves parallel to the lines of constant drift time in the dense electrical field independent of the side on which the particle passes the wire. Therefore the electron avalanches produced by particles with a positive charge reach the sense wire in a small time window. Those avalanches originating from a particle with a negative charge reach the sense wire over a longer period of time, because tracks from negative charged particles start electron avalanches having different drift times to the sense wire. The resulting signal is broader and less pronounced. This lead to a worse spatial resolution. The probability of loosing a hit from a negative track is bigger than for hits from a positive track.

The geometry of the CTD favors negative charged tracks. The form of the electrical field around the sense wire favors positive charged tracks. These effects do not cancel each other completely. The acceptance for positive tracks is better than those for negative tracks. The difference in acceptance is bigger for tracks with a small radius which means a small momentum.

4.2 D* Reconstruction

In this analysis the D* decay is used to indicate the presence of a charm quark. The D* meson reconstruction method [Nus75] is based upon the information from the tracking device. In this analysis the decay channel $\mathrm{D}^{*\pm} \rightarrow \mathrm{D}^0\pi_\mathrm{s}^\pm \rightarrow (K^\mp\pi^\pm)\pi_s^\pm$ is used. The momentum three-vector of a particle at the vertex is calculated from the parameters of the track helix. Particle identification is not possible. Therefore a combinatorial ansatz was chosen where every possible combination of momentum three-vectors is tested whether it is possible to reconstruct a D^* - meson under particular circumstances.

Tracks fulfilling strict quality requirements are selected. One track is assumed to be the kaon, one the pion from the D^0 - meson decay. A third track is assumed to be the π_s from the D* - decay. The quality requirements for this track are reduced.

The forth component of each four vector is calculated with the assumption of the kaon or pion mass as measured in other experiments. The world average is taken from [PDG00]. Based on the four vectors the invariant mass of the $K\pi\pi_s$ system is calculated and treated as the invariant mass of the D*: $M(D^*) = M_{K\pi\pi_s}$. The invariant mass of the $K\pi$ system is treated as the mass of the D^0-meson: $M(D^0) = M_{K\pi}$. The mass difference $\Delta M = M_{K\pi\pi_s} - M_{K\pi}$ is calculated by

$$\Delta M = \frac{M(D^*)^2 M_{\pi^\pm} - M(D^0)}{2M(D^*)^2}. \tag{4.4}$$

This is repeated for every possible track combination. If ΔM and M_{D^0} are inside a defined mass window the combination is called a D* - candidate. The measured ΔM distribution is shown in Fig. 4.4. A clear signal can be seen around 145 MeV. The M_{D^0} distribution is shown in Fig. 4.5. Also here a clear signal is found around the nominal D^0-mass. The difference between the data points and the background estimation can be explained by the additional decay mode $D^* \to K\pi\pi\pi^0$. The neutral pion can not be seen in the CTD. Therefore the reconstructed invariant mass of the D^0 is too small.

The advantage of measuring ΔM instead of $M(D^*)$ is: The four-vectors of the kaon and the pion from the D^0 - decay are used for the calculation of $M(D^0)$ and $M(D^*)$. For the calculation of ΔM these four-vectors are used twice and their errors cancel out. The reconstruction error of ΔM therefore mainly depends on the error of the four-vector of the π_s. The momentum of the π_s is small compared to the one of K and π. Due to the smaller radius of the track, the reconstruction error of the π_s is smaller than those of the K and the π. In addition the small phase space for the π_s in the D* → D$^0\pi_\mathrm{s}$ decay leads to a small error on ΔM even if the error on $p(\pi_s)$ is large.

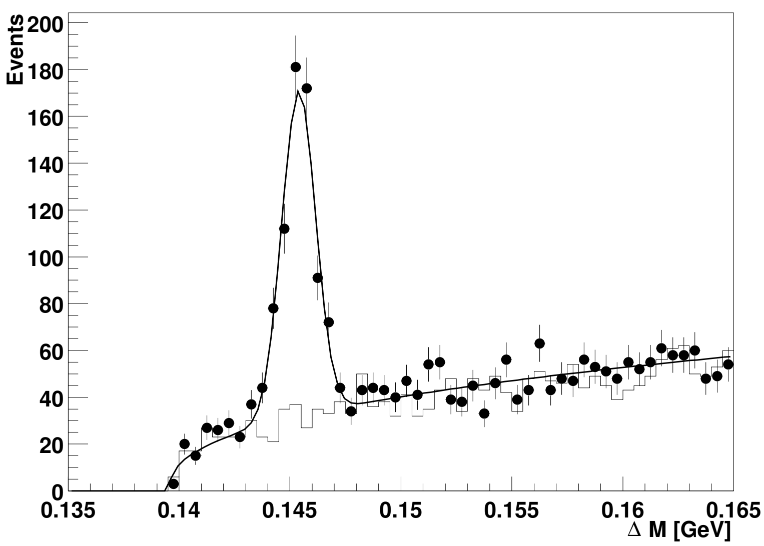

Figure 4.4: ΔM Distribution for events with an electron in the 44m electron tagger. The filled circles are those events with a correct charge combination. The histogram shows the number events with wrong charge combination as a background estimation.

4.2.1 Background

Not all D*-candidates originate from D* decays. Some of them just fulfill the requirements by chance. For a given event it is not possible to distinguish whether the candidate is produced by a D* decay or the required ΔM and $M(D^0)$ values are produced by a statistical

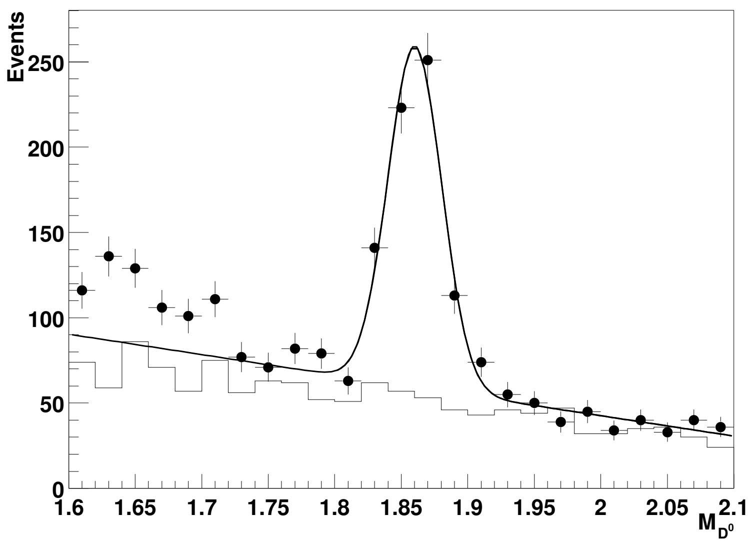

Figure 4.5: Distribution of the reconstructed D^0 - meson mass for events with an electron in the 44m electron tagger. The filled circles are those events with a correct charge combination. The histogram shows the number of events with wrong charge combination as a background estimation.

fluctuation. This so called statistical background is not limited to the D* signal region. To measure the number of D* decays in the sample one has to subtract the number of background candidates from the total number of candidates. Two different methods were used in this analysis to determine the statistical background.

4.2.1.1 Wrong Charge Combination

If the background originates from pure statistical fluctuations, the same result should be obtained for track combinations which fulfill all kinematic requirements, but have incorrectly charged tracks. The two correct charge combinations are: $D^{*-} \to K^+\pi^-\pi_s^-$ and $D^{*+} \to K^-\pi^+\pi_s^+$. The two combinations $K^+\pi^+\pi_s^-$ and $K^-\pi^-\pi_s^+$ can not originate from D*-meson decays because the two high momentum tracks have the same charge and can therefore be used to estimate the background. The combinations $K^-\pi^+\pi_s^-$ and $K^+\pi^-\pi_s^+$ are not used because they may contain valid D^0 candidates. This method determines the background by the so called "wrong charge combinations". The ΔM distributions for the signal[3] (closed points) and the background (histogram) are compared in the region 0.15 GeV $< \Delta M <$ 0.165 GeV to improve the description of the signal by the background estimation. In Fig. 4.6the background is scaled up by $\approx 2\%$.

This method produces stable results as long as D^{*+} and D^{*-} are measured together. If one measures them separately, one can choose two different background combinations which

[3]Signal means the distribution coming from the candidates with right charge combinations.

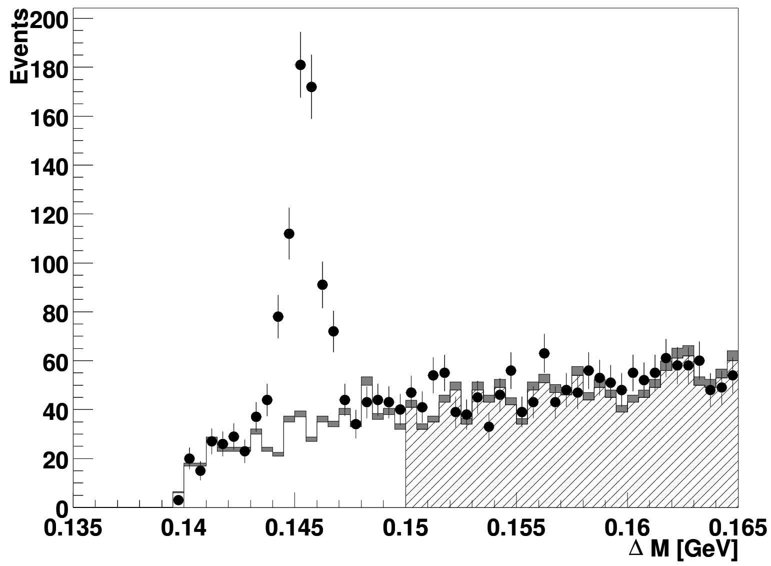

Figure 4.6: Background normalization. The points show the ΔM distribution for track combinations with right charge combination. The histogram shows those with wrong charge combination. In the hatched region the wrong charge distribution is area normalized to the right charge distribution. The cross hatched region at the top of each histogram bin indicates the applied normalization factor.

should lead to the same results. The background for $D^{*-} \to K^+\pi^-\pi_s^-$ can be:

1. $K^+\pi^+\pi_s^-$: The π_{slow} has the same charge as for the signal combination. Due to the small momentum the π_{slow} helix has the smallest radius, therefore its charge can be measured most accurately. But the sum of the charges is different compared to the signal.

2. $K^-\pi^-\pi_s^+$: The sum of the charges is the same as for the signal combination. But the charge of the π_{slow} is different compared to the signal.

Due to statistical fluctuations of the background both methods lead to different results.

It is not unambiguously defined which signal-background combination leads to the better background description. This results in an additional systematical error. If D^{*+} and D^{*-} are measured together both possible backgrounds are used for the combined background. In this case the ambiguity is eliminated.

4.2.1.2 Fitting the ΔM distribution

To avoid the ambiguity of the wrong charge combination background method, the number of D^* events and of background events is directly measured from the ΔM distribution by fitting the background and the signal distributions with the function:

$$\begin{aligned} \Delta M &= A(\Delta M - m_{\pi^\pm})^B \\ &+E \cdot e^{-\frac{1}{2}\left(\frac{x-F}{G}\right)^2} \cdot \frac{w}{\sqrt{2\pi}G} \end{aligned} \tag{4.5}$$

with w being the bin width and A, B, E, F, G being free parameters of the fit procedure. $A(\Delta M - m_{\pi^\pm})^B$ is a parameterization of the background distribution and $E \cdot e^{-\frac{1}{2}\left(\frac{x-F}{G}\right)^2}$ assumes a Gaussian signal. The factor $\frac{w}{\sqrt{2\pi}G}$ normalizes the signal function and E measures the number of D^* - mesons. This method also works for a separate measurement of D^{*+} and D^{*-} mesons because the fit just uses the right charge data distribution.

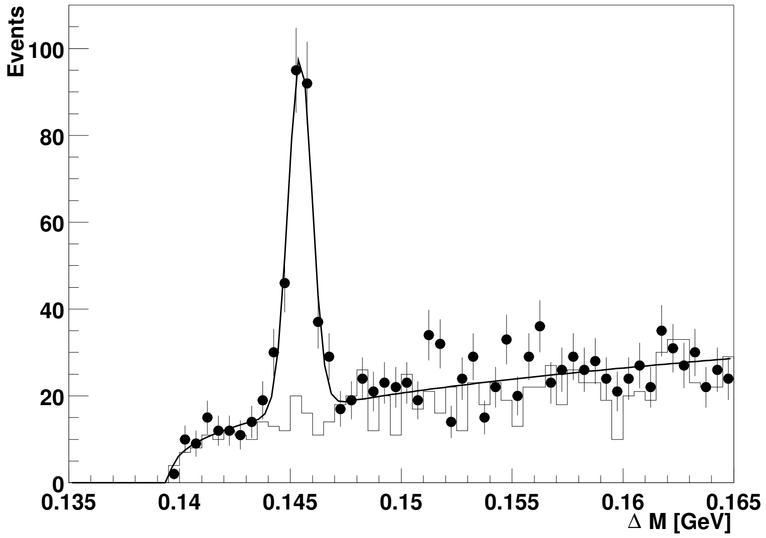

Figure 4.7: ΔM distribution for 44m tagged events with D^{*+}. The filled circles are those events with a correct charge combination. The histogram shows the numbers for the events with wrong charge combination. The wrong charge background chosen here is the one with π_s^+.

4.2.1.2.1 Differences between D^{*+} and D^{*-} As explained in 4.1.1 the momentum of a positively charged track is generally better reconstructed than the momentum for a negatively charged track. This leads to a broader signal for the D^{*-}. In Figure 4.7 and Figure 4.8 it is shown that the width of the fitted Gaussian function is different for D^{*+} and D^{*-}. Therefore a single Gauss functions does not describe the signal for a combined measurement of D^{*+} and D^{*-}.

In most of the measurements in this analysis D^{*+} and D^{*-} are measured together. In this measurements the "wrong charge combination" method is used. In the measurements where the D^{*+} and D^{*-} distributions are compared, the number of D^* events is calculated with a fit to the ΔM signal.

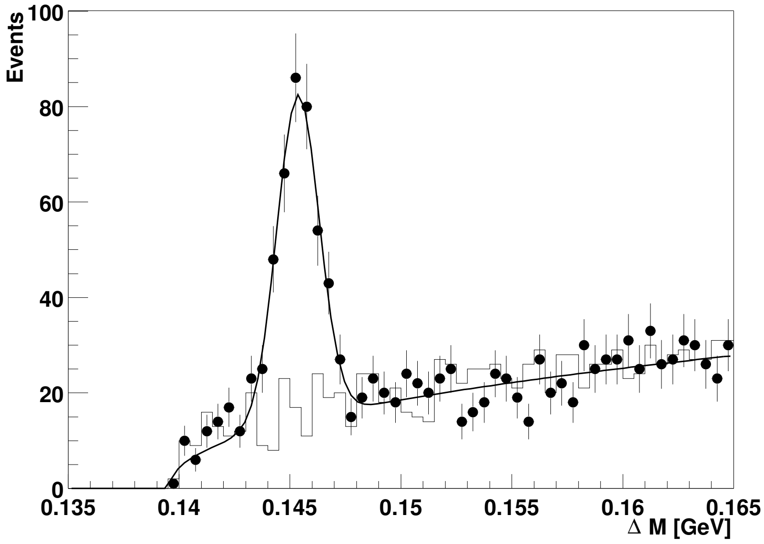

Figure 4.8: ΔM distribution for 44m tagged events with D^{*-}. The filled circles are those events with a correct charge combination. The histogram shows the numbers for the events with wrong charge combination. The wrong charge background chosen here is the one with π_s^-.

4.3 Photoproduction Selection with the 44m Tagger

This analysis is restricted to the photoproduction region where a quasi real photon ($Q^2 \approx 0$) collides with the proton. In general there are two different methods to select photoproduction events. The so called "untagged" method requires no scattered electron found in the main detector. Depending on the geometry and acceptance of the calorimeter a scattered electron found in the main calorimeter indicates a deep inelastic scattering event with $Q^2 > 4$ GeV^2. For the "tagged" method an electron measurement in a dedicated detector, a so called tagger, is required[4]. In this case the geometry and acceptance of the tagger determines $Q^2 \sim 0$ GeV^2. In this analysis a tagger, 44 m downstream from the interaction point is used (see 2.2.3.1). This tagger is able to detect electrons with a certain energy. The angle of the electron can be calculated by the geometry of the tagger and the beam magnets. As shown in equation 4.6 a small scattering angle (θ_e) of the outgoing electron leads to $Q^2 \approx 0$ GeV^2.

$$Q^2_{el} = 2E_e E_e^{'}(1 + \cos\theta_e) \tag{4.6}$$

The angle of the outgoing electron is measured with respect to the proton direction (see 2.2). E_e is the energy of the electron beam and E_e' the energy of the scattered electron.

[4]The requirement not to have the scattered electron in the calorimeter is also referred to as "negative electron tag". An identified electron in the main detector or one of the subdetectors is also called a "positive electron tag". In this case "positive" or "negative" does not mean the charge of the lepton.

The 44 m tagger just provides the information whether an electron was detected or not. This is not sufficient to calculate the event kinematics. The event kinematics can be calculated by the method of "Jacquet - Blondel" [JB79], which uses the information from the hadronic system and does not require information about the scattered electron. y and W can be approximated by

$$y_{JB} = \frac{\sum_h E - p_z}{2E_e} \tag{4.7}$$

With $\sum_h E - p_z$ being the sum of $E - p_z$ over all hadrons.

$$W_{JB} = \sqrt{y_{JB}\ s} \tag{4.8}$$

and s being the square of the energy in the center of mass system. This method is insensitive to particles leaving the detector undetected in the forward direction because for particles in the forward direction ($\sum E - p_z$) is small. Particles in the backward direction contribute more to this sum. Therefore particles escaping undetected in the backward direction lower the measured W_{JB}.

Because the electron was found in the 44 m tagger, all energy deposits in the calorimeter are assumed to belong to the hadronic system. For each cell in the calorimeter the value $E - p_z$ is calculated. To calculate the z-component of the momentum the position of the cell center relative to the vertex is used. Each cell is calculated separately.

In most cases a shower originating from a single particle is spread across several calorimeter cells. Therefore cells which are close together could originate from the same particle and are combined to clusters. In ZEUS two different algorithms have been used to combine cells to clusters. The "condensates" algorithm considers just those cells which are in the same calorimeter (RCAL, BCAL, FCAL) and connects them with each other along their sides. The "islands" algorithm is able to build clusters which cover different calorimeters. This algorithm also considers cells connected at their edges belonging to the same cluster. The value $E - p_z$ is calculated for every cluster (condensate / island). The position of the cluster is calculated from the positions of the cells which belong to the cluster. The weight of each cell is given by the energy deposit in the cell.

Due to the dead material between the CTD and the calorimeter some particles seen in the CTD are not detected in the calorimeter. Moreover the angular resolution of the CTD for charged particles is better than the one of the calorimeter, for low energy particles the momentum measurement of the CTD is better than the energy measurement of the calorimeter. This can be exploited to improve the calorimeter measurement of the hadronic system. A matching algorithm finds pairs of tracks and calorimeter clusters. For each of those pairs the best measured values are taken. These pairs are called ZUFO's [Bri98]. Unpaired tracks and calorimeter clusters are added to this list. Based upon this pairs W_{JB} is calculated in this analysis.

Chapter 5

Analysis

5.1 Data Sample

For this analysis data taken with the ZEUS detector in the years 1996 and 1997 have been used. The integrated luminosity for this analysis is 16.6 pb^{-1} and is known within an error of $\pm 1.1\%$. The luminosity has been measured by a detector placed 107 m downstream from the interaction point [PZ95] using the process $ep \to ep\gamma$.

5.2 Event Selection

5.2.1 Trigger Selection

All events selected for this analysis have to pass a three level trigger system. Each event must fulfill at least one positive trigger decision on each trigger level. This means that at least one of the 50 - 250 boolean variables per trigger level is "true". These boolean variables are also called "trigger bits". A trigger bit is "true", if the event fulfills certain physics criteria[1]. In addition a trigger bit can require one or more trigger bits from the previous level to be set. A combination of trigger bits which requires at least one positive trigger decision on each level is called a "trigger chain".

The trigger decision can also be simulated for Monte Carlo events. For each simulated event the trigger response on every level is calculated independently from the decision on the previous trigger level. To treat real and simulated events in a comparable way it is necessary to apply the trigger chain requirement for both types of events.

For this analysis a chain was chosen with exactly one trigger requirement on each level. The chain requires an electron in the 44 m tagger and a track combination which is assumed to originate from a D^* meson.

[1]The physics criteria are in most cases based upon the energy deposit in the calorimeter or the activity found in the tracking device.

FLT The first level trigger requires some activity in the tracking system and an electron detected in the 44 meter tagger. The tracking at this level has a limited accuracy. It just takes into account the hits in the coaxial superlayers of the CTD. The spacial resolution is reduced to a superlayer in an octant.

SLT The requirements on the second level include the FLT bit described above. Compared to the tracks used in the offline analysis the tracks are still measured less precisely[2]. Therefore relatively loose criteria for $p_\perp(K)$, $p_\perp(\pi)$ and $p_\perp(D^0)$ are used. The cuts are chosen in a way which allows more than 60% of the D* events which can be reconstructed in the offline reconstruction, to pass this level.

TLT At this level the reconstructed tracks are close to the final ones. Based upon this tracks a complete D* reconstruction is performed. At least one track combination has to fulfill the ΔM, $M(D^0)$ and $p_\perp(D^*)$ requirements. Due to the remaining differences of the TLT tracks compared to those used in the offline analysis, the cuts applied on this level are less rigid than those used in the offline analysis.

5.2.2 Offline Selection

The ZES tool (see Section 2.3) is used to preselect the events. ZES allows to select events for an analysis, based on the value of approx. 200 numerical variables. In this analysis two ZES variables are used, the reconstructed transverse momentum $p_\perp(D^*)$ and the pseudorapidity $|\eta(D^*)|$ of the D* meson. The pseudorapidity is defined by

$$\eta = -\ln\tan\frac{\theta}{2} \tag{5.1}$$

where θ is the azimuth of the particle in question. $p_\perp(D^*)$ and $|\eta(D^*)|$ are calculated for every track combination which fulfill the same relaxed requirements as used in the third level trigger but they are calculated based upon the more precise track information available at offline level. The largest $p_\perp(D^*)$ and the smallest $|\eta(D^*)|$ found in all track combinations of an event are stored in the ZES database.

To select an event there has to be at least one candidate with $p_\perp(D^*) > 1.7$ GeV and another (or the same) with $|\eta(D^*)| < 1.7$. These cuts are relaxed with respect to the cuts used in this analysis. The relaxed cuts allow to study systematic effects of the $p_\perp(D^*)$ and $|\eta(D^*)|$ cuts used in this analysis.

5.2.3 Photoproduction Selection

This analysis is restricted to photoproduction events which are selected by a signal in the electron tagger (see section 4.3). Only events produced within a certain kinematic region are

[2] The maximum accuracy is limited by the input rate, the maximal output rate and the computing power of the second level trigger.

accepted in the electron tagger. The accessible kinematic region is given by the geometry, position and acceptance of the tagger. Due to the position of the tagger relative to the magnetic field of the beam magnets and the size and form of the active area only scattered electrons with $E'_e > 22$ GeV can be measured in this tagger (see Fig. 5.1). The procedure to obtain the acceptance of the electron tagger is explained in section 5.3.1 and in detail in [Kli].

According to formula 5.2 the limited acceptance of the scattered electron in E'_e and θ_e

$$W = \sqrt{s \ \ (1 - E'_e \frac{1 - \cos\theta_e}{2E_e})} \quad \text{for} \quad Q^2 \approx 0 \ \ \text{GeV}^2 \tag{5.2}$$

results in an accessible W region of 80 GeV $< W <$ 120 GeV. As shown in Fig. 5.10 this region has an acceptance above 20%. For every event W is measured by the Jacquet-Blondel method using the hadronic final state objects (see 4.3).

Monte Carlo studies show (see Fig. 5.2 and Fig. 5.3) a small deviation in the reconstruction of W. Fig. 5.2 shows the correlation between the reconstructed W and the generated W_{true}. The straight line indicates the W region used in this analysis. At the lower W limit of the 44m electron (80 GeV) tagger the reconstructed W is in reasonable agreement with the generated W (W_{true}). At the upper W limit (120 GeV) the reconstructed W is slightly smaller than the generated one. To compensate this deviation different W regions were chosen for the generated and the reconstructed events. For the generated W the region 80 GeV $< W_{true} <$ 120 GeV was chosen. The W region for the reconstructed value is slightly smaller 80 GeV $< W <$ 116.5 GeV. These regions are marked with a line in Fig. 5.2.

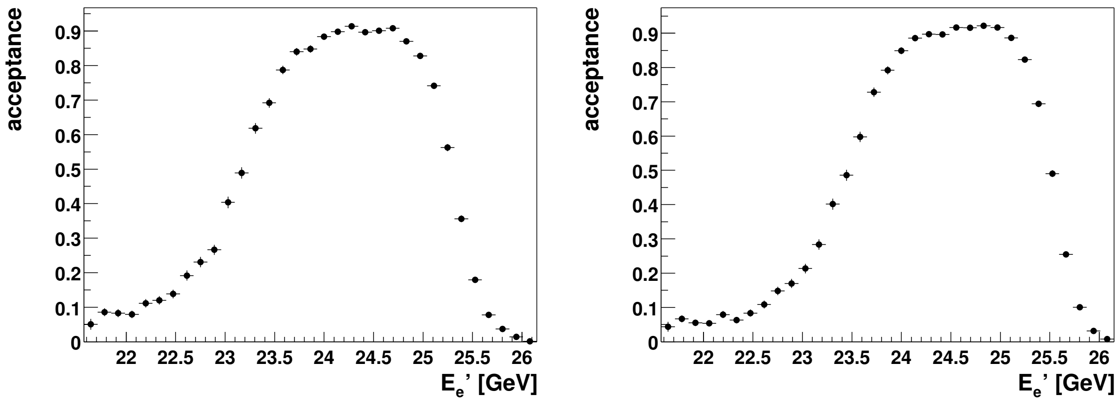

Figure 5.1: Acceptance of the electron tagger as function of the electron energy. The left plot shows the acceptance for 1996 and the right one for 1997.

5.2.4 D* Meson Selection

For the D* meson reconstruction only those events are used which fulfill the following quality requirements. Each track should cross at least the three innermost superlayers of the CTD,

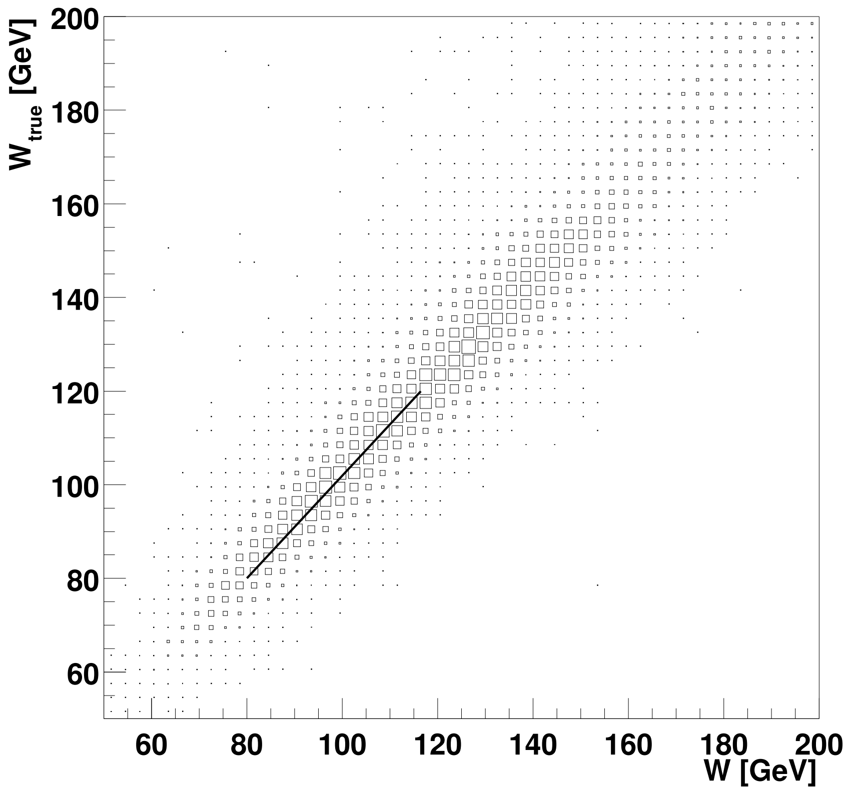

Figure 5.2: W_{true} vs. W. The solid line indicates the region used in this analysis. The size of each box is proportional to the number of events in the bin.

to have a reliable track reconstruction. Therefore a certain angle or pseudorapidity $\eta = \ln \tan \theta/2$ is required for every track.

- $|\eta_{track}| < 1.75$

Due to the short lifetime of the D* - meson and D^0 - meson the vertices produced by the decay of these mesons, are close to the primary vertex. The resolution of the tracking system is not sufficient to reconstruct the D* - meson and D^0 - meson vertices separately from the primary vertex. Therefore only tracks from the reconstructed primary vertex are accepted.

The main vertex has to be situated close to the nominal interaction point. The z-component is required to be within ± 40 cm of the nominal position.

Every track has to have a transverse momentum $p_\perp > 0.125$ GeV to ensure a reliable measurement of the track parameters in the CTD. The momentum of the K - mesons and the π - mesons from the D^0 decay are predominantly above 1 GeV. Fig. 5.4 and 5.5 show the transverse momentum and pseudorapidity distribution of the selected tracks. Low $p_\perp(K)$ and $p_\perp(\pi)$ requirements lead to a bad signal/noise ratio. A requirement of $p_\perp > 0.45$ GeV for the mesons from the D^0 decay leads to a good signal / noise ratio with an acceptable reduction in the number of events.

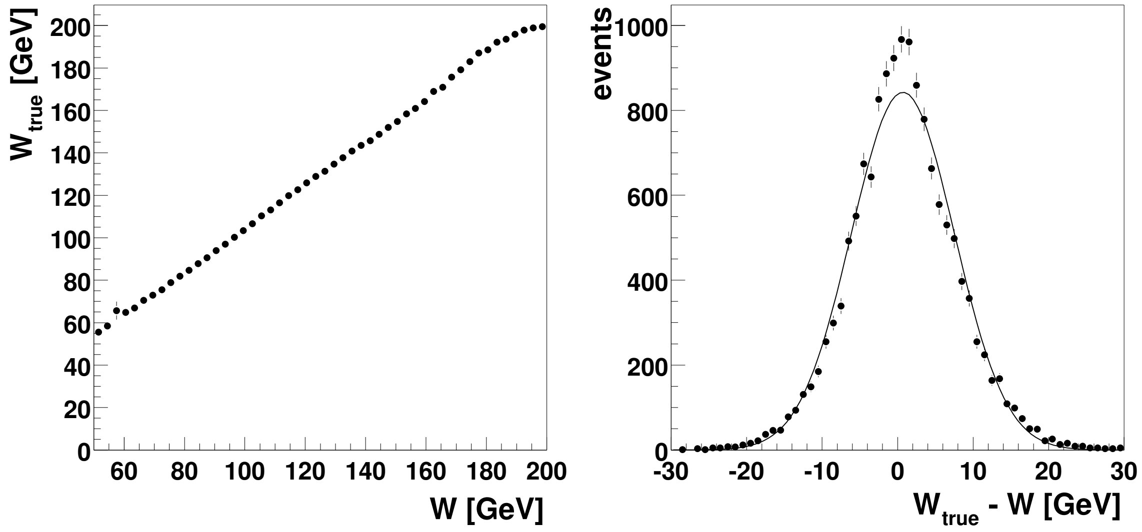

Figure 5.3: $W_{generated}$ vs. $W_{measured}$. The left plot is the mean value of Fig. 5.2. For each W the point indicates the mean W_{true}. The right plot shows the difference between the generated W_{true} and the reconstructed W. For this plots 80 GeV $< W <$ 116.5 GeV and 80 GeV $< W_{true} <$ 120 GeV is required. The reconstructed W is corrected according to the different W_{true} and W regions.

Compared to $p_\perp(K)$ and $p_\perp(\pi)$, $p_\perp(\pi_s)$ is small (see Fig. 5.6). For the π_s - meson $p_\perp(\pi_s) >$ 0.125 GeV is chosen.

- $p_\perp(K) > 0.45$ GeV
- $p_\perp(\pi) > 0.45$ GeV
- $p_\perp(\pi_{slow}) > 0.125$ GeV

The D* meson and the D^0 meson decay are two body decays. In the D* / D^0 rest frame the decay products are therefore produced back to back. However in the observed events the D* meson and therefore also the D^0 meson are not at rest. They are boosted in the direction of the charm quark. This boost also affects all decay products. In general the decay products are observed in the direction of the charm quark. By limiting η and $p_\perp$ for each track $\eta(D^*)$ and $p_\perp(D^*)$ are implicitly limited too. The cuts for $\eta(D^*)$ and $p_\perp(D^*)$ are chosen in a way which assures that the D* meson acceptance is not significantly affected by the track cuts.

- -1.0 $< \eta(D^*) <$ 1.5
- $p_\perp(D^*) > 2.0$ GeV

From the events fulfilling the given quality requirements the D* -mesons are selected. Their reconstructed ΔM and M_{D^0} have to be in a 3σ range around the peak value. This range is defined by:

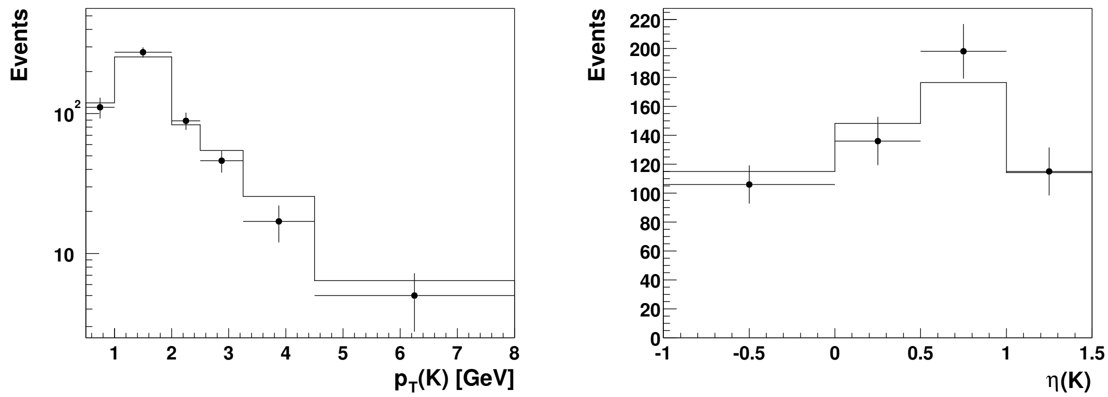

Figure 5.4: Comparison of the reconstructed $p_\perp(K)$ and $\eta(K)$ for measured data (points) and Monte Carlo (histogram). The Monte Carlo is area normalized to the measured data. $p_\perp(K)$ is shown in the left and $\eta(K)$ in the right plot.

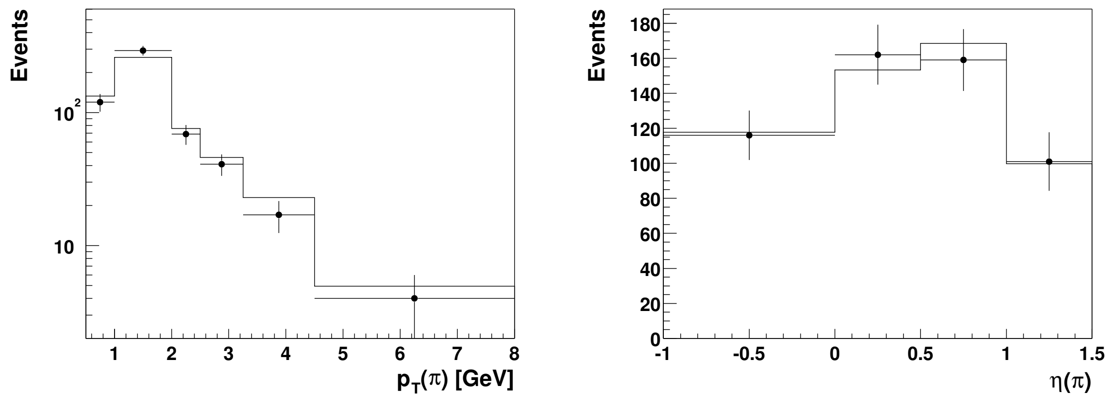

Figure 5.5: Comparison of the reconstructed $p_\perp(\pi)$ and $\eta(\pi)$ for measured data (points) and Monte Carlo (histogram). The Monte Carlo is area normalized to the measured data. $p_\perp(\pi)$ is shown in the left and $\eta(\pi)$ in the right plot.

- 0.143 GeV $< \Delta M <$ 0.148 GeV
- 1.8 GeV $< M(D^0) <$ 1.92 GeV

The ΔM and $M(D^0)$ distributions are shown in Fig. 5.8 and 5.9. The selected signal region is indicated. In the ΔM distribution one can see a prominent peak over a relatively flat background. This background is estimated by the "wrong charge combination" method (see section 4.2.1.1). In the $M(D^0)$ distribution the peak is less prominent. Also the background is not described as well as in the ΔM distribution. For $M_{D^0} < 1.7$ GeV the "wrong charge combination" method does not describe the background. This so called "satellite peak" is mainly produced by $D^* \to K\pi\pi\pi^0$ mode events (see section 4.2).

The number of events with a D* decay is obtained by subtracting the number of candidates with wrong charge combinations from the number of candidates with right charge

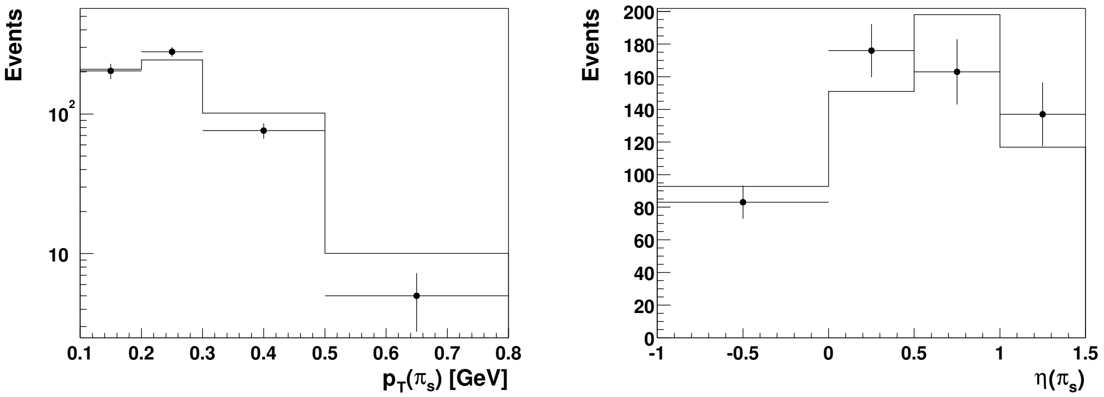

Figure 5.6: Comparison of the reconstructed $p_\perp(\pi_s)$ and $\eta(\pi_s)$ for measured data (points) and Monte Carlo (histogram). The Monte Carlo is area normalized to the measured data. $p_\perp(\pi_s)$ is shown in the left and $\eta(\pi_s)$ in the right plot.

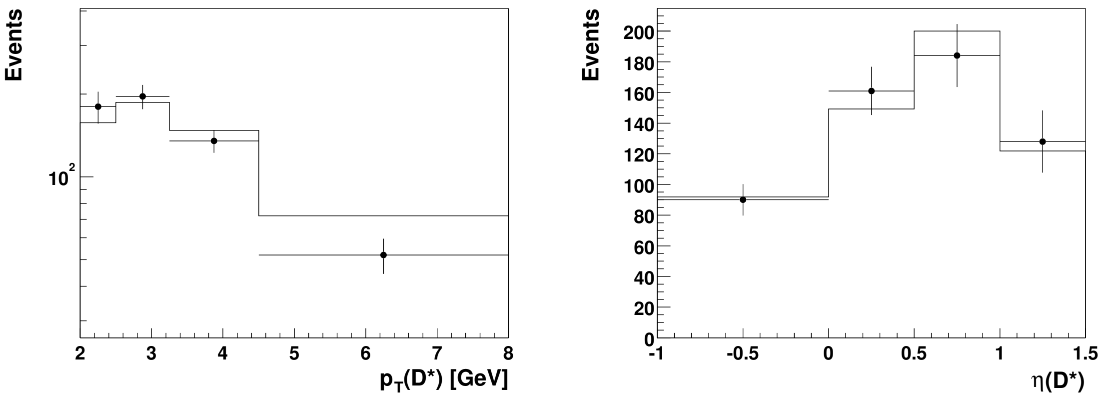

Figure 5.7: Comparison of $p_\perp(D^*)$ and $\eta(D^*)$ for Data (points) and Monte Carlo (histogram). $p_\perp(D^*)$ is shown in the left and $\eta(D^*)$ in the right plot.

combinations.

5.3 Acceptance

Due to the detector geometry and efficency not all events containing a D* decay can be reconstructed in the detector. To calculate cross sections the total number of events containing a D* is has to be determined. This number is achieved by scaling the measured number of events with a D* with the acceptance $\mathcal{A}$.

$$\mathcal{A} = \frac{\text{number of reconstructed events}}{\text{number of generated events}} \tag{5.3}$$

In general the acceptance is calculated by comparing the number of events generated in a

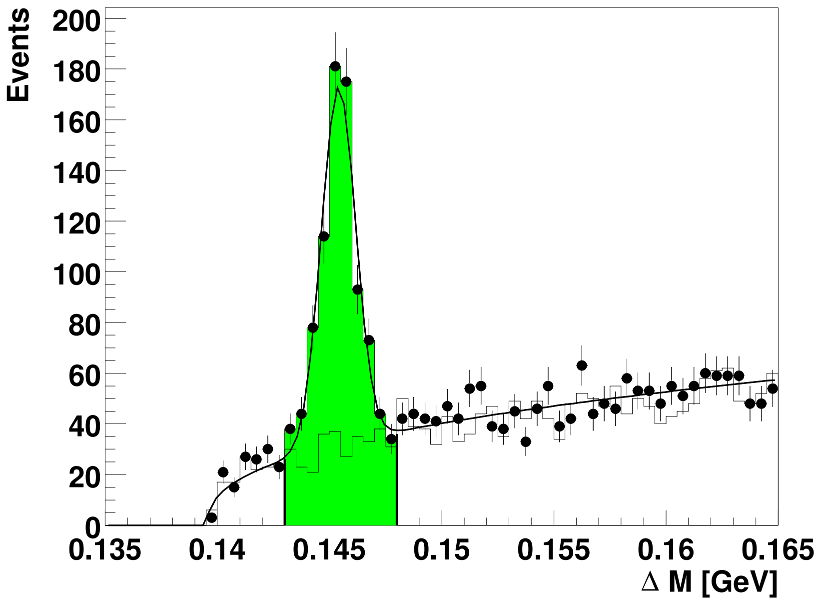

Figure 5.8: ΔM distribution for events with an electron in the 44m electron tagger. The points show the distribution for candidates with the right charge combination and the histogram shows the wrong charge combination background. The solid line shows the fit. The hatched area indicates the selected signal region defined by: 0.143 GeV $< \Delta M <$ 0.148 GeV.

certain kinematic range with the number of events which can be reconstructed from this sample. In this analysis the main contributions to the total acceptance are the D* - meson acceptance and the 44m electron tagger acceptance. Both acceptances are independent from each other. The acceptance of the D* decay depends on the geometrical acceptance and the track reconstruction efficency in the central tracking detector and the acceptance of the 44m electron tagger depends on the kinematic parameters of the scattered electron. They are calculated separately. The D* - meson acceptance is calculated by a Monte Carlo simulation as a function of $\eta(D^*)$ and $p_\perp(D^*)$. The 44m tagger acceptance is calculated as a function of W. Each real event is scaled by the inverse of the product of the two different acceptances. The appropriate acceptances are chosen according to the measured $\eta(D^*)$, $p_\perp(D^*)$ and W values.

5.3.1 44m Tagger Acceptance

The acceptance of the 44m tagger can not be determined with the general detector simulation program. It is calculated in a separate process based on the geometry of the beampipe and the beam magnets. The main input parameter for this calculation is the vertex distribution in the x-direction. From there on the electron trajectory is propagated through the beampipe according to the magnetic field generated by the beam magnets. The electron tagger is located in the x-z plane next to the beampipe. Therefore the y-vertex distribution does not

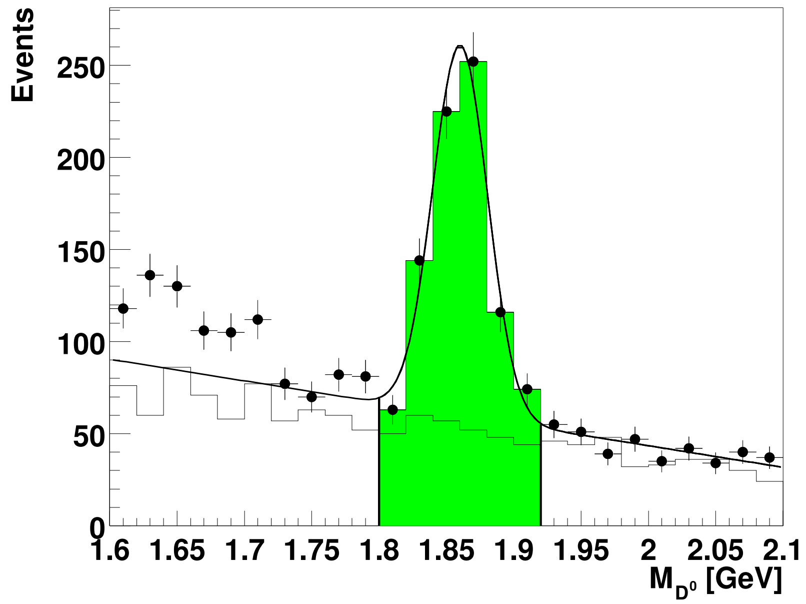

Figure 5.9: $M(D^0)$ distribution for events with an electron in the 44m electron tagger. The points show the distribution for candidates with the right charge combination and the histogram shows the wrong charge combination background. The solid line shows the fit. The fit was done for $M_{D^0} > 1.75$ GeV. The hatched area indicates the selected signal region defined by: 1.8 GeV $< M_{D^0} <$ 1.92 GeV.

affect the tagger acceptance and is neglected. Based upon this distribution, the acceptance of the 44m tagger is calculated in 52 W bins (see Fig. 5.10). The exact procedure can be found in [Kli].

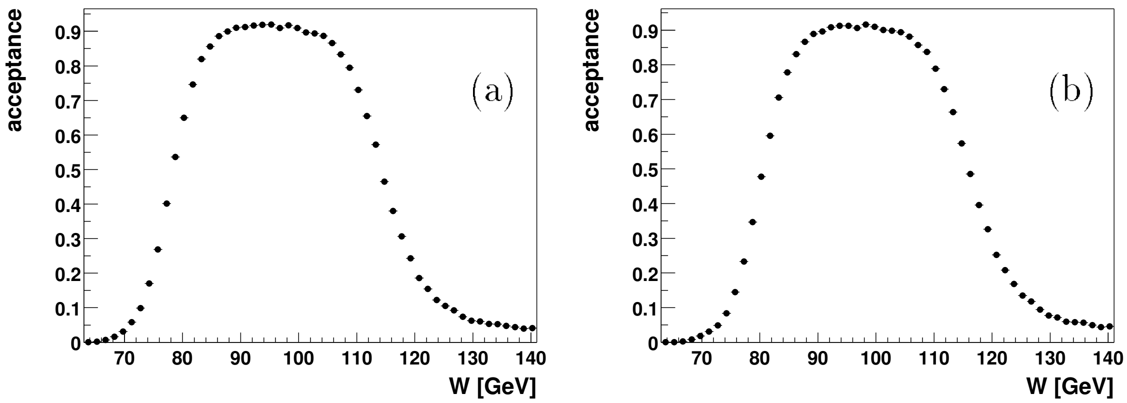

Figure 5.10: Acceptance of the electron tagger as function of W. The left plot shows the data form 1996 and the right one from 1997.

In this analysis the region 80 GeV $< W <$ 120 GeV is chosen. In this region the acceptance of the 44m electron tagger is understood and larger than 20%.

5.3.2 D* Meson Acceptance

As explained in section 5.2.4 this analysis is limited in $\eta(D^*)$ and $p_\perp(D^*)$. The acceptance is only calculated for this region. An extrapolation to the region not covered by the detector relies on the assumption that the $\eta(D^*)$ and $p_\perp(D^*)$ distributions are described correctly outside the geometrically inaccessibly region. Since the quality of the theory does not seem to allow such an extrapolation the geometrically inaccessible region is not considered in this analysis. For the calculation of the acceptance generated events with -1.0 $< \eta(D^*) <$ 1.5 and $p_\perp(D^*) > 2$ GeV are used. These are the same cuts as for the measured events.

The D* acceptance is estimated with events generated by a Monte Carlo simulation. As shown in Fig. 5.11 a large amount of generated events have a D*-meson within the chosen $\eta(D^*)$, $p_\perp(D^*)$ region, but at least one track from the D* meson / D^0 meson decay does not fulfill the requirements for η_{track} or $p_{\perp\, track}$. Therefore this decay is not reconstructed. Within the selected $\eta(D^*)$, $p_\perp(D^*)$ this effect dominates the D* meson acceptance.

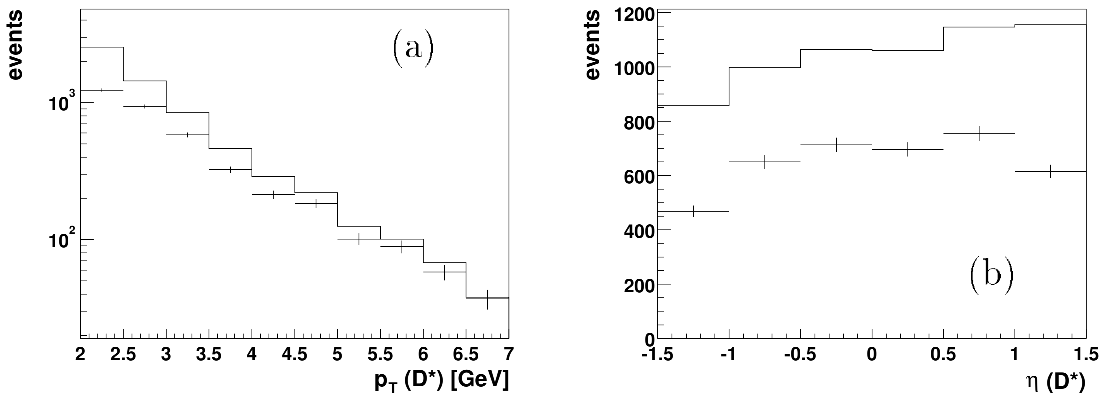

Figure 5.11: Generated $\eta(D^*)$ and $p_\perp(D^*)$. The histogram shows the number of generated events which fulfill the $\eta(D^*)$ and $p_\perp(D^*)$ requirements. The crosses show the number of events which fulfill the $\eta(D^*)$ and $p_\perp(D^*)$ requirements and the values generated for K, π and π_s fulfill the requirements applied to every single track. In this plot only generated quantities without detector simulation are shown.

The generated events are restricted to $Q^2 < 0.15$ GeV^2 since the generator is intended for this region.

In the selected region $\eta(D^*)$ and $p_\perp(D^*)$ are reconstructed without a systematic bias (see Fig. 5.12 and 5.13). This is also true for the three tracks from K, π and π_s (see Fig. 5.14, Fig. 5.15 and Fig. 5.16). Therefore no correction is applied to $\eta(D^*)$ and $p_\perp(D^*)$.

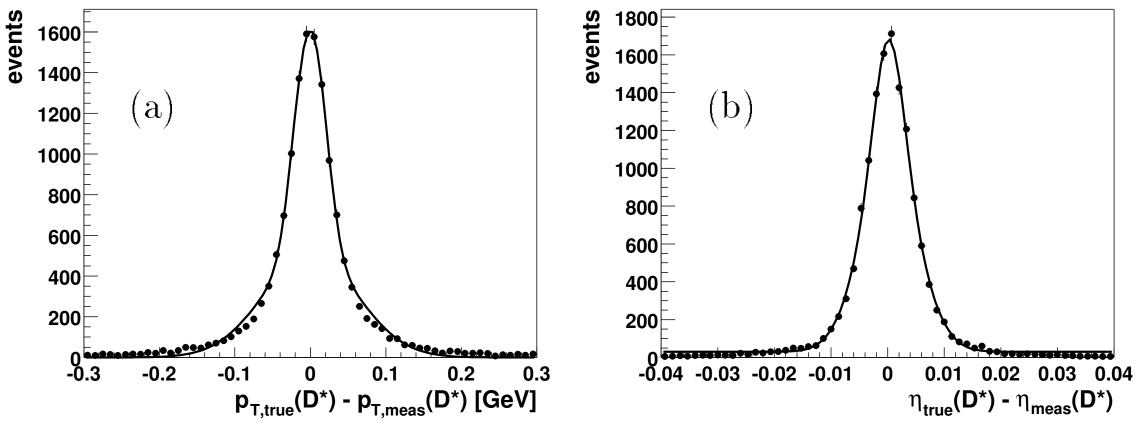

Figure 5.12: Difference between generated and Monte Carlo reconstructed $p_\perp(D^*)$ (left plot) and $\eta(D^*)$ (right plot).

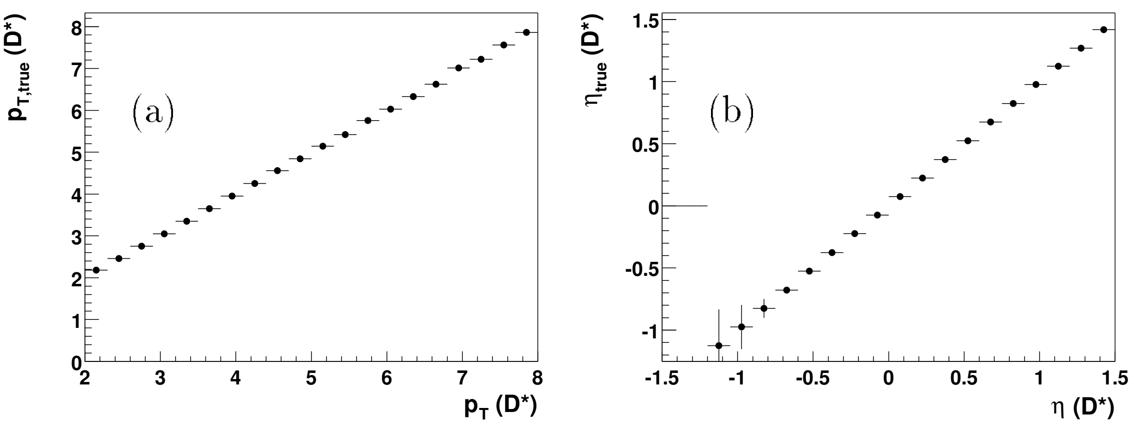

Figure 5.13: Relation between generated and Monte Carlo reconstructed $p_\perp(D^*)$ (left plot) and $\eta(D^*)$ (right plot). The relation is shown in a profile plot. The point in each $p_\perp$, η bin indicates the mean $p_{\perp,true}$, η_{true} value assuming a gaussian $p_{\perp,true}$, η_{true} distribution.

5.3.2.1 Grid Correction

The D* meson acceptance is not evenly distributed over the $\eta(D^*)$ and $p_\perp(D^*)$ range. A single acceptance for the whole range is highly dependent on the $\eta(D^*)$ and $p_\perp(D^*)$ predictions of the Monte Carlo and can therefore only be safely applied , if the measured $p_\perp(D^*)$ and $\eta(D^*)$ distributions are correctly described by the Monte Carlo. To reduce this dependence on the $p_\perp(D^*)$ and $\eta(D^*)$ distributions the D* reconstruction acceptance is measured separately for different bins in $\eta(D^*)$ and $p_\perp(D^*)$. The smaller the bins are the less model dependent is the acceptance. The size of the bins is limited by the $\eta(D^*)$ and $p_\perp(D^*)$ resolution and by the number of generated Monte Carlo events. A large number of bins requires a huge amount of

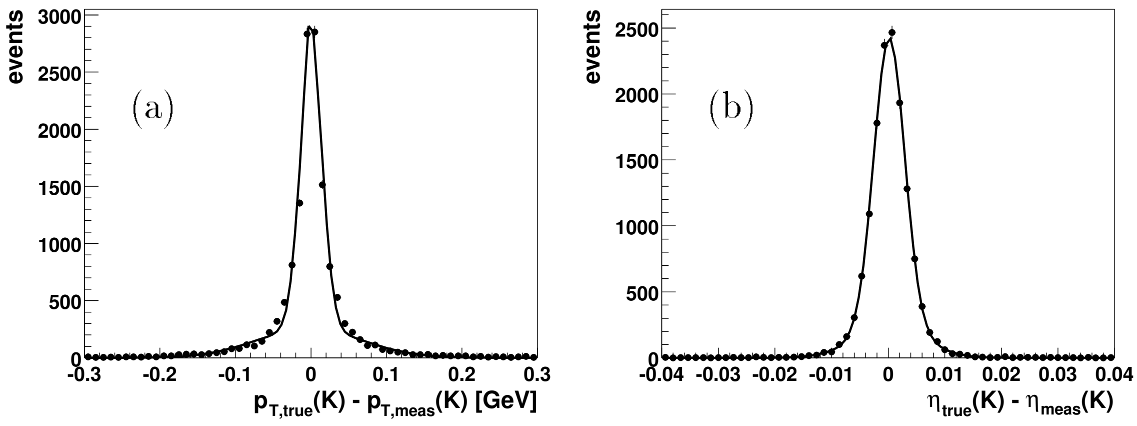

Figure 5.14: Difference between generated and Monte Carlo reconstructed $p_\perp(K)$ (left plot) and $\eta(K)$ (right plot).

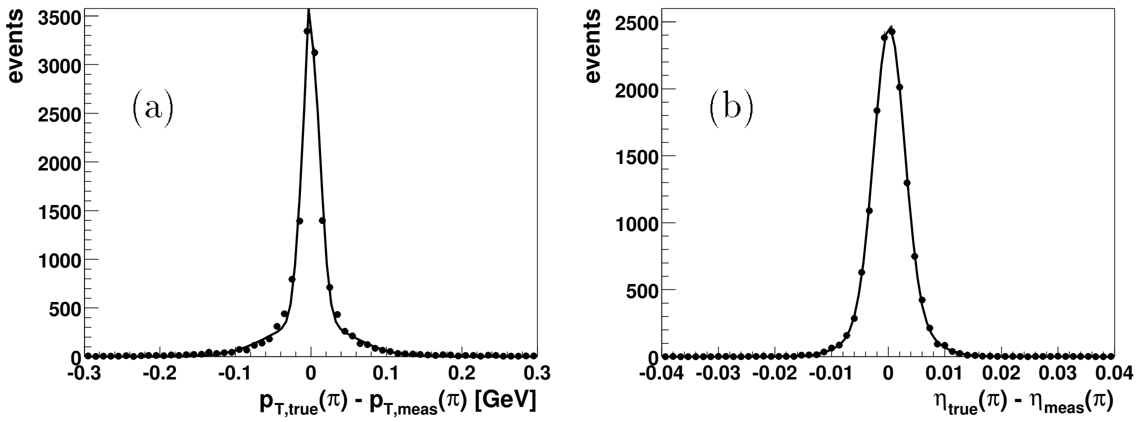

Figure 5.15: Difference between generated and Monte Carlo reconstructed $p_\perp(\pi)$ (left plot) and $\eta(\pi)$ (right plot).

simulated events to keep the statistical error small. In this analysis each variable is measured in four different bins which leads to 16 bins in total. The following $\eta(D^*)$ and $p_\perp(D^*)$ bins are used:

- $\eta(D^*)$ bin edges: -1.0 , 0.0 , 0.5 , 1.0 , 1.5
- $p_\perp(D^*)$ bin edges in GeV: 2.0 , 2.5 , 3.25 , 4.5 , 8.0

Each measured event is scaled with the inverse of the acceptance in the corresponding $\eta(D^*)$,$p_\perp(D^*)$ cell.

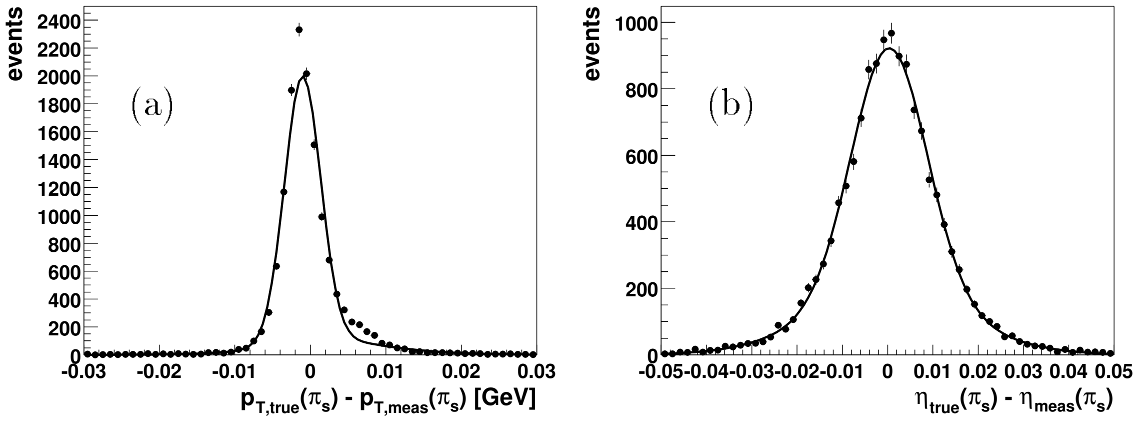

Figure 5.16: Difference between generated and Monte Carlo reconstructed $p_\perp(\pi_s)$ (left plot) and $\eta(\pi_s)$ (right plot). The scale for the x-axis is different compared to the D*, K and π.

5.4 Systematical Uncertainties

The following systematic checks where performed. The effect on the total cross section is given in brackets. If the value was shifted in both directions the first value refers to the shift in positive direction. Except for the last two cases the shift was applied to the measured data and the Monte Carlo based acceptance calculation.

- The ΔM signal region was shifted by ± 1 MeV (2.9% / -5.2%)
- The $M(D^0)$ signal region was shifted by ± 10 MeV (1.3% / 3.7%)
- The transverse momentum cut on the kaon was shifted by ± 50 MeV (-1.6%/-1.0%)
- The transverse momentum cut on the pion from the D^0 was shifted by ± 50 MeV (-0.3%/2.5%)
- The transverse momentum cut on the slow pion was shifted by ± 5 MeV (-0.3%/1.7%)
- The cut on the event vertex was removed (0.5%)
- The measured W region was shifted by $\pm$ 5 GeV (1.1%/-2.2%)
- The Pythia generator was used instead of Herwig (-5.8%)

The total systematical error is calculated by separately summing the negative and the positive contributions in quadrature.

The following systematical errors are not included in the calculation:

- The uncertainty of the luminosity measurement (1.4%)
- Uncertainties from the D* and D^0 branching ratios (0.5%) [PDG00]

5.4.1 Charge Asymmetry

Since a charm quark and a anti-charm quark are always produced together one would expect to have approximately the same number of D^{*+} and D^{*-} events in the sample used for this analysis. The difference is expected to depend on the acceptance and statistics. The acceptance (see Fig. 5.17) slightly favors D^{*+} above D^{*-}. This discrepancy in acceptance is based upon the different reconstructions qualities for positive and negative charged tracks (see 4.2.1.2.1). This behavior is seen as expected in the D^* untagged photoproduction analysis [ZEU99]. The untagged analysis is comparable to the tagged one presented here. The untagged analysis covers 130 GeV $< W <$ 250 GeV.

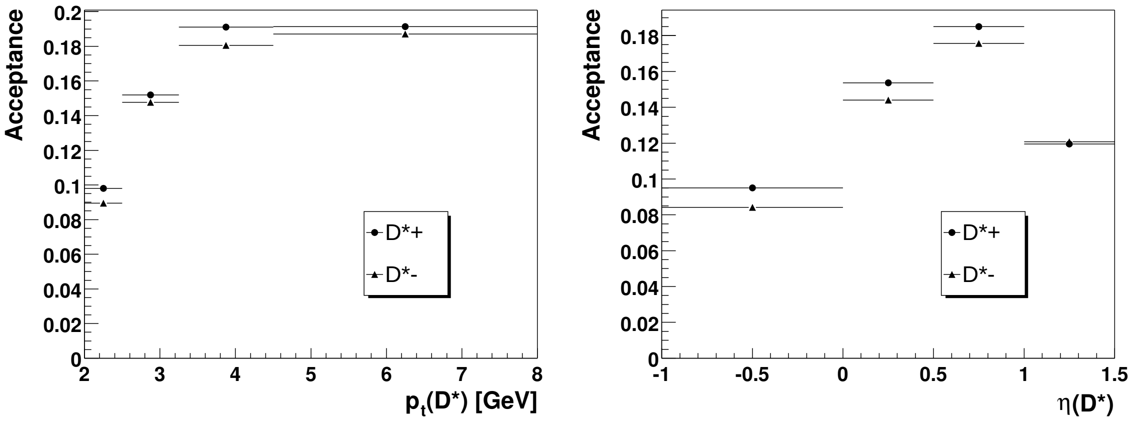

Figure 5.17: Acceptance for D^{*+} and D^{*+} as function of $\eta(D^*)$ and $p_\perp(D^*)$. The left plot shows $p_\perp(D^*)$ and the right one $\eta(D^*)$.

This expected asymmetry is not seen for the events used in this analysis. Instead one can see the opposite effect. In the years 1996 and 1997 more D^{*-} than D^{*+} are measured. This can be caused by the detector or the reconstruction process. It can also be a statistical fluctuation or a physical effect. To exclude a detector or reconstruction effect the trigger system and the track reconstruction was checked for an effect which favors negatively charged tracks or disfavors positively charged tracks.

The asymmetry between D^{*+} than D^{*-} is defined by

$$\mathcal{A} = \frac{\mathcal{N}D^{*+} - \mathcal{N}D^{*-}}{\mathcal{N}D^{*+} + \mathcal{N}D^{*-}} \tag{5.4}$$

with $\mathcal{N}D^{*+}$ and $\mathcal{N}D^{*-}$ being the number of D^{*+} and D^{*-} -mesons. Since the detector and the reconstruction was not changed one would expect to have the same asymmetry in all run periods if the effect is related to the detector or the reconstruction. Fig. 5.18 shows the asymmetry for the different run periods. The plot is based on the uncorrected number of D^* mesons. Due to the slightly better acceptance for D^{*+} the expected values for the asymmetry are above 0. The asymmetry which favors D^{*-} can just be found in the years 1996 and 1997. This leads to the assumption that the observed asymmetry in the tagged photoproduction D^* meson data is just a statistical fluctuation.

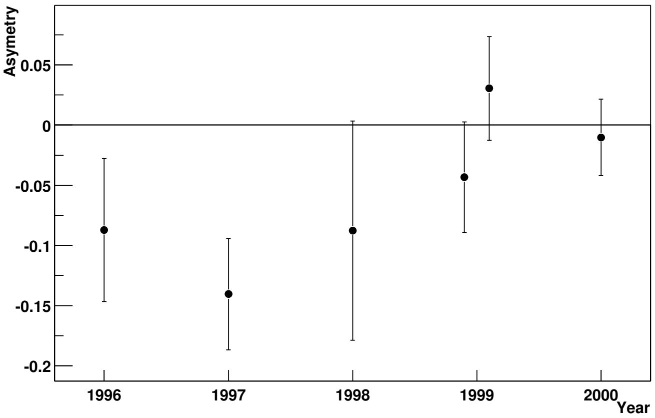

Figure 5.18: Charge asymmetry for photoproduction events tagged by the 44m tagger. Each point represents the asymmetry found in a certain time period. 1999 is represented by two points. The left one is measured with electrons, the right one with positrons. The errors shown are the statistical ones.

In addition the analysis was also performed for the so called "untagged" photoproduction. For this analysis a completely independent set of trigger bits was used. No identification of an electron in the 44m tagger was required. Instead the main calorimeter was searched for the scattered electron. The events were accepted if no electron was found. The asymmetry for this analysis is shown in Fig. 5.19. No relevant deviation from the expected value can be observed. Since the D* meson analysis based on tagged and untagged photoproduction have different $\eta(D^*)$ distributions (compare Fig. 6.1 and 6.8) the asymmetry is plotted for different $\eta(D^*)$ bins (see Fig. 5.20). Just the bin $-1 < \eta(D^*) < -0.5$ shows a small asymmetry which favors the detection of D^{*-} mesons. As shown in Fig. 6.2 the contribution of this bin to the total cross section is small. This plot is based on the events from the untagged photoproduction analysis in 1996/1997. Since no relevant asymmetry effect can be found in the untagged photoproduction analysis, neither for different years nor for different $\eta(D^*)$, one can conclude that the ZEUS tracking system and the applied selection criteria does not generate the asymmetry in the D* meson tagged photoproduction analysis.

In conclusion, no evidence for a systematical detector or reconstruction effect was found. The observed asymmetry for events with a D* and a tag from the 44m tagger is in reasonable agreement with the hypothesis of a statistical fluctuation.

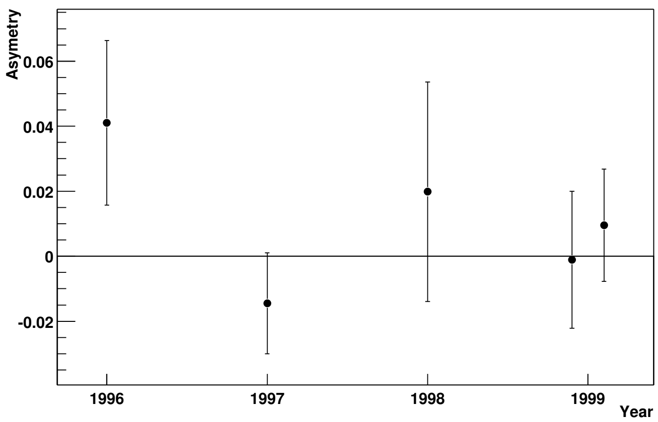

Figure 5.19: Charge asymmetry for events from untagged photoproduction. Each point represents the asymmetry found in a certain time period. 1999 is represented by two points. The left one is measured with electron, the right one with positrons. The scale is different to Fig. 5.18. The errors shown are the statistical ones.

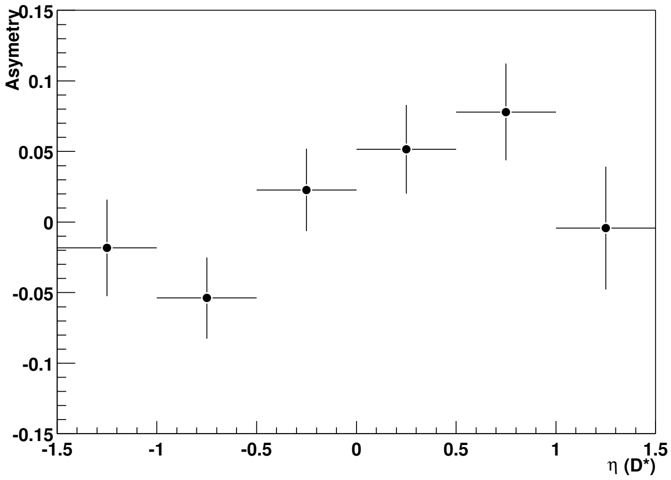

Figure 5.20: Charge asymmetry for untagged photoproduction events. Here the asymmetry is shown as a function of $\eta(D^*)$. The errors shown are the statistical ones.

Chapter 6

Results

6.1 Cross Section

6.1.1 Total Cross Section

The D* meson production cross section at $\sqrt{s} = 300$ GeV in the limited phase space 2 GeV $< p_\perp(D^*) < 8$ GeV, -1 $< \eta(D^*) < 1.5$, 80 GeV $< W < 120$ GeV and $Q^2 < 0.15$ GeV^2 can be calculated from the number of D* meson candidates measured in the phase space region by

$$\sigma_{ep\to eD^*X} = \frac{N_{D^*}}{\mathcal{E}_{D^*}\ \mathcal{E}_{t44}\ BR(D^{*\pm} \to K\pi\pi_s)\ \mathcal{L}} \tag{6.1}$$

where N_{D^*} is the number of D* candidates observed in the signal region after background subtraction. $\mathcal{E}_{D^*}$ is the D* meson reconstruction efficiency (see Sect. 5.3.2) and $\mathcal{E}_{t44}$ is the efficiency to find an electron in the 44m-tagger (see Sect. 5.3.1). The branching ratio of a D* meson decaying in the K$\pi\pi_s$ channel $BR(D^{*\pm} \to K\pi\pi_s) = 0.026 \pm 0.005$ is taken from [PDG00] (see Sect. 1.4). $\mathcal{L}$ is the integrated luminosity of the data set used for this analysis. This analysis is based upon the datasets from 1996 and 1997 with a combined luminosity of $\mathcal{L} = 16.6$ pb^{-1}. This leads to an integrated cross section in the selected phase space region

$$\sigma_{ep\to eD^*X} = 8.8 \pm 0.7(stat)^{+0.5}_{-1.0}(syst)\ \text{nb} \tag{6.2}$$

The phase space for this cross section is limited to 2 GeV $< p_\perp(D^*) < 8$ GeV, -1 $< \eta(D^*) <$ 1.5, 80 GeV $< W < 120$ GeV and $Q^2 < 0.15$ GeV^2. The same limits apply to the following differential cross sections if not stated otherwise.

6.1.2 Differential Cross Sections

The large available data sample also allows to measure the cross section differentially in $\eta(D^*)$ and $p_\perp(D^*)$. They are shown in Fig. 6.1 - 6.6. The inner error represents the statistical error and the outer the total error. The total error is the square root of the sum of the squares of the statistical and the systematical error. The horizontal bars indicate the width of the bin in which the cross was measured. The measured differential cross sections are compared to different massive (see Figs. 6.1, 6.2, 6.3 and 6.4) and massless QCD calculations (see Figs. 6.5 and 6.6)

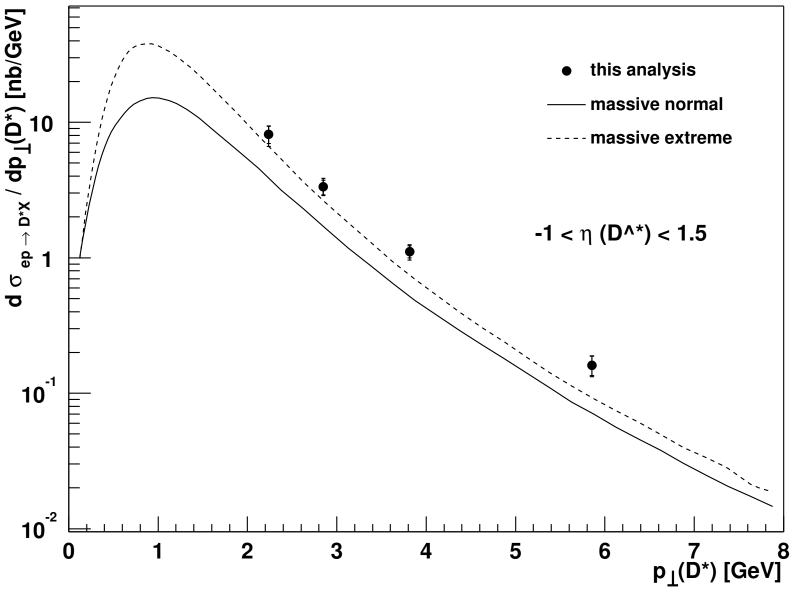

Figure 6.1: Differential cross sections $d\sigma/dp_\perp(D^*)$ for -1.0 $< \eta(D^*) <$ 1.5. The filled circles show the results of this analysis and the full line the predictions of a QCD calculation obtained by a program from Frixione et al. with the default parameters $\epsilon = 0.036$, $\mu_R = m_\perp$, $m_c = 1.5$ GeV. The dashed line represents the extreme settings $\epsilon = 0.036$, $\mu_R = 0.5 m_\perp$, $m_c = 1.2$ GeV.

The differential cross section $d\sigma_{ep\to D^*X}/dp_\perp(D^*)$ is shown in Fig. 6.1. The cross section for 2 GeV $< p_\perp(D^*) <$ 8 GeV spans nearly two orders of magnitude. The data points are positioned at the $p_\perp(D^*)$ value calculated by assuming an exponential drop of the cross section towards higher $p_\perp(D^*)$. The slope of the exponential is determined by a Monte Carlo calculation. This is justified since the slope of the $p_\perp(D^*)$ is reproduced by the Monte Carlo (see Fig. 5.7). The point at which the exponential function equals the integral over the bin in question divided by its width is taken as the center of the bin.

In addition to the measured data two QCD calculations are shown. The predictions are also drawn in the unmeasured region 0 GeV $< p_\perp(D^*) <$ 2 GeV. Both predictions are based upon a massive calculation. The calculation was performed by a program provided by Frixione et al. [MNR92] [FMNR94]. This program uses a massive NLO calculation and the Peterson fragmentation function [PSSZ83]. The continuous line represents the results of the calculation using the default parameters recommended by the authors: the Peterson parameter is set to $\epsilon = 0.036$, the renormalization scale is $\mu_R = m_\perp$ and the charm mass is set to $m_c = 1.5$ GeV. This set of parameters predicts cross sections which are almost a factor two lower than the measured ones. To check whether a better agreement can be found with

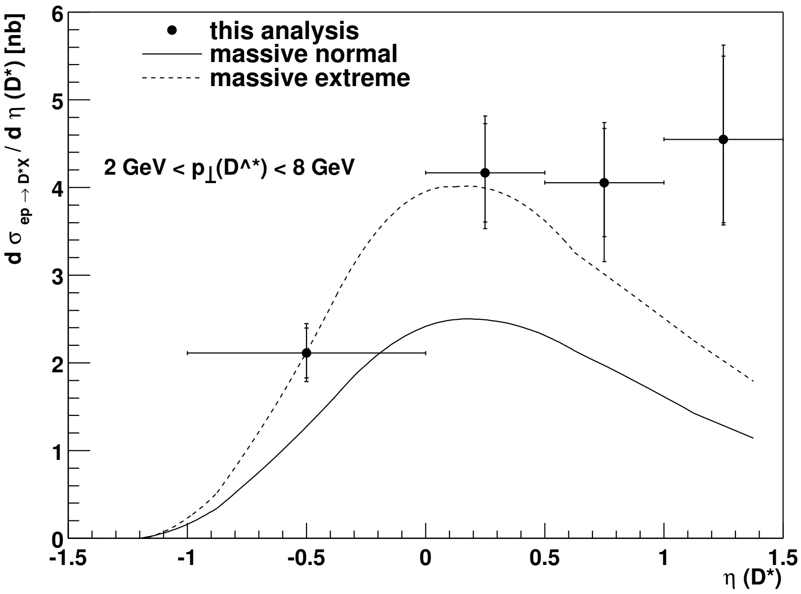

Figure 6.2: Differential cross sections $d\sigma/d\eta(D^*)$ for 2 GeV $< p_\perp(D^*) <$ 8 GeV. The filled circles show the results of this analysis and the full line the predictions of a QCD calculation obtained by a program from Frixione et al. with the default parameters $\epsilon = 0.036$, $\mu_R = m_\perp$, $m_c = 1.5$ GeV. The dashed line represents the extreme settings $\epsilon = 0.036$, $\mu_R = 0.5 m_\perp$, $m_c = 1.2$ GeV.

other parameter settings, the parameters are changed within the limits recommended by the authors. The renormalization scale is set to $\mu_R = \frac{1}{2} m_\perp$ and for the charm mass $m_c = 1.2$ GeV is used. This set of parameters leads to a higher cross section prediction which is shown as the dashed line. This prediction describes the data better, in particular at low $p_\perp(D^*)$, but is still too low for high $p_\perp(D^*)$. This behavior is expected, since the massive method is expected to be less reliable for $p_\perp \gg m_c$.

In Fig. 6.2 the differential cross section $d\sigma_{ep\to D^*X}/d\eta(D^*)$ is shown. As for the $d\sigma_{ep\to D^*X}/dp_\perp(D^*)$ cross section the same two massive calculations are plotted, also as a straight and a dashed line. Neither of them is in agreement with the data. The calculation based upon the normal settings is about a factor two below the data. The largest deviation can be observed in the forward direction. For negative $\eta(D^*)$ the calculation with extreme parameters describes the data, but in the forward direction it is significantly below the data. Compared to the calculation with the normal setting, the extreme set of parameters leads to an increase up 50% of the cross section in the forward region. The largest increase can be observed in the central region.

To further investigate the discrepancy between data and QCD calculations, the differential cross section $d\sigma_{ep\to D^*X}/d\eta(D^*)$ is plotted for two different $p_\perp(D^*)$ regions. Fig 6.3 is restricted to low $p_\perp(D^*)$: 2 GeV $< p_\perp(D^*) <$ 3.25 GeV and Fig 6.4 shows the high $p_\perp(D^*)$ region: 3.25 GeV $< p_\perp(D^*) <$ 8 GeV. A comparison of the calculations shows that the shape of the D* mesons cross section for high $p_\perp(D^*)$ is shifted towards the forward direction. As expected

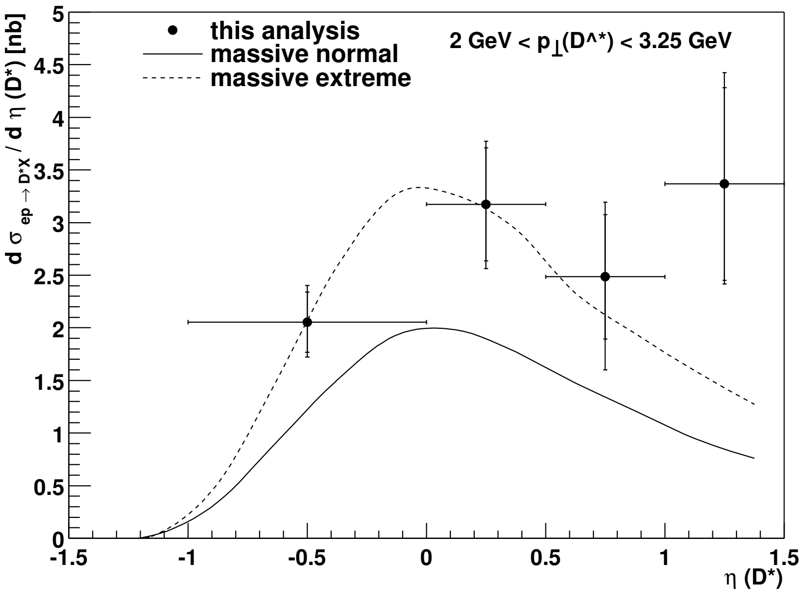

Figure 6.3: Differential cross sections $d\sigma/d\eta(D^*)$ for 2 GeV $< p_\perp(D^*) <$ 3.25 GeV. The filled circles show the results of this analysis and the full line the predictions of a QCD calculation obtained by a program from Frixione et al. with the default parameters $\epsilon = 0.036$, $\mu_R = m_\perp$, $m_c = 1.5$ GeV. The dashed line represents the extreme settings $\epsilon = 0.036$, $\mu_R = 0.5 m_\perp$, $m_c = 1.2$ GeV.

the massive calculation describes the data better for smaller $p_\perp(D^*)$. For higher $p_\perp(D^*)$ an excess of the data compared to the QCD calculations can be seen in the forward direction or for positive $\eta(D^*)$. All predictions are below the data. Due to the limited event sample the significance of this effect is not high, since none of the points is two standard deviations or more away from the model predictions.

In Fig. 6.5 the differential cross section $d\sigma_{ep\to D^*X}/dp_\perp(D^*)$ is compared to a massless calculation by Kniehl et al. [KKS97] [BKK98] [BKK97]. This calculation was performed with three different photon structure function parametrisations. The continuous line was calculated with GRV-G HO [GRV92], the dashed with GS-G-96 HO and the dotted with AFG-G HO [AGF93]. The charm quark fragmentation function used in this calculation is of the Peterson form with parameters obtained from e^+e^- data [BKK97]. This calculation gives a better description of the measured cross sections. Only at low $p_\perp(D^*)$ they are clearly above the data. The slope is steeper than the measured one. Since the massless calculation is expected to be not reliable for $p_\perp \sim m_c$, it is not shown for the unmeasured region 0 GeV $< p_\perp(D^*) <$ 2 GeV. Since for low $p_\perp(D^*)$ the authors have not made calculations, their predictions of $d\sigma_{ep\to D^*X}/d\eta(D^*)$ can only be compared in the high $p_\perp(D^*)$ region. Fig. 6.6 shows that the results of the calculation are sensitive to the photon structure function parametrisations used, in particular for $\eta(D^*) < 0.5$. But the differences are small compared to the errors of the measurement. As in the massive case the forward cross section predictions are lower than the measured data.

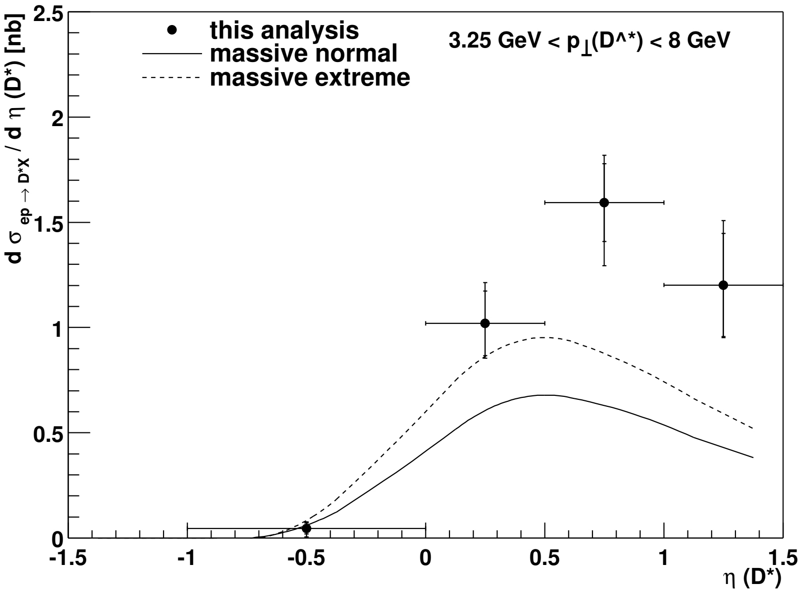

Figure 6.4: Differential cross sections $d\sigma/d\eta(D^*)$ for 3.25 GeV $< p_\perp(D^*) <$ 8 GeV. The filled circles show the results of this analysis and the full line the predictions of a QCD calculation obtained by a program from Frixione et al. with the default parameters $\epsilon = 0.036$, $\mu_R = m_\perp$, $m_c = 1.5$ GeV. The dashed line represents the extreme settings $\epsilon = 0.036$, $\mu_R = 0.5m_\perp$, $m_c = 1.2$ GeV.

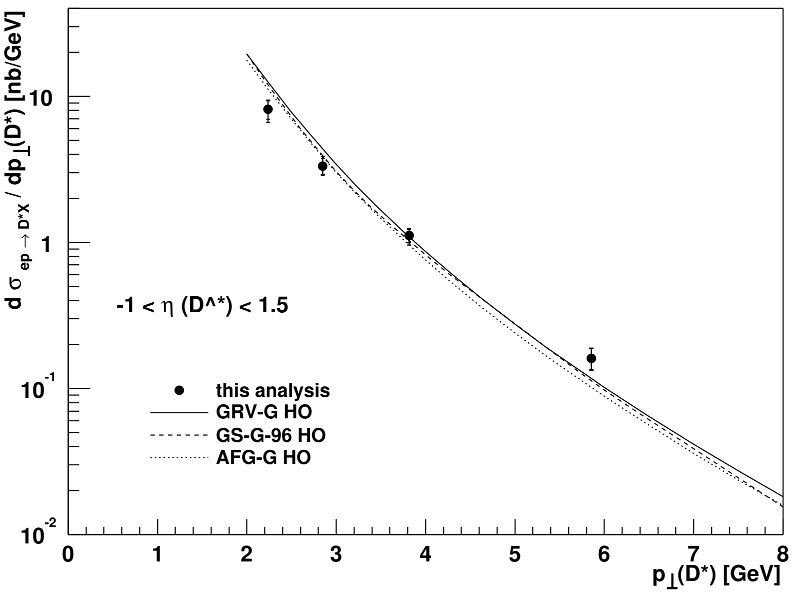

Figure 6.5: Differential cross sections $d\sigma/dp_\perp(D^*)$ for -1.0 $< \eta(D^*) <$ 1.5. The filled circles show the results of this analysis. The lines show the results of massless calculations with different photon structure functions.

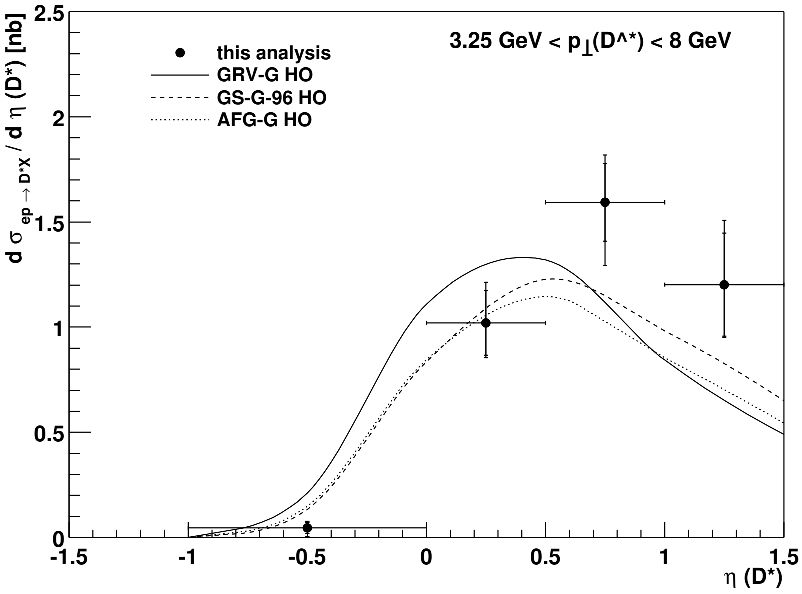

Figure 6.6: Differential cross sections $d\sigma/d\eta(D^*)$ for 3.25 GeV $< p_\perp(D^*) <$ 8 GeV. The filled circles show the results of this analysis. The lines show the results of massless calculations with different photon structure functions.

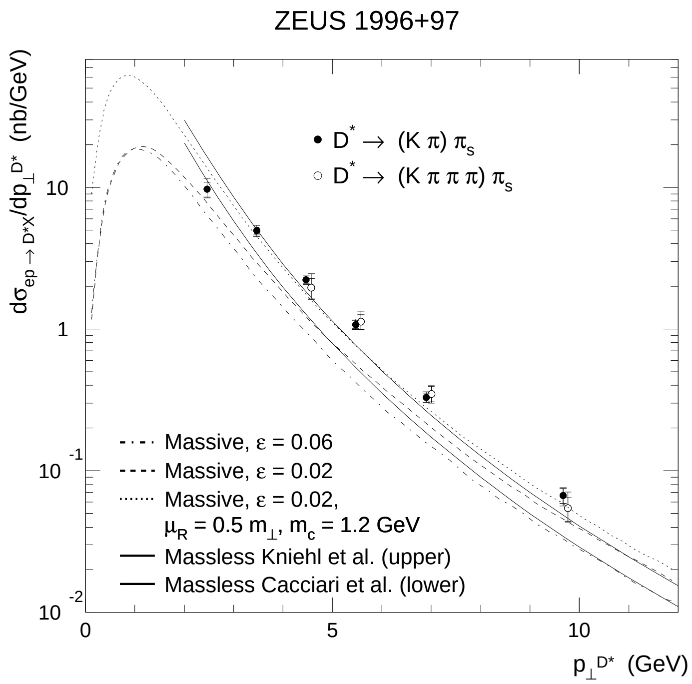

Figure 6.7: Differential cross sections $d\sigma/dp_\perp(D^*)$ for untagged photoproduction. (from [ZEU99])

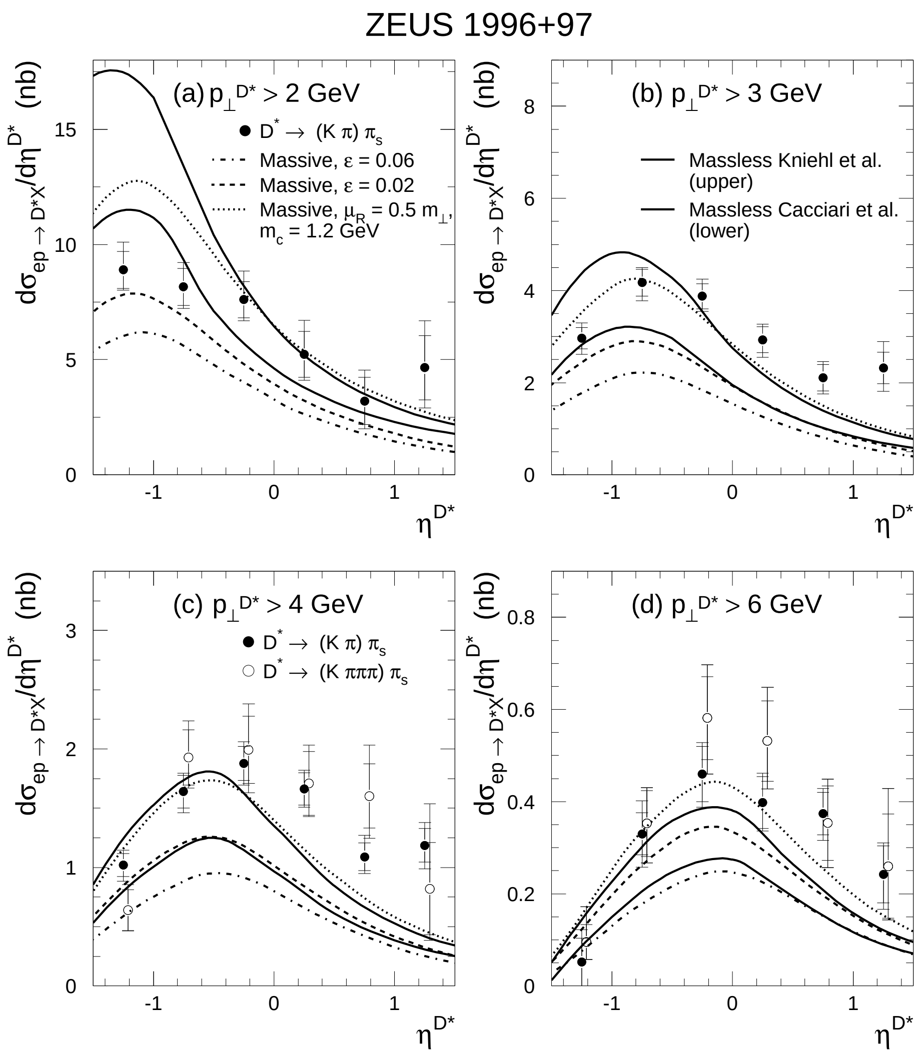

Figure 6.8: Differential cross sections $d\sigma/d\eta(D^*)$ for untagged photoproduction. (from [ZEU99])

In general the massless calculations describe the data better than the massive ones, especially for high $p_\perp(D^*)$. Both the massive and the massless calculation underestimate the forward cross section. This effect was also observed in the "untagged" analysis [ZEU99] [ZEU99a]. This analysis is similar to the one shown in this thesis but covers a different W region: 130 GeV $< W <$ 250 GeV. In this analysis no identification of the scattered electron is required. The selection of photoproduction events is done by rejecting all events where an electron was found in the main calorimeter (untagged photoproduction). The D* meson is identified by the decay products of the $D^{*\pm} \rightarrow (K^{\mp}\pi^{\pm})\pi_s^{\pm}$ channel. In addition the results from the analysis of the decay channel $D^{*\pm} \rightarrow (K^{\mp}\pi^{\pm}\pi^{\pm}\pi^{\mp})\pi_s^{\pm}$ are shown as open circles. In Fig 6.7 the differential cross section $d\sigma_{ep\rightarrow D^*X}/dp_\perp(D^*)$ for 130 GeV $< W <$ 250 GeV is shown. The cross sections are compared to different massive and massless calculations. The massive ones are based upon the same program as those used in Fig. 6.1 - Fig. 6.4. The cross section $d\sigma_{ep\rightarrow D^*X}/d\eta(D^*)$ of this analysis is shown in Fig. 6.8. The minimal $p_\perp(D^*)$ is given in each plot. For $p_\perp(D^*) > 3$ GeV, $p_\perp(D^*) > 4$ GeV and $p_\perp(D^*) > 6$ GeV all calculations underestimate the cross section in the forward direction. The same effect was also observed in deep inelastic scattering (DIS) D* meson production [ZEU00].

By comparing Fig. 6.8(a) to Fig. 6.2 or Fig. 6.8(b) to Fig. 6.4 which represent approximately the same $p_\perp(D^*)$ region the cross section is shifted to higher $\eta(D^*)$ for lower W as expected.

In the Peterson fragmentation (see Sect. 1.4.1) the production of a certain hadron with a certain momentum fraction just depends on the Peterson parameter ϵ. The direction of the charm quark is directly inherited by the charmed hadron. In [NS99] a refined fragmentation model is presented which takes into account the interaction between the proton remnant and the charmed hadron. This model shifts the charmed hadron to the forward direction. The effect has been called "beam-drag effect". Since both calculations, the massive and the massless one, use the Peterson fragmentation, this effect can explain why both calculations underestimate the cross section in the forward direction.

To evaluate this effect the Peterson fragmentation in the massive calculation was replaced by the fragmentation as it is implemented in the Pythia Monte Carlo Generator. This fragmentation takes into account interactions between the charmed hadron and the proton remnant and can therefore mimic the "beam-drag effect". The results are shown in Fig. 6.9. By this procedure the cross section is shifted in the forward direction.

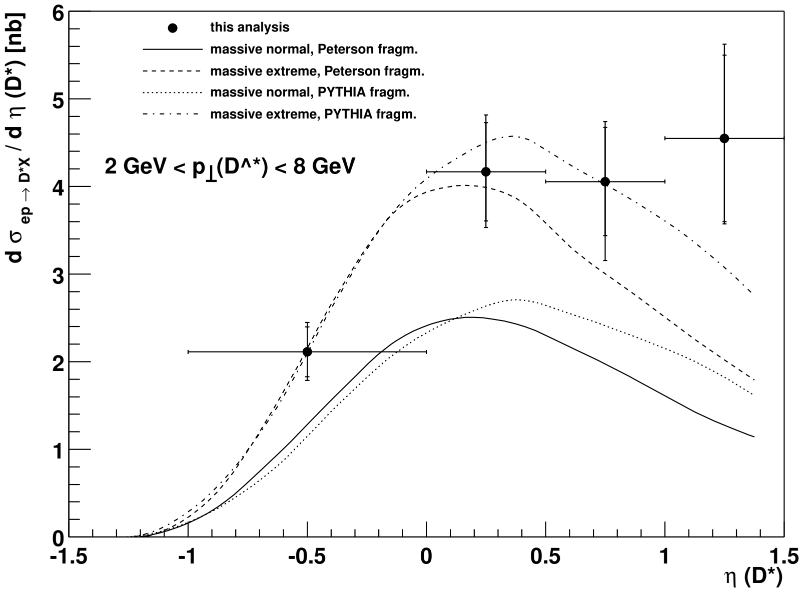

Figure 6.9: Differential cross sections $d\sigma/d\eta(D^*)$ for 2 GeV $< p_\perp(D^*) <$ 8 GeV. The filled circles show the results of this analysis. As in Fig. 6.2 the full and the dashed lines are calculated in the massive scheme with the normal and extreme settings. The dotted and the dash-dotted lines are also calculated with the normal and the extreme settings, but using fragmentation as obtained from Pythia.

In Fig. 6.10 the results of the massive and the massless calculations are compared to the data measured in this analysis. The 3.25 GeV $< p_\perp(D^*) <$ 8 GeV region is chosen, since it is the region for which results from both calculations are available. The massive calculation is

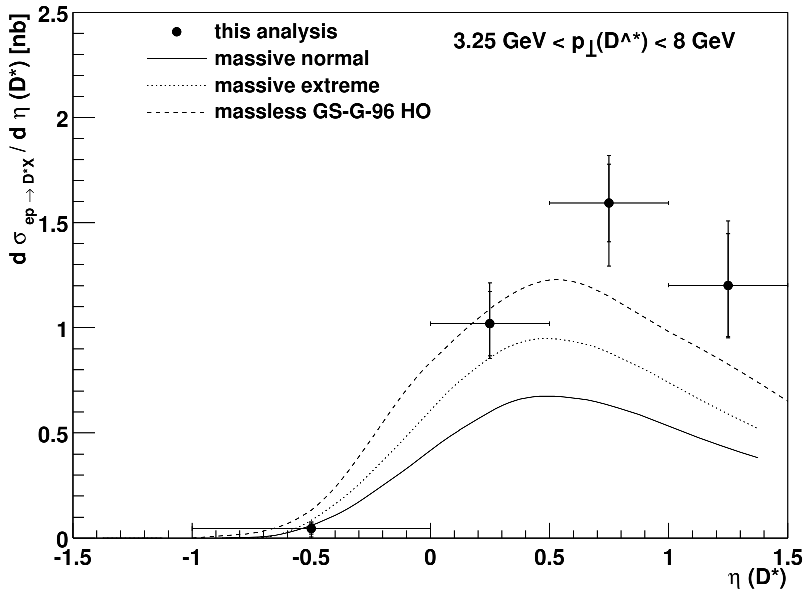

Figure 6.10: The results of the massive and the massless QCD calculations are compared to the measured cross sections in the region 3.25 GeV $< p_\perp <$ 8 GeV. For the massless calculation the photon structure function parametrisations GS-G-96 HO was used.

about a factor of two below the massless calculation. The massless one is in better agreement with the measured data, although the error of the data is large. Since the massive calculation is more reliable for $p_\perp \sim m_c$ and the massless one for $p_\perp \gg m_c$, the massless calculation is expected to describe the region 3.25 GeV $< p_\perp(D^*) <$ 8 GeV better, while the massive one should be more reliable at 2 GeV $< p_\perp(D^*) <$ 3.25 GeV.

A fair comparison of the theory to the data should therefore compare low $p_\perp(D^*)$ data with the massive calculation (see Fig. 6.3) and the high $p_\perp(D^*)$ data with the massless calculation (see Fig. 6.6). As one sees in Fig. 6.3 and Fig. 6.6 the two calculations approximately describe the data in their appropriate region of validity. However, even in their preferred region both calculations underestimate the cross section in the forward direction. Due to the large errors in the data and the uncertainties of the calculations it is not possible to draw firm conclusions.

Since the kinematic regions of the analysis presented in this thesis and the analysis at 130 GeV $< W <$ 280 GeV partly differ, a direct comaprison is not possible. Therefore only the ratios between the measured data and the results of the NLO QCD calculations are compared In Fig. 6.11 the measured cross section is divided by the results of the NLO QCD calculations in the appropriate W region. Fig. 6.11 (a) shows a comparison for the $p_\perp(D^*) >$ 2 GeV region. The 80 GeV $< W <$ 120 GeV analysis is in addition restricted to $p_\perp(D^*) <$ 8 GeV. For the low W analysis the results of the massive calculation with the normal and the extreme parameter settings are shown. For the high W case only the results of the calculation with the normal settings are available. In addition to the two massive calculations the results of the massless calculation are compared to the results of the measurement restricted to high $p_\perp(D^*)$ in Fig. 6.11(b). High $p_\perp(D^*)$ means 2 GeV $< p_\perp(D^*) <$ 8 GeV for the analysis with

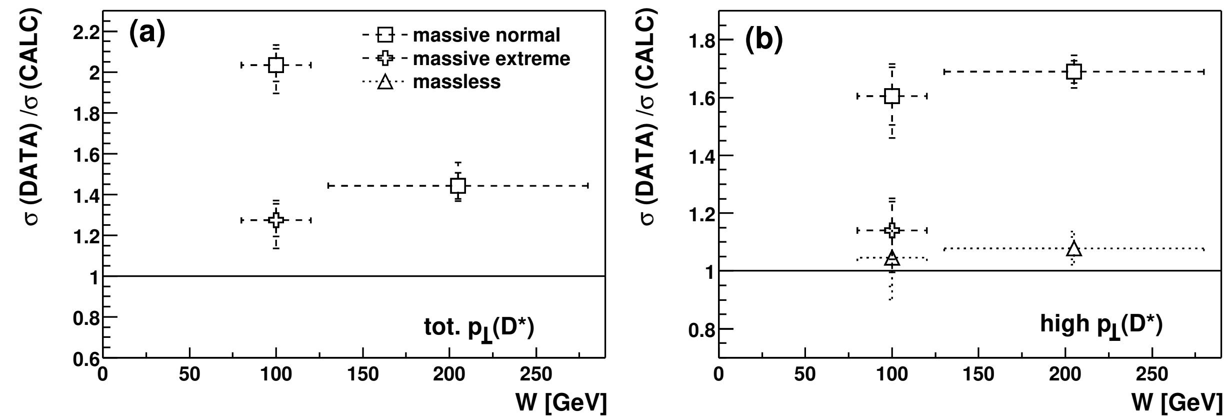

Figure 6.11: The measured cross sections are divided by the results of different calculations. Fig. (a) shows the ratios for the total $p_\perp(D^*)$ region: 2 GeV $< p_\perp(D^*) <$ 8 GeV for 80 GeV $< W <$ 120 GeV and $p_\perp(D^*) >$ 2 GeV for 130 GeV $< W <$ 280 GeV. Fig. (b) is restricted to the high $p_\perp(D^*)$ region: 3.25 GeV $< p_\perp(D^*) <$ 8 GeV for 80 GeV $< W <$ 120 GeV and $p_\perp(D^*) >$ 3 GeV for 130 GeV $< W <$ 280 GeV. The errors shown are the errors of the measurement projected to the calculations.

80 GeV $< W <$ 120 GeV and $p_\perp(D^*) >$ 2 GeV for the analysis with 130 GeV $< W <$ 280 GeV.

For the total $p_\perp(D^*)$ region the massive calculation with normal parameters shows a significant discrepancy between the low W and the high W region. The agreement of the calculation is better at high W. The W dependence of the cross section is not described by this calculation. The massive calculation with extreme parameter settings describes the data better than the calculation with normal settings in the low W region. For high $p_\perp(D^*)$ the massive calculation with normal parameters is about a factor of 1.7 away from the data, but it describes the W dependence of the cross section. The massive calculation with extreme parameters describe, within the errors, the data for low W. The massless calculation describes, within the errors, the data, including the W dependence of the cross section. The extension of the D^* cross section measurement towards low W provides therefore an additional consistency check for perturbative QCD.

Summary and Conclusions

An analysis of $D^{*\pm}$ meson photoproduction in electron proton scattering at HERA has been presented. The data taken with the ZEUS detector in the years 1996 and 1997 with an integrated luminosity of $\mathcal{L} = 16.6$ pb^{-1} has been analyzed.

The events for this analysis were preselected with a new tag database using an object oriented database management system (OODBMS). This tag database was developed in the course of this thesis and reduces the amount of computing power needed for a physics analysis by up to one order of magnitude.

Photoproduction events were selected by requiring an identification of the scattered electron in a tagger 44m away from the interaction point. By this requirement the invariant mass of the $\gamma - p$ system W is limited to 80 GeV $< W <$ 120 GeV and $Q^2 < 0.15$ GeV^2. The $D^{*\pm}$ photoproduction in this region has been measured for the first time. The $D^{*\pm}$ meson channel $D^{*\pm} \to K^{\mp}\pi^{\pm}\pi_s^{\pm}$ is used in this analysis to identify a $D^{*\pm}$ meson. Due to detector geometry and acceptance effects the kinematic region was limited in the pseudorapidity of the D^* meson to -1.0 $< \eta(D^*) <$ 1.5 and the transverse momentum of the D^* meson to 2.0 GeV $< p_\perp(D^*) <$ 8.0 GeV.

The total cross section for $\sqrt{s_{ep}} = 300$ GeV in the phase space limited in W, Q^2, $\eta(D^*)$ and $p_\perp(D^*)$ is measured to

$$\sigma_{ep\to eD^*X} = 8.8 \pm 0.7(stat)^{+0.5}_{-1.0}(syst)\ \text{nb}.$$

The differential cross sections $d\sigma_{ep\to D^*X}/dp_\perp(D^*)$ and $d\sigma_{ep\to D^*X}/d\eta(D^*)$ were measured and compared to "massive" and "massless" NLO QCD calculations. The "massive" calculation was found to be in reasonable agreement with the data for $2 < p_\perp(D^*) < 3.25$ GeV only when extreme parameters were used. With the normal parameters the calculation is a factor two below the data. A "massless" calculation is not available for this low $p_\perp(D^*)$ region. For $3.25 < p_\perp(D^*) < 8$ GeV the "massless" calculation describes the data better than the "massive" calculation. Also in this high $p_\perp(D^*)$ region the "massive" calculation with extreme parameters describes the data better than those with the normal parameters. Both calculations show a reasonable agreement with the data in their appropriate region of validity, the "massive" calculation for low $p_\perp(D^*)$ and the "massless" one for high $p_\perp(D^*)$. But both calculations underestimate, for high $p_\perp(D^*)$ and for low $p_\perp(D^*)$, the cross section in forward direction. This in agreement with a previous measurement in a different W range.

The comparison to previous analyses and different NLO pQCD calculations provides a testing ground to investigate the region of applicability for the different NLO pQCD calculations. In general a consistent description of the data was found in the region where the respective calculation is expected to be applicable. In particular the massless calculation gives a good description of the data at high $p_\perp(D^*)$.

Bibliography

[A+74a] J. J. Aubert et al., "Experimental observation of a heavy particle J", *Phys. Rev. Let.* **33** (1974) 1404–1406.

[A+74b] J.-E. Augustin et al., "Discovery of a narrow resonance in e^+e^- annihilation", *Phys. Rev. Let.* **33** (1974) 1406–1408.

[ALE94] ALEPH Collaboration (D. Buskulic et al.), "Production of charmed mesons in Z decays", *Zeitschrift für Physik C* **62** (1994) 1–14.

[AGF93] P. Aurenche, J.-P. Guillet and M. Fontannaz, "Parton distributions in the photon", *Z. Phys. C* **64** (1994) 621–630.

[AGIS83] B. Andersson, G. Gustavson, G. Ingelman and T. Sjöstrand, "Parton fragmentation and string dynamics", *Phys. Rep.* **97** (1983) 31–171.

[ARG92] ARGUS Collaboration (H. Albrecht et al.), "A measurement of the inclusive semileptonic decay fraction of charmed hadrons", *Phys. Lett. B* **278** (1992) 202–208.

[B+91] N. Brook et al., "Photoproduction generators at HERA", in *Monte Carlo Generators*, edited by W. Buchmüller and G. Ingelmann, vol. 3 of *Physics at HERA, Proceedings of the workshop: Hamburg 29-30 October 1991*, 1221, 1991.

[BFHS+01] L. A. T. Bauerdick, A. Fox-Murphy, T. Haas, S. Stonjek and E. Tassi, "Event indexing systems for efficient selection and analysis of HERA data", DESY 01-045, 2001.

[BGMS] V. M. Budnev, I. F. Ginzburg, G. V. Meledin and V. G. Serbo, "The two-photon particle production mechanism. physical problems. applications. equivalent photon approximation", *Phys. Rep.* **15**(4) (1974) 181–282.

[BKK97] J. Binnewies, B. A. Kniehl and G. Kramer, "Coherent description of $D^{*\pm}$ production in e^+e^- and low-Q^2 ep collisions", *Z. Phys. C* **76** (1997) 677–688.

[BKK98] J. Binnewies, B. A. Kniehl and G. Kramer, "Prediction of $D^{*\pm}$ photoproduction at DESY HERA with new fragmentation functions from CERN LEP1", *Phys. Rev.D* **58** (1998) 014014.

[Bri98] G. M. Briskin, *Diffractive Dissociation in ep Deep Inelastic Scattering*, PhD thesis, Tel Aviv University, School of Physics and Astronomy, 1998.

[BS89] A. C. Bawa and W. J. Stirling, "Validity of the equivalent photonapproximationin high-energy electron-proton collisions", *J. Phys. G* **15** (1989) 1339–1348.

[Cac97] M. Cacciari, "On heavy quarks photoproduction and c $\rightarrow$ D* fragmentation functions", DESY 97-156; hep-ph/9708282, 1997.

[CAS94] CERN Application Software Group (S. Giani et al.), "GEANT: Detector description and simulation tool", CERN Program Library Long Writeup W5013, Oct. 1994.

[CDF94] CDF Collaboration (F. Abe et al.), "Evidence for top quark production in anti-p p collisions at $\sqrt{s} = 1.8$ TeV", *Phys. Rev. D* **50** (1994) 2966–3026.

[CDF95] CDF Collaboration (F. Abe et al.), "Observation of top quark production in anti-p p collisions", *Phys. Rev. Lett.* **74** (1995) 2626–2631.

[CFN01] M. Cacciari, S. Frixione and P. Nason, "The p_T spectrum in heavy-flavour photoproduction", JHEP 03(2001)006, 2001.

[CG93] M. Cacciari and M. Greco, "Charm photoproduction via fragmentation", *Z. Phys. C* **69** (1993) 459–465.

[CGN98] M. Cacciari, M. Greco and P. Nason, "The p_T spectrum in heavy-flavour photoproduction", JHEP 05(1998)007, 1998.

[CGRT97a] M. Cacciari, M. Greco, S. Rolli and A. Tanzini, "Charmed meson fragmentation functions", *Phys. Rev. D* **55**(5) (1997) 2736–2740.

[CGRT97b] M. Cacciari, M. Greco, S. Rolli and A. Tanzini, "D* production from e^+e^- to *ep* collisions in NLO QCD", *Phys. Rev. D* **55**(11) (1997) 7134–7143.

[CSS86] J. C. Collins, D. E. Soper and G. Sterman, "Heavy particle production in high-energy hadron collisions", *Nucl. Phys B* **263** (1986) 37–60.

[D0-95] D0 Collaboration (S. Abachi et al.), "Observation of the top quark", *Phys. Rev. Lett.* **74** (1995) 2632–2637.

[DEL93] DELPHI Collaboration (P. Abreu et al.), "A measurement of D meson production in Z^0 hadronic decays", *Zeitschrift für Physik C* **59** (1993) 533–545.

[DJS$^+$79] R. DeWitt, L. M. Jones, J. D. Sullivan, D. E. Willem and H. W. Wyld, "Anomalous components of the photon structure function", *Phys. Rev. D* **19** (1979) 2046.

[DW64] S. D. Drell and J. D. Walecka, "Electrodynamic processes with nuclear targets", *Annals of Physics* **28** (1964) 18–33.

[EK88] R. K. Ellis and Z. Kunszt, "Photoproduction and electroproduction of heavy flavours with gluon bremsstrahlung", *Nucl. Phys B* **303** (1988) 635–664.

[EN89] R. K. Ellis and P. Nason, "QCD radiative corrections to the photoproduction of heavy quarks", *Nucl. Phys. B* **312** (1989) 551–570.

[ESW96] R. K. Ellis, W. J. Stirling and B. R. Webber, *QCD and Collider Physics*, Cambridge University Press, 1996.

[FMNR93] S. Frixione, M. L. Mangano, P. Nason and G. Ridolfi, "Improving the Weizsäcker-Williams approximation", *Physics Letters B* **319** (1993) 339–345.

[FMNR94] S. Frixione, M. L. Mangano, P. Nason and G. Ridolfi, "Heavy-quark correlations in photon-hadron collisions", *Nucl. Phys. B* **412** (1994) 225–295.

[FNR95] S. Frixione, P. Nason and G. Ridolfi, "Differential distributions for heavy flavour production at HERA", *Nucl. Phys. B* **454** (1995) 3–24.

[FP94] S. M. Fisher and P. Palazzi, *ADAMO Reference Manual*, CERN Programming Techniques Group, ECP Division, Februar 1994.

[Fri01] S. Frixione, "Heavy-flavour production at HERA", Talk at DIS 2001; http://ax3ze4.bo.infn.it:9999/~corradi/dis2001/010427/HI/Frixione.pdf, Apr. 2001.

[GIM70] S. L. Glashow, J. Iliopoulos and L. Maiani, "Weak interactions with lepton-hadron symetry", *Phys. Rev. D* **2** (1970) 1285.

[Gla99] L. Gladilin, "Charm hadron production fractions", hep-ex/9912064, 1999.

[GM64] M. Gell-Mann, "A schematic model of baryons and mesons", *Physics Letters* **8** (1964) 214.

[GRV92] M. Glück, E. Reya and A. Vogt, "Parton structure of the photon beyond the leading order", *Phys. Rev. D* **45**(11) (1992) 3986–3994.

[H$^+$77] S. W. Herb et al., "Observation of a dimuon resonance at 9.5 GeV in 400 GeV proton - nucleus collisions", *Phys. Rev. Lett.* **39** (1977) 252–255.

[H1-99] H1 Collaboration (C. Adloff et al.), "Measurement of D* meson cross sections at HERA and determination of the gluon density in the proton using NLO QCD", *Nucl. Phys. B* **545** (1999) 21–44.

[Haa92] T. Haas, "Generating Monte Carlos events with MOZART", ZEUS Note 92-021, 1992.

[Han63] L. N. Hand, "Experimental investigation of pion electropruduction", *Phys. Rev.* **129**(4) (1963) 1834–1846.

[Heb00] K. Hebbel, *Measurement of Charm Production in Deep Inelastic ep Scattering at HERA*, PhD thesis, Universität Hamburg, 2000, DESY-THESIS-2000-016.

[HILM96] G. Hartner, Y. Iga, J. Lane and N. McCubbin, "Offline output information", ZEUS Note 96-013, 1996.

[JB79] F. Jacquet and A. Blondel, in *Proc. Study of an ep Facility in Europe*, edited by U. Amaldi, 391, 1979, DESY 79-48.

[KKS97] B. A. Kniehl, G. Kramer and M. Spira, "Large-$p_\perp$ photoproduction of $D^{*\pm}$ mesons in ep collisions", *Z. Phys. C* **76** (1997) 689–700.

[Kli] K. Klimek, Ph.D. thesis in preparation.

[KW89] R. Klanner and G. Wolf, "Das ZEUS Präzisionskalorimeter für HERA", *Physikalische Blätter* **45**(9) (1989) 365.

[MNR92] M. L. Mangano, P. Nason and G. Ridolfi, "Heavy-quark correlations in hadron collisions at next-to-leading order", *Nucl. Phys. B* **373** (1992) 295–345.

[MNR93] M. L. Mangano, P. Nason and G. Ridolfi, "Fixed-target hadroproduction of heavy quarks", *Nucl. Phys. B* **405** (1993) 507–535.

[MWA+92] G. Marchesini, B. R. Webber, G. Abbiendi, I. G. Knowles, M. H. Seymour and L. Stanco, "Herwig event generator", *Comp. Phys. Commu.* **67** (1992) 465.

[Ng93] J. Ng, "Proposal for a small angle rear track detector for ZEUS", ZEUS Note 93-016, 1993.

[NS99] E. Norrbin and T. Sjöstrad, "Drag effects in charm photoproduction", hep-ph/9905493, 1999.

[Nus75] S. Nussinov , "On possible effects of decays of charmed particle resonances.", *Phys. Rev. Lett.* **35** (1975) 1672.

[NV95] J. Ng and W. Verkerke, "An overview of SRTD analysis", ZEUS Note 95-037, 1995.

[OPA95] OPAL Collaboration (R. Akers et al.), "A measurement of the production of $D^{*\pm}$ mesons on the Z^0 resonance", *Zeitschrift für Physik C* **67** (1995) 27–44.

[PB95] H. Plothow-Besch, "The parton distribution function library", *Int. J. Mod. Phys. A* **10** (1995) 2901–2920.

[PDG00] Particle Data Group (Groom et al.), "Review of prticle physics", *Eur. Phys. J. C* **15** (2000) 1–878.

[PSSZ83] C. Peterson, D. Schlatter, I. Schmitt and P. M. Zerwas, "Scaling violations in inclusive e^+e^- annihilation spectra", *Phys. Rev. D* **27**(1) (1983) 105–111.

[PZ95] K. Piotrzkowski and M. Zachara, "Determination of the ZEUS luminosity in 1994", ZEUS Note 95-138, 1995.

[Sjö94] T. Sjöstard, "Pythia 5.7 and Jestset 7.4", *Comp. Phys. Commu.* **82** (1994) 74.

[Sto98] S. Stonjek, "An object oriented database for ZEUS", in *Conference Proceedings: Computing in High Energy Physics 1998*.

[Web84] B. R. Webber, "A QCD model for jet fragmentation including soft gluon interference", *Nucl. Phys. B* **238**(238) (1984) 492–528.

[Wei34] C. F. Weizsäcker, *Z. Phys.* **88** (1934) 612.

[Wil34] E. J. Williams, *Phys. Rev.* **45** (1934) 729.

[Wit77] E. Witten, "Anomalous cross section for photon-photon scattering in gauge theories", *Nucl. Phys. B* **120** (1977) 189–202.

[WY93] L. Wai and R. Yoshida, "Running MOZART-ZGANA-ZEPHYR chain using FUNNEL", ZEUS Note 93-065, 1993.

[ZEU93] ZEUS Collaboration, "The ZEUS detector, status report", Februar 1993.

[ZEU99] ZEUS Collaboration (J. Breitweg et al.), "Measurement of inclusive $D^{*\pm}$ and associated dijet cross sections in photoproduction at HERA", *Eur. Phys. J. C* **6** (1999) 67–83.

[ZEU99a] ZEUS Collaboration, "Measurement of inclusive $D_s^{\pm}$ and $D^{*\pm}$ cross sections in photoproduction at HERA", Contributed paper to Europhysics Conference on High Energy Physics 1999, 1999.

[ZEU00] ZEUS Collaboration (J. Breitweg et al.), "Measurement of D^* production and the charm contribution to F_2 in deep inelastic scattering at HERA", *Eur. Phys. J. C* **12** (2000) 35–52.

[Zwe64a] G. Zweig, CERN-8192/TH 401 CERN-8419/TH 402, 1964.

[Zwe64b] G. Zweig, "An SU(3) model for strong interaction symmetry and its breaking", CERN-TH-412 74 pp., 1964.

I would like to thank all the people who helped me during the mostly joyful but sometimes hard times while I was working on my Ph.D.

Thank You very much!

In particular I would like to thank R. Klanner for his advice and support and for the opportunity to work with the ZEUS collaboration. I really enjoyed to work in the "D^* in photoproduction" group and I want to thank L. Gladilin, U. Karshon, Y. Eisenberg and D. Hochmann for the great cooperation. It was a great pleasure to work in the "heavy flavor" group. I am really thankful for the endurance T. Carli showed, especially during the last month I worked on my thesis. I want to thank A. Geiser for all the interesting and helpful discussions. N. Pavel also gave countless and valuable advice. I really appreciated to work in the ZEUS offline group and I want to thank T. Haas for the opportunity to work on the ZES project. It was a marvelous time to work together with the students from the Hamburg group. I also want to thank my friends and family for showing me every now and then that there is a life besides physics.